

University of Denver

Digital Commons @ DU

Electronic Theses and Dissertations

Graduate Studies

1-1-2016

Statistical Modeling to Investigate Anatomy and Function of the Knee

Lowell Matthew Smoger
University of Denver

Follow this and additional works at: <https://digitalcommons.du.edu/etd>



Part of the [Biomechanical Engineering Commons](#)

Recommended Citation

Smoger, Lowell Matthew, "Statistical Modeling to Investigate Anatomy and Function of the Knee" (2016). *Electronic Theses and Dissertations*. 1123.
<https://digitalcommons.du.edu/etd/1123>

This Dissertation is brought to you for free and open access by the Graduate Studies at Digital Commons @ DU. It has been accepted for inclusion in Electronic Theses and Dissertations by an authorized administrator of Digital Commons @ DU. For more information, please contact jennifer.cox@du.edu, dig-commons@du.edu.

Statistical Modeling to Investigate Anatomy and Function of the Knee

A Dissertation

Presented to

The Faculty of the Daniel Felix Ritchie School of Engineering and Computer Science

University of Denver

In Partial Fulfillment

of the Requirements for the Degree

Doctor of Philosophy

by

Lowell M. Smoger

June 2016

Advisor: Peter J. Laz

© Copyright by Lowell M. Smoger 2016

All Rights Reserved

Author: Lowell M. Smoger
Title: Statistical Modeling to Investigate Anatomy and Function of the Knee
Advisor: Peter J. Laz
Degree date: June 2016

ABSTRACT

The natural knee is a hinge joint with significant functional requirements during activities of daily living; as a result, acute and chronic injuries can occur. Pathologies are influenced by joint anatomy and may include patellar maltracking, cartilage degeneration (e.g. osteoarthritis), or acute injuries such as meniscal or ligamentous tears. Population variability makes broadly applicable conclusions about etiology of these conditions from small-scale investigations challenging. The work presented in this dissertation is a demonstration of statistical modeling approaches to evaluate population variability in anatomy of the knee and function of its tibiofemoral (TF) and patellofemoral (PF) joints. Three-dimensional (3D) computational models of the bone and cartilage in the knee were characterized using a principal component analysis (PCA) algorithm to understand the primary sources of variability in shape and motion and make predictions from sparse data.

Statistical models were used to investigate relationships between natural knee anatomy and kinematics and make predictions of both shape and function from sparse data. A whole-joint characterization study identified key correlations between shape and function of the TF and PF joints, successfully recreating results from multiple studies and introducing new relationships under one unified approach. Results from this study were

used in a subsequent investigation to build a statistical model of two-dimensional (2D) shape and alignment measures and 6 degree-of-freedom (DOF) kinematics to identify the key measures capable of predicting PF joint motion. The ability to reconstruct the 3D implanted patellar bone of a subject with a total knee replacement (TKR) was evaluated by a statistical shape model of the patella and simulated 2D edge profiles in a custom optimization algorithm. Lastly, a validated predictive algorithm was employed to assess the accuracy of subject-specific knee articular cartilage predictions from bony geometry. The utility of statistical modeling is elucidated by the population-based evaluations of the musculoskeletal system described in this work and could continue to inform characteristics related to pathological conditions and large-scale computational evaluations of implant performance.

ACKNOWLEDGEMENTS

Without hesitation I must recognize my advisor, Dr. Peter Laz, for his guidance, patience, and encouragement. His endeavors to produce both quality research and researchers has earned him the utmost respect from myself and (if I may speak for them) my colleagues. I truly hope that this dissertation will be viewed as an asset to the lab, and that I may now be considered a “giver.” I would also like to thank my committee members, Dr. Paul Rullkoetter and Dr. Mohammad Mahoor, both of whom have contributed valuable recommendations and encouragement. Dr. Rullkoetter’s insistence on what I call “research for a reason” has helped me focus on producing *useful* knowledge. Dr. Mahoor’s insight into the statistical methods presented here have directly influenced the outcomes of the work. Thank you also to Dr. Robert Dores for acting as committee chair; your presence is much appreciated.

Everyone in our lab and department has made DU a wonderful place to spend the past four years. Tremendous thanks to Dr. Matthew Gordon, Renee Carvalho, and Yvonne Pettitt for their organization and handling of everything that allows us to function. From the lab, I would like to specifically thank Azhar Ali and Dr. Adam Cyr. These colleagues consistently helped me when I needed it the most and, thus, deserve much praise. Finally, thank you to all of the people who put up with me on a near daily basis: Justin, Sean, Aruna, Alessandro, Irene, John, Tariq, James, and Vasiliki. You know more about me than you probably ever wanted to! Thanks for letting me share. I’d also like to acknowledge the National Science Foundation, DePuy-Synthes, the DU Department of Mechanical and Materials Engineering, and the Osteoarthritis Initiative for their support of the research projects in this dissertation.

TABLE OF CONTENTS

Abstract	ii
Acknowledgements.....	iv
Chapter 1. Introduction	1
1.1. Introduction	1
1.2. Objectives.....	3
1.3. Dissertation Overview	4
Chapter 2. Background Information and Literature Review	6
2.1. Statistical Modeling of Biological Structures	6
2.2. Anatomical and Functional Analysis of the Knee.....	11
Chapter 3. Overview of Methods.....	16
3.1. Data Collection.....	16
3.1.1. Experimental Testing	16
3.1.2. Imaging and Segmentation.....	17
3.2. Development of the Statistical Model.....	20
3.2.1. The Template Mesh.....	20
3.2.2. Geometry Registration	21
3.2.3. Kinematic Processing.....	23
3.2.4. Principal Component Analysis.....	24
3.2.5. Parallel Analysis.....	26
3.3. Visualization of the Statistical Model	27
3.4. Explicit Finite Element Evaluation of the Statistical Model.....	29
3.5. Automated Measurements on the SSM and its Training Set	31
3.6. Building 3D Models from Radiographs using Statistical Modeling.....	32
Chapter 4. Statistical Modeling to Characterize Relationships between Knee Anatomy and Kinematics.....	48
4.1. Abstract	48
4.2. Introduction	49
4.3. Methods.....	52
4.4. Results	56
4.5. Discussion	60
Chapter 5. Measures-driven Prediction of Patellofemoral Joint Kinematics.....	77
5.1. Abstract	77
5.2. Introduction	78

5.3. Methods	81
5.4. Results	83
5.5. Discussion	85
Chapter 6. Statistical Shape Modeling Predicts Patellar Bone Geometry to Enable Stereo-Radiographic Kinematic Tracking	94
6.1. Abstract	94
6.2. Introduction	95
6.3. Methods	98
6.4. Results	103
6.5. Discussion	105
Chapter 7. Prediction of Knee Articular Cartilage from 3D Bone Geometry Using a Statistical Shape Model.....	115
7.1. Abstract	115
7.2. Introduction	116
7.3. Methods	119
7.4. Results	124
7.5. Discussion	126
Chapter 8. Conclusions and Recommendations.....	137
List of References	140
Appendix A. Related Publications.....	155
Appendix B. Statistical Modeling to Characterize Relationships between Knee Anatomy and Kinematics.....	156
Appendix B.1. List of Anatomical Measures	156
Appendix B.2. Description of Further Modes	157
Appendix C. Patella Digitization Instructions in XMA Lab.....	167
Appendix D. Training Set Identifiers.....	176

LIST OF TABLES

Table 3.1 Scan data and research study usage.	36
Table 4.1 Descriptive statistics and anatomical measures for the training set.....	73
Table 4.2 Pearson’s correlation coefficients between the first six principal components and anatomical and kinematic measures. Initial alignment correlations were calculated at approximately 10 degrees TF flexion. Range-of-motion (ROM) was defined as the difference between the minimum and maximum values in a kinematic measure. Correlations are presented as absolute values. Anatomical measures with no significant correlations were omitted. White cells indicate no correlation.....	74
Table 4.3 Pearson’s correlation coefficients between anatomical and kinematic measures. Initial alignment correlations were calculated at 10 degrees TF flexion. Range-of-motion (ROM) was defined as the difference between the minimum and maximum values in a kinematic measure. Correlations are presented as absolute values. Anatomical measures with no significant correlations were omitted. White cells indicate no correlation.....	75
Table 4.4 Mean absolute error between experimental and predicted lowest point results averaged across all specimens. All values are in millimeters.	76
Table 5.1 Descriptive statistics for the linear measures of the PF joint.....	92
Table 5.2 Cumulative variability explained with the specified number of modes of variation.	92
Table 5.3 Mean RMS error and standard deviations (SD) for individual sets of predictive measures for each kinematic DOF. Difference is between FE-predicted and measure-predicted kinematics.	93
Table B.1 Cumulative variability explained with the specified number of modes of variation.	159
Table B.2 Pearson’s correlation coefficients between net kinematics defined here as the difference between start and end positions in the flexion cycle. Correlations are presented as absolute values. White cells indicate no correlation.	160
Table D.3 Training set identifiers and demographics from the University of Kansas, DePuy-Synthes, and Osteoarthritis Initiative databases.	176

LIST OF FIGURES

Figure 3.1 The process of extracting joint kinematics for the statistical shape and function model: Rigid body markers (white) fixed to the femur, tibia, and patella are tracked during *in vitro* cadaveric knee testing (A). Alignment of specimen-specific geometry (gray) and local anatomical coordinate systems (red) to probed cadaver surface points (yellow) defines position of the bones with respect to the rigid bodies. Grood-Suntay open-chain kinematics are calculated from the relative motion of the local bone coordinate systems (C)..... 37

Figure 3.2 The process of building a training set for the statistical shape model: Segmentation of a MR scan (A), the resulting 3D stereolithography model (B), alignment to bone template mesh (C) and handle placement on articular cartilage (D), “as-scanned” alignment of template mesh-registered specimen-specific geometry (E), Completed training set of 40 specimens (F)..... 38

Figure 3.3 A comparison of the cumulative distribution functions (CDF) for the femur epicondylar width measurement across multiple populations shows a similar range of geometric size in the current training set. 39

Figure 3.4 Cartilage registration graphical user interface (GUI) with representative femur cartilage from segmentation. Black points represent the manually selected landmark sites to guide the placement of surface handles on the stereolithography (STL) mesh. 39

Figure 3.5 Template hexahedral cartilage mesh with surface handles (yellow) (Baldwin et al., 2010). 40

Figure 3.6 Alignment of registered specimen-specific geometry to their digitized position (yellow points) in the Kansas Knee Simulator (KKS)..... 40

Figure 3.7 Eigenvalues for each principal component (PC) are ranked by magnitude (variance). The number of significant PCs in a model (blue) are those with variances greater than the variances in 5-95% bounds of models built from randomized instances of the same dataset (green and red). 41

Figure 3.8 The automated ligament morphing algorithm wrapped soft tissue structures (gray) around the first three principal component shapes of bone for a representative SSM. Structures shown include the rectus femoris (RF), vasti, patellar ligament (PAT-LIG), medial collateral ligament (MCL), superficial MCL (sMCL), lateral collateral ligament (LCL), medial and lateral patellofemoral (MPFL and LPFL), and posterior capsules (PCAP). 42

Figure 3.9 FE model of the mean geometry used in the computational analysis. The position shown is in initial alignment of approximately 15 degrees. 43

Figure 3.10 Kinematics and contact mechanics for the mean geometry. Maximum contact pressure, mean contact pressure, and contact area (top) for the TF and PF joints. Imposed KKS (black) and measured Abaqus (blue) tibial kinematics (middle) and patellar kinematics (bottom). 44

Figure 3.11 Contour maps of the contact pressures from the FE analysis for the tibia and patellar cartilages. The full geometry on the left shows the relative position of the joint for each of the three flexion angles..... 45

Figure 3.12 Illustrations of some of the automated linear measures: epicondylar width (a), anterior sulcus angle (b), sulcus width (c), cartilage width along epicondylar axis (d), antero-inferior sulcus angle (e), condylar ML and AP widths (f), intercondylar notch width at the distal aspect (g), distal sulcus angle (h), bisect offset (i), Insall-Salvatti index (j), tibial cartilage ML and AP widths (k), trochlear groove radius of curvature (l), patellar angle (m), patellar ML width (n), and patellar ridge medialization (o). 46

Figure 3.13 Orientation of a right knee in the HSSR for imaging. Light sources at the X-ray generators create a shadow of the object on the image-intensifiers to aid in alignment of the knee. 47

Figure 3.14 Digitization of the resection plane from stereo radiographic images (left) for the implanted patellar bone. Epipolar lines 1_A-3_A are projected across image plane B to inform the selection of associated points, 1_B-3_B , on the resection plane projection. The resulting 3D position of the points (red, green, blue) represents the resection plane in the patellar local coordinate system (right)..... 47

Figure 4.1 Development of a statistical shape and function model. The shape representation was derived from image data by segmenting and establishing correspondence to a template mesh, and tibiofemoral and patellofemoral kinematics were obtained from cadaveric testing and registration of the anatomy and local coordinate systems (CS) to experimentally probed points. 66

Figure 4.2 Training set of 20 specimens used to create the statistical shape-kinematics model. Specimens are represented with the template mesh in the initial kinematic position..... 67

Figure 4.3 Representations of bone and cartilage for the first three principal component modes. Knees are shown at +/- 1.5 standard deviations. Coronal and sagittal views at initial alignment with merchant view at 45° TF flexion. 68

Figure 4.4 Tibiofemoral kinematics for the first 3 principal component modes and all specimens (gray lines). Clockwise from top: Tibial flexion-extension, anterior-posterior (AP) translation and internal-external (IE) rotation. Inset bar charts show relative contribution of each mode. 69

Figure 4.5 Patellofemoral kinematics for the first 3 principal component modes and all specimens (gray lines). Clockwise from top-left: Patellar internal-external (IE) rotation, medial-lateral (ML) translation, superior-inferior (SI) translation and anterior-poster (AP) translation. Inset bar charts show relative contribution of each mode. ISI = Insall-Salvati Index. 70

Figure 4.6 Sagittal condylar geometry (with radius of curvature lines) for the mean and first three modes (left). Femoral lowest point representation of the TF contact points for the first three modes at +/- 1.5 standard deviations (right). 71

Figure 4.7 Comparison of actual (solid) and predicted (dashed) lowest contact point for a leave-one-out evaluation with varying flexion. Predictions were made with each member of the training set left out of the analysis. Error bars shown for anterior-posterior (AP) and medial-lateral (ML) degrees of freedom on each condyle. Full extension results reported as 0-10° flexion as not all specimens achieved 0° 72

Figure 5.1 Illustrations of the automatically extracted linear measures. Measures include femur epicondylar width (a), femur anterior sulcus angle (b), femur antero-inferior sulcus angle (c), patellar cartilage width and height (d), femur cartilage width along the epicondylar axis (e), medial trochlear inclination (f), lateral trochlear inclination (g), distal sulcus angle (h), patellar angle (i), Insall-Salvati Index (j), intercondylar notch width (k), femur sulcus width along the posterior condylar line (PCL) (l), bisect offset (m), and femur AP width (n). The angle formed by the PCL and the line connecting both anterior condylar points on the femur (image n) describes the trochlear angle (axial plane)..... 89

Figure 5.2 Patellofemoral kinematics for the first three principal component modes and all subjects (gray lines). Patellar varus-valgus (VV) and internal-external (IE) rotation (top), medial-lateral (ML) and superior-inferior (SI) translation (bottom)..... 90

Figure 5.3 Comparison of measure-based (current study) and shape-based kinematics (Fitzpatrick et al. 2011) to training set kinematics (Fitzpatrick et al. 2011) for two representative subjects (bold curves). Training set kinematics (from FE) are shown in gray and illustrate the spread for each degree of freedom. 91

Figure 6.1 Imaged position of the flexed left knee in the high speed stereo radiography (HSSR) system, top view (left). Representation of the imaged knee as seen on camera planes A and B (right). Note: Subject is supine..... 109

Figure 6.2 A representative intact patella (left) and, after automated implantation, its resected version (right). 110

Figure 6.3 Proposed imaging positions with varying orientation in the horizontal plane of the stereo-radiography system. 110

Figure 6.4 Schematic of the optimization algorithm to reconstruct the full 3D patellar geometry from simulated sparse data. PC scores of the patellar bone SSM are optimized until the profile (black) of the projected point cloud (green) matches the simulated target profiles (red). The magenta lines represent corresponding points on the target and predicted profiles. RMS error calculated between these corresponding point sets is minimized by the optimization algorithm. 111

Figure 6.5 Representations of patellar bone for the first three principal component modes. Patellae are shown at +/- 1.5 standard deviations. Views include coronal (top), sagittal (middle), and transverse (bottom). 112

Figure 6.6 Nodes of an instance of the patellar bone SSM (green) projected by the DLT onto the camera image planes and its profile (black). The anterior region of the target profiles for a representative left-out subject (red). One position is shown for rigid body alignment of the mean instance and then all five positions over ~180° for the optimized instance. 112

Figure 6.7 Comparison of the three imaging scenarios for a representative subject; the 1st position (left), the 1st, 3rd, and 5th positions (center), and all five positions (right). Bar charts show the 2D image plane error (blue) in pixels and anterior surface 3D geometric error (red) in millimeters for each scenario. Contours represent absolute difference between the actual and predicted shape for the resected case. Contour units are in millimeters. 113

Figure 6.8 Contours of absolute difference between the actual and predicted shape for the resected case using all 5 positions. Four representative subjects are shown. Individual RMS errors are reported next to each subject. Units are in millimeters. 114

Figure 7.1 Development of a statistical shape model of the knee: Scans of an MRI were segmented to generate a 3D stereolithography (STL) model of the bone and cartilage. Bone was registered to a template using an Iterative Closest Point (ICP) algorithm while cartilage, being a thinner structure, required a custom developed algorithm and GUI to register the STL geometry. A template developed for a median-sized subject was then morphed for each training set member to establish correspondence between like structures. 132

Figure 7.2 The segmented geometry is loaded into the Matlab® graphical user interface (top left), landmark points (red) are manually selected to guide the automatic distribution of handles (black) onto the subject's surface (bottom left). This dually establishes correspondence to the training set and the template hexahedral mesh (bottom right). A mesh-morphing algorithm deforms the template hexahedral mesh to the subject's segmented shape to generate an FE-ready cartilage representation (top right). 133

Figure 7.3 Representations of the bones and cartilage for first three principal component modes from the combined bone-cartilage model. Knees are shown at +/- 1.5 standard

deviations and bones are aligned to their local coordinate systems. Alignments are for relative comparison between mode perturbations.....	134
Figure 7.4 Correlations within the combined bone-cartilage SSM. Overall PC scores were correlated to bone-only PC scores (left) and cartilage-only PC scores (right). PCs with high correlations in both figures indicate that the shape described by those modes have strong predictive potential.....	135
Figure 7.5 Comparison of actual and predicted cartilage distribution and thickness for the femur and patella. The patella has been enlarged for the visualization purposes. Thickness is represented by the color contour on the actual and predicted cartilage surface. Units are in millimeters.	136
Figure B.1 Absolute and relative tibiofemoral kinematics for the first 3 principal component modes and all specimens (gray lines). Bar charts show relative contribution of each mode.	161
Figure B.2 Absolute and relative patellofemoral kinematics for the first 3 principal component modes and all specimens (gray lines). Bar charts show relative contribution of each mode.	162
Figure B.3 Scatter plots of mode, shape and kinematic relationships with strong correlations. PC score for Mode 1 versus epicondylar width (A), anatomic measures versus tibiofemoral (TF) kinematics (B-C), and patellofemoral (PF) shape and kinematics (D-F). Colored data points represent the first six PC modes at $\pm 1.5\sigma$. Pearson's correlation coefficient (r) and linear equation are reported for each plot.	163
Figure B.4 Distal view of Mode 4+ and 4- showing variation in patellar ML alignment and lateral trochlear inclination (top left). The absolute patellar ML translation curve further illustrates the high ROM in Mode 4- (top right). Geometric differences in the medial femoral condyle contribute to the variation in relative tibial SI translation (bottom left and right).....	164
Figure B.5 Proximal view of Mode 5+ and 5- showing variation in intercondylar notch width (top left). Relative tibial ML translation through the cycle (top right). Variation in the distal region of the medial femoral facet influences the relative patellar ML translation through the cycle (bottom left and right). Dimensions are shown in millimeters unless otherwise noted.	165
Figure B.6 Initial anterior tibial alignment in Mode 6- is associated with more prominent postero-inferior femoral condyles (top left). Second to Mode 1, Mode 6 exhibited a large amount of through-cycle variation in tibial AP translation (top right). Variation in distal sulcus angle (bottom left) and relative tibial IE rotation (bottom right) are highly correlated ($r = 0.83$).	166

CHAPTER 1. INTRODUCTION

1.1. Introduction

Kinematics and contact mechanics are known factors contributing to natural knee joint pathologies, including patellar subluxation and dislocation (Boling et al., 2010), and osteoarthritis (OA), or degeneration of the articular cartilage (Andriacchi and Mündermann, 2003 and 2006; Neogi et al., 2013). The onset of OA, in particular, can exacerbate these conditions through increased pain and altered mechanics (Hamai et al., 2009; Brage et al., 1994). The knee is a complex anatomical structure comprised of the tibiofemoral (TF) and patellofemoral (PF) joints. Understanding the relationships between shape and 6 degree-of-freedom (DOF) joint motion is therefore useful for improving outcomes from physical therapy and total knee replacement (TKR). Experimental investigations into knee joint function have historically involved *in vitro* or *in vivo* data collections on cadaveric specimens or live subjects and joint anatomy has traditionally been characterized by 2D linear measures on magnetic resonance (MR) or computed tomography (CT) scans. These methods, however, are limited in their ability to describe complete knee morphology or measure muscle forces and internal joint loads.

Computational biomechanics offers an efficient means by which to investigate complexities of the human musculoskeletal system that would otherwise be too difficult or cost prohibitive to study experimentally. Studies have developed complex

computational models on a small number of subjects to assess subject-specific characteristics of the joint (Halloran et al., 2005; Baldwin et al., 2012). These studies provide valuable insight into the mechanics of the knee joint, but are limited in their applicability to the broader population. Joint anatomy and kinematics of the knee vary significantly across the entire human population and within ethnicities (Leszko et al., 2012; Mahfouz et al., 2013). Population-based analyses are becoming increasingly relevant as the age range for injuries and surgical intervention increases (Ravi et al., 2012).

Statistical methods provide a means by which to evaluate variability and uncertainty in biological systems. When linked to computer models of the human musculoskeletal system, these methods can account for anatomical and physiological variation in a population of subjects. Statistical shape models (SSMs) have evaluated three-dimensional (3D) geometric variability in bone, cartilage and ligamentous structures across a training set of subjects (Meller et al., 2004; Chintalapani et al., 2007). Other applications have included assessment of resection plane positioning to inform TKR component sizing (Dai et al., 2013), and prediction of 3D bone shape from sparse data such as digitized anatomical landmarks during surgical intervention or 3D ultrasound imaging (Fleute et al., 1998; Barratt et al., 2008).

In addition to structural anatomy, statistical models have incorporated material property and functional characteristics of bones and joints (Deluzio et al., 2007; Bryan et al., 2010; Sarkalkan et al., 2014). SSMs involving multiple structures have informed not only relationships between adjoining bones but also joint alignment and kinematic

variability (Rao et al., 2013). This dissertation describes the use of statistical methods to further investigate variability in shape, alignment and function of the natural knee and their application to identify key clinical measures related to function, improve the efficiency of experimental methods, and predict previously unexplored characteristics from sparse data.

1.2. Objectives

The objectives of this dissertation were to develop several statistical models of the knee joint for applications ranging from characterization of population variability to prediction of shape or function. Models varied in size of the training set and were developed with different combinations of shape, alignment and function variables. Bone, cartilage and ligament structures of the tibiofemoral (TF) and patellofemoral (PF) joints were extracted from CT, MR, or stereo radiographic images and registered to a common point distribution model (PDM). TF and PF kinematic data were obtained from experimental testing or numerical simulations; for correspondence, the data were also registered in a consistent manner.

Each statistical model was developed by applying principal component analysis (PCA) to the registered training set of subject data. PCA reduced the large number of shape and/or function variables into a smaller set principal component (PC) scores describing important structure within the data. The models were employed in leave-one-out analyses to make predictions either between registered training set data or from unregistered, sparse data such as 2D images that were not part of the training sets. Specific aims included (1) characterizing shape-function relationships in the TF and PF

joints, (2) predicting PF joint function from linear geometric measures, (3) reconstruction of 3D patellar bone from x-ray images, and (4) predicting cartilage from bony geometry with an SSM of the whole knee.

1.3. Dissertation Overview

Chapter 2 provides an overview of the published literature on measures-based and statistical modeling approaches to computational analyses of the knee. The chapter primarily focuses on relationships between shape and function, estimation of shape from sparse data, and predictions of shape or function for new, unknown subjects.

Chapter 3 provides an overview of the methods to develop, evaluate and use statistical shape models. Specifically, this chapter describes data collection and processing, statistical model development using PCA, training set and PC mode visualization, statistical model-based finite element analysis, automated clinical shape parameter measurements, and 3D object reconstruction from 2D radiographs.

Chapter 4 presents *Statistical Modeling to Characterize Relationships between Knee Anatomy and Kinematics* whose objective was to describe relationships between knee anatomy and tibiofemoral and patellofemoral kinematics using a statistical shape and function modeling approach. Similar models and techniques presented here are also used in subsequent chapters. This study has been published in the Journal of Orthopaedic Research.

Chapter 5 presents *Statistical Shape Modeling Predicts Patellar Bone Geometry to Enable Stereo-Radiographic Kinematic Tracking* whose objective was to accurately predict the shape and pose of the natural patella from biplane fluoroscopic images using a

patella-specific statistical shape model. This study has been accepted for presentation at the 2016 annual meeting of the Orthopaedic Research Society and will be submitted in manuscript form to a peer-reviewed journal.

Chapter 6 presents *Prediction of Knee Articular Cartilage from 3D Bone Geometry Using a Statistical Shape Model* whose objective was to accurately predict specimen-specific distribution and thickness of the femoral, tibial and patellar articulating cartilages from the specimen bony geometry using a statistical shape model of the knee joint. This study will be submitted in manuscript form to a peer-reviewed journal.

Chapter 7 presents *Measures-driven Prediction of Patellofemoral Joint Kinematics* whose objective was to predict patellofemoral function from linear shape measures on the previously developed statistical shape and function model described in Chapter 4. This study will be submitted in manuscript form to a peer-reviewed journal.

Chapter 8 discusses the specific contributions of this dissertation in addition to suggestions for continuing work with statistical modeling techniques in the field.

CHAPTER 2. BACKGROUND INFORMATION AND LITERATURE REVIEW

2.1. Statistical Modeling of Biological Structures

Population variability introduces a challenge for researchers in their pursuit to understand the complex function of biological structures. Size and shape are fundamental differences among structures of interest, and statistical (or active) shape models (SSMs) have been developed to characterize and quantify these variables in members of a population. Cootes et al. originally illustrated the utility of SSMs by describing two-dimensional (2D) geometric differences in circuit-board resistors with principal component (PC) modes of variation. The modes described important structural variability such as body length, body width, and wire length in the training set of resistors that were used to build the model (Cootes et al., 1995). Correspondence between training set members was achieved by manual selection of landmark features on the resistor shapes such as points at the ends of the wires or along the outline of the resistor body. A unique characteristic of the SSM was elucidated by plotting the first two modes of variation against each other; the lack of correlation illustrated their independence and thus, efficient representation of population variability.

Statistical modeling techniques have been extended to 3D models of human bones to better understand population anatomical variability. Lorenz et al. introduced the idea

of a surface point distribution model (PDM) that acts as a template upon which to register like shapes for point-to-point correspondence (Lorenz et al., 2000). Important geometric differences have been elucidated by correlations between common anatomical features on the bone and principal component modes of variation (Meller et al., 2004). Other early applications have included fitting SSMs to x-rays for subsequent age or density measurements (Behiels et al., 2002) and semi-automated CT or MR scan segmentation (Fripp et al., 2006) to efficiently develop 3D subject-specific models.

The inclusion of multiple structures into a single SSM has informed whole joint morphology and alignment characteristics in the shoulder (Yang et al., 2008) and knee (Baldwin et al., 2010). Baldwin et al. built a PCA-based SSM of articular cartilage in the tibiofemoral (TF) and patellofemoral (PF) joints from automatically segmented MR scans. Shape and alignment of the cartilage were described by the first few PC modes of variation; isotropic scaling and significant as-scanned alignment was represented in Mode 1, patellar SI alignment as described by Mode 2, and sagittal plane shape changes were described by both Modes 3 and 4. Although limited in its ability to describe performance-related alignment characteristics, the model successfully illustrated the ability to dually described shape and relative position of anatomical structures. Yang et al. evaluated shoulder joint anatomy in primates by applying PCA to a training set of scapulae and humeri as a data reduction technique and then utilized canonical correlation analysis (CCA) to quantify geometric relationships for a subsequent predictive analysis (Yang et al., 2008). CCA was applied to the PC modes of each bone and described “highly linear morphological interrelationships” between bones of the shoulder joint.

Recent SSMs have also expanded to incorporate other metrics such as bone density distribution to further inform population variability in material properties (Querol et al., 2006; Bredbenner, et al., 2008; Bryan et al., 2010; Sarkalkan et al., 2014). CT scans, which also contain gray-scale density information, were used to dually fit shape models for extraction of both geometry and material properties in a cohort of femurs (Querol et al., 2006; Brednenner et al., 2008; Sarkalkan et al., 2014). Bryan et al. extended an SSM of the whole femur to incorporate material properties with the goal of creating models suitable for finite element (FE) analyses (Bryan et al., 2010). The authors demonstrated the robustness of the model by leave-one-out and reconstruction tests that assess predictive and descriptive capabilities of the model. Utility of material-mapped shape models was further demonstrated by the efficient development of virtual models for subsequent FE investigations; 1000 FE material-mapped femurs were subjected to a fall-loading condition to study femoral neck fracture risk (Bryan et al., 2009). Results relating fracture location and the surrounding bone mineral density distribution illustrated the technique's ability to recreate common fracture patterns and provide valuable correlations to local bone material properties. Sarkalkan et al. illustrated the diagnostic capabilities of incorporating material properties by identifying modes of variation with predisposing factors for osteoarthritis (OA) such as including bone porosity in the femoral head (Sarkalkan et al., 2014).

Multi-body statistical models have been further developed with the addition of performance measures such as kinetics, kinematics and deformation mechanics. Statistical models of kinematics and kinetics have been employed to evaluate patterns and

inform functional consequences of subjects with OA (Deluzio et al., 1997). Galloway et al. similarly built a statistical model of TF kinetics from musculoskeletal models of gait representing 31 pre-operative TKR patients (Galloway et al., 2012). Leave-one-out and reconstruction tests demonstrated the model's ability to predict and fully describe the kinetic curves, thus meeting the authors' goal for developing a population of virtual instances from a small training set.

With the goal of predicting kinematics and contact mechanics from shape, Fitzpatrick et al. combined anatomy and mechanics to develop an SSM of PF joint cartilage in a prescribed loaded alignment and finite-element (FE) predicted mechanics (Fitzpatrick et al., 2011). The first several modes of variation described similar size and shape changes as Baldwin et al.; uniform scaling, patella alta and sulcus groove depth were descriptors of Modes 1, 2 and 3, respectively (Baldwin et al., 2010). Kinematics and contact mechanics were predicted in a leave-one-out analysis using only the shape of the left-out specimen and the SSM. Good agreement existed between the FE- and SSM-predicted kinematics with root mean square errors of less than 3 degrees and 2.5 mm. The holistic approach of evaluating shape variability through statistical analysis of point distribution models (PDMs) introduces the ability to study groups of points, specifically edges, which can be used to predict and track 3D representations.

The predictive capability of SSMs has also been used to reconstruct 3D bone contours from fluoroscopic x-rays (Kurazeme et al., 2009; Zhu et al., 2011; Baka et al., 2011) for *in vivo* bone tracking to measure 6 degree-of-freedom (DOF) joint kinematics. Baka et al. developed a technique for optimizing shape parameters in a 3D SSM of the

distal femur to achieve accurate pose and shape estimation based on Canny edge maps of 2 or more coupled fluoroscopic images. Accuracy to within 1.68 mm of the ground-truth geometry was achieved, illustrating the feasibility of this technique to accurately reproduce specimen-specific 3D bone contours and eliminate the need for acquisition and segmentation of MR or CT images, thus reducing processing time and radiation exposure to patients. Baka et al. extended their previous work of shape and pose estimation to a sequence of fluoroscopic images for femur bone tracking and relative motion through the sequence (Baka et al., 2012). The two-step alternating process included one initial manual alignment of the mean model geometry with automatic pose fitting to subsequent frames in the sequence by seed information from the previous frame. The second step optimized the shape parameters across all frames to obtain a single shape estimate for the entire sequence. Root-mean-square (RMS) error for SSM-based shape predictions was 1.48 mm and RMS tracking errors in ML and AP translations and rotations were less than 0.2 mm and 0.1 degrees. Internal-external (IE) rotation was the most difficult DOF to predict with RMS error of 1 +/- 2.5 degrees. The limitation was attributed to axisymmetry in the femoral shaft during IE rotation and relatively low impact of the distal region where useful edge variation occurs during IE. In their latest study, Baka et al. used the previously described technique to estimate shape and pose of both the tibia and femur to calculate *in vivo* TF kinematics of a jump-landing activity in biplane fluoroscopic images (Baka et al., 2014). Kinematic accuracy between the SSM-based and CT-segmented models was within 1 mm and 1 degree with the exception of axial tibial rotation (1.18 degrees). The authors also demonstrated that more accurate SSM-

based geometries do not necessarily result in more accurate measurements, suggesting that 2D-3D fitting plays a larger role in determining *in vivo* kinematics. To date, no authors have attempted to reconstruct patellae or PF kinematics, which may further reduce the need for segmentation and processing of 3D models from CT or MR scans.

SSM-based predictions have also been used to predict adjoining bones (Yang et al., 2008). A statistical model of the scapula and humerus was developed and subsequently used in a leave-one-out type of analysis to predict one bone shape from the shape of the other. A non-linear partial least squares (NIPALS) algorithm took advantage of the common relationships, or redundancies, (e.g. corresponding isotropic scaling) between the two bones within each principal component and described by their implementation of CCA. Redundancies are revealed in the off-diagonal components of the covariance matrix while diagonal components represent variances and highlight important structure in the dataset. Traditionally, low covariance is sought when determining the optimal bases to describe the dataset (Shlens et al., 2014); however, non-zero covariance components may indicate strong relationships between variables that a statistical model could use to estimate missing information in incomplete datasets.

2.2. Anatomical and Functional Analysis of the Knee

Owing to the complex morphology and functional requirements of the knee, researchers have been compelled to investigate specific characteristics of shape and kinematics. There is value in understanding the influence of a particular anatomical feature on joint motion for diagnosis and treatment of pathologies. Historically, joint anatomy has been characterized and measured from medical imaging (e.g. CT, MR, or x-

ray) or cadaveric studies. Studies have focused on sagittal plane knee morphology in an effort to understand the main anatomical drivers of flexion, and in-plane (SI and AP) translations of the TF and PF joints (Iwaki et al., 2000; Martelli et al., 2002; Masouros et al., 2010). Iwaki et al. looked at sagittal MR scans of the TF joint and characterized the femur articular condyles as arcs of varying length and radius (Iwaki et al., 2000). The medial condyle was described as two separate arcs: an anterior arc associated with extension and a posterior arc associated with flexion. The medial plateau of the tibia was described as two flat regions with the anterior region (extension facet) angled posteriorly and articulating with the femur's extension arc in early flexion. Posterior to the extension facet, the flexion facet articulates with the posterior arc of the femur; however, the authors described the relative motion of the medial compartment as almost entirely rotational, with little AP translation. The lateral condyle was described primarily by a flexion facet upon which joint rotation and translation occurred. This variation in AP translation between the medial and lateral condyles during flexion causes internal tibial rotation, commonly referred to as the screw-home mechanism (Masouros et al., 2010; Piazza and Cavanaugh, 2000).

In addition to the sagittal plane, Martelli et al. evaluated MR scans of the articular surfaces in all three major anatomical planes to further understand geometric and kinematic variability (Martelli et al., 2002). A coronal view of the joint revealed curved and thus, more congruent TF surfaces between the inside aspect of the medial condyle and the tibial eminence. However, a flattened interior aspect of the lateral condyle resulted in less congruency, suggesting a relationship with increased mobility. In a

transverse (axial) view, the medial side of the tibial eminence was relatively linear in the AP direction, but laterally it exhibited a more convex curve. The authors indicated that this increased congruency in the medial compartment contributed to the constraint of the medial condyle and subsequent arcing motion of the lateral condyle around the tibial eminence and about a medially-orientated longitudinal axis. Furthermore, the congruency and constraint of the medial compartment also likely contributes to coronal plane varus rotation, which is often accompanied by lift-off of the lateral condyle during flexion (Martelli et al., 2002).

PF joint geometry is characterized by two articulating facets on the posterior aspect of the patella and the femur trochlear groove. As the patella slides along the groove, its primary function is to increase the moment arm of the quadriceps muscle and improve TF flexion efficiency (Masouros, et al., 2010). The shape and conformity of these surfaces are known to affect joint alignment, motion and pain (Harbaugh et al., 2010; Powers et al., 2000; Pal et al., 2013; Stefanik et al., 2013). Stefanik et al. measured features of the PF joint in 907 axial plane MR scans and correlated patellar tilt angle with lateral trochlear inclination and trochlear angle. Bisect offset of the patella was also correlated to lateral trochlear inclination ($r = -0.38$). Harbaugh et al. correlated lateral trochlear inclination with medial patellar alignment in both a healthy control group and a patellar maltracking group (Harbaugh et al., 2010). Medial tilt or IE alignment of the patella was also correlated to both cohorts ($r = 0.61$ and $r = 0.57$, respectively).

Pal et al. measured patella alta-baja, patellar tilt angle and bisect offset from oblique-axial planes of 3D MRIs in PF pain-free subjects and subjects experiencing PF

pain (Pal et al., 2013). PF pain subjects experienced more patellar maltracking with an alta patella and, within the PF pain group, there were significant differences in patellar tilt for subjects with alta patella versus those with pain and normal patellar height. The authors also suggested that bisect offset may be another parameter that varies in PF pain versus pain-free subjects ($p = 0.058$). Powers et al. assessed trochlear groove depth in the axial plane of MR scans and found correlations with patellar medial-lateral tilt and displacement in early flexion (Powers et al., 2000). A shallower groove described by a larger sulcus angle was correlated to both laterally rotated and laterally displaced patellae. Varadarajan et al. found that axial MR plane parameters such as mediolateral trochlear sulcus position and trochlear bisector angle were more strongly correlated to axial alignment and kinematic parameters, e.g. tilt and ML position, than coronal measures, e.g. trochlear groove angle and patellar VV alignment (Varadarajan et al., 2010). Freedman and Sheehan assessed the ability of 2D MR image-based measurements to predict 3D kinematics using a regression-based approach (Freedman and Sheehan, 2013). Measurements of static patellar tilt angle and bisect offset were strongly correlated to their dynamic counterparts but were not enough to predict complete 3D dynamic kinematics.

In addition to the articular surfaces, investigations of inter-joint and whole bone characteristics have reported correlations to knee mechanics. Hill et al. noted that during loaded squatting, an initial tibial position in external rotation demonstrated less internal rotation than an initial tibial position in neutral (Hill et al., 2000). Similarly, Pal et al. reported that alta patellae did not demonstrate as much flexion or medial-lateral

translation through the flexion cycle as the healthy control group (Pal et al. 2013). The most significant inter-joint relationship at the knee was reported by Sheehan et al. who noted that internal tibial rotation resulted in increased medial patellar tracking (Sheehan et al., 2009). In an investigation of knee kinematics and the whole femur bone, Hoshino et al. reported that two measurements, condylar twist angle and condylar offset ratio, were positively correlated to tibial internal rotation and anterior translation, respectively (Hoshino et al., 2012). This finding suggests that it is not simply the articulating geometry of the distal condyles that influences knee joint motion but also their relative alignment to the proximal femoral head.

CHAPTER 3. OVERVIEW OF METHODS

This chapter describes the methods that were used to develop, analyze, and apply statistical models of knee for the studies presented in subsequent chapters. Data collection involved experimental testing and computational analysis of joint kinematics, creation of specimen-specific 3D models from magnetic resonance (MR) images, and automated extraction of linear measures. The PCA-based approach for SSM development is discussed with a focus on its application for a comprehensive training set of specimen geometry (bone, cartilage, and ligaments) and 6 degree-of-freedom (DOF) kinematics for the TF and PF joints. Processing and visualization of the geometric and kinematic representations for principal component modes of variation illustrates the utility of statistical models in FE modeling. Finally, the methods for predicting 3D shape from 2D images with a statistical model is discussed in relation to a subsequent study.

3.1. Data Collection

3.1.1. Experimental Testing

Chapter 4 presents experimental knee mechanics that were used to develop a statistical shape and function model of the TF and PF joints. This section discusses the experimental protocol and subsequent processing that was performed to acquire those data. *In vitro* testing of cadaveric knee joints provides access to detailed information

about the joint and its function that is difficult to acquire from *in vivo* methods. The Kansas Knee Simulator (KKS) is an experimental simulator in which cadaveric knees are mounted and controlled by a simulated hip, ankle and quadriceps load to replicate a variety of activities including gait and squatting (Figure 3.1). Rigid body markers are surgically mounted to the femur, tibia and patella and subsequently tracked via an Optotrak system (Northern Digital, Waterloo, ON). These tracked points can then be used to calculate the relative motion between the three bones and thus, the 6-DOF kinematics for the PF and TF joints (Halloran et al., 2005; Maletsky and Hillberry 2005).

3.1.2. Imaging and Segmentation

3D representations of the knee used in subsequent chapters and statistical models were acquired from traditional imaging and segmentation approaches. Imaging modalities and the structures that they reveal are discussed in this section. Detailed information regarding the internal and surrounding structures of the knee joint are accessible through the use of magnetic resonance (MR), computed tomography (CT), and radiographic x-ray imaging modalities. Radiographs are the most common modality; however, they rely on x-rays and thus are limited in their ability to capture the structural detail of a joint since x-rays are only absorbed by dense structures and calcium-rich bone. While radiographs are used to assess bone quality and static joint alignment, a real benefit is the speed at which they can be captured (e.g. in fluoroscopic systems), which makes them an ideal choice for visualizing *in vivo* dynamic activity of joints and other internal systems via radiopaque agents. CT imaging utilizes radiographic x-rays acquired at different axial positions around an object, which are then tomographically

reconstructed into nearly adjacent cross-sectional images of the object. The result is a set of sequential 2D planar images that contain detailed shape and density information for the imaged bone. However, this method also relies on x-rays and thus it lacks the ability to capture soft tissue structures such as cartilage, ligaments, tendons and musculature. MR images provide detailed 2D cross-sectional views of the internal structures and are capable of sub-millimeter gaps between slices. Slices are generated by powerful magnets that rapidly and repeatedly align the structure's hydrogen atoms in two opposing orientations; electrical properties of these alignments are recorded. The alignment time required by the hydrogen atoms varies by structure, resulting in different signal properties and creating contrast in the resulting cross-sectional image. The prevalence of hydrogen atoms in most biological structures means MR scans are capable of capturing high levels of detail for both hard and soft tissues.

By combining a sequence of slices from MRI it was possible to digitally reconstruct a 3D representation of the scanned object (Figure 3.2). In the case of the knee joint, slices of the bone and cartilage for the distal femur, proximal tibia, and patella were masked in their appropriate slices using segmentation software such as ScanIP (Simpleware Exeter, UK). Attachment sites for ligamentous structures were also masked; these included the rectus femoris (RF), patellar ligament (PAT-LIG), medial patellofemoral ligament (MPFL), lateral patellofemoral ligament (LPFL), medial collateral ligament (MCL), superficial medial collateral ligament (sMCL), lateral collateral ligament (LCL), anterior cruciate ligament (ACL), and posterior cruciate ligament (PCL). Although most scans show a clear interface between bone and cartilage,

low resolution of some scans can make it challenging to locate thinner ligaments (e.g. MCL, LCL) and the tapering edges of thicker ligaments. Therefore, it is necessary to have a working knowledge of the anatomy of the knee joint in order to mask the appropriate image features on the MRI slice. Once all slices for a particular structure were masked, a 3D representation was computed; gaps between adjacent slices were interpolated to form a single 3D model. Typically, the resulting 3D model contained imperfections on the surface as a result of large slice gaps or masking inconsistencies due to human error. Filtering techniques to remove these artifacts included filling of cavities, removal of small islands, and surface smoothing via the Recursive Gaussian process to remove erratic (high-frequency) changes in surface contour. Because capturing surface contours were of primary interest, 3D models were further defined by vertices and 2D triangular faces, which were exported separately as stereolithography (STL) files. Structures from a single sequence of MR images were described with respect to that image stack's coordinate system and positioned in space as they were when scanned. The 2D bone surface representations were then imported into Hyperworks (Altair, Troy, MI), a dedicated pre-processing software, where their fine meshes were resampled according to the registration technique discussed in Chapter 3.2.2. Members of the training set were chosen in an effort to describe the broad range of sizes found in the white male and female populations (Figure 3.3). Information regarding the training set demographics, scan information, and study usage may be found in Table 3.1 and Table D.3.

3.2. Development of the Statistical Model

3.2.1. The Template Mesh

Comparison of knee geometries using statistical methods requires correspondence between their mesh representations. Each knee joint was therefore registered to a common template mesh for the bones, cartilage, and ligamentous structures (Figure 3.2). The template for the femur, tibia and patella bones contains 2384, 1101 and 472 nodes, respectively, each with 2D triangular elements approximately 3 mm in length. Since cartilage-to-cartilage contact is often of interest in FE-based studies, the softer articular cartilage of the TF and PF joints was represented with continuum hexahedral elements to create an FE-ready statistical model. The femoral, medial tibial, lateral tibial and patellar cartilages consisted of 2748, 990, 825, 90 and 504 hexahedral elements, respectively. Handles were used to move zones of adjacent nodes and thus represent subject-specific cartilage shape with a consistent mesh.

An anatomic local coordinate system (LCS) was defined for the femur, tibia, and patella bones. These LCS were established based on the articular surface geometry and anatomical landmarks (Rao et al., 2013). The femoral coordinate system was defined by the axis of a cylinder fitted through the flexion facet of the medial and lateral condyles of the femur and the line passing through the centroids of three image slices in the transected diaphysis of the femur (Pandy et al., 1997; Morton et al., 2007). The origin was placed at the midpoint between the medial and lateral epicondylar points. The tibial coordinate system was constructed with the origin at the medial tibial eminence, using lines passing through centroids of three image slices in the transected diaphysis, and

through the centers of the tibial condyles (Morton et al., 2007). The patellar coordinate system was developed using the proximal, distal, and lateral points around the articular periphery with the origin located at the geometric centroid (Morton et al., 2007). Cartilage and ligament attachment sites were defined with respect to their bone's LCS.

3.2.2. Geometry Registration

Registration refers to any process by which segmented shapes of a training set are linked to a common point distribution model (PDM) or template mesh for correspondence, which is required for PCA (Chapter 3.2.4) and the development of an SSM. Cartilage is primarily a 2D structure with a much smaller thickness dimension. By contrast, bones are more uniform in their 3D shape, which makes handling variation less of a challenge for registration protocols. Therefore, two separate registration processes were developed to achieve the best results for bone and cartilage.

Bone registration involves alignment of the training set subjects to the template mesh and employment of an iterative closest point (ICP) algorithm to find nearest-neighbor nodal relationships between the geometries. First, STL meshes of the femur, tibia and patella are aligned to their respective templates; the femur and tibia shafts are then cropped to match the long-axis length of the template mesh. Cropping increases the similarity between the template and specimen meshes and thus, increases the likelihood of improved correspondence. ICP employs several techniques; a nearest-neighbor search with improved efficiency from a kd-tree algorithm, rigid body alignment, and orthotropic scaling to reduce the overall distance between nearest neighbors. The nodes on the template geometry are then assigned the coordinates of their associated target specimen

nodes, effectively representing the specimen's geometry with the template mesh. As each specimen is aligned to the template mesh via ICP, they adopt the template's LCS as their own. This adoption ensures that subsequent size and shape analysis will be independent of relative joint alignments. Joint alignment of the as-scanned position may therefore be defined by the transformation between two bones (Figure 3.1).

Registration of the articulating cartilage is based on similar work by Fitzpatrick et al. was developed to uniformly distribute 2030, 504 and 390 handles on the surface of each subject's segmented femoral, tibial, and patellar cartilages, respectively (Fitzpatrick et al. 2011). A graphical user interface (GUI) provides coronal and transverse views of the 3D segmented STL geometry for landmark point selection (Figure 3.4). Seven landmark points on the femoral cartilage are selected on the cartilage edges above the posterior condyles, corner points on the anterior aspect of the medial and lateral condyles, the intercondylar notch, and distal points on each condyle. Two mediolateral landmark points on each of the tibial cartilages and patellar cartilage define the primary axis along which the algorithm mathematically distributes vertical sets of handles on the attachment and articular surfaces of the cartilage volumes. The algorithm divides the STL meshes into subsections based on these landmark points and distributed handles evenly across the dividing lines. Uniform handle placement is an important component of both correspondence between subjects and the generation of well-formed hexahedral elements for use in FE analyses. Morphing of the template cartilage mesh (Figure 3.5) to a subject-specific shape is achieved by repositioning the template mesh handles to the subject's corresponding handle coordinates. Surrounding internal and surface nodes are

linearly interpolated between adjacent handles to morph and smooth the hex mesh into the subject-specific geometry (Baldwin et al., 2010). Cartilage structures are also described in the coordinate system of the associated bone so as to reduce the effects of alignment variability.

3.2.3. Kinematic Processing

Kinematics of cadaveric knees tested on the KKS are measured by tracking each bone's rigid body marker (Figure 3.1). Rigid body markers are affixed directly to the femur, tibia, and patella and tracked optically (Optotrak, Northern Digital Inc., Waterloo, CA) as they move in the test apparatus. After testing, each bone is cleaned to expose the knee articular surfaces and manually digitized with a hand-held probe. In this way, an outline of the articular surface is recorded with respect to the bone's rigid body marker set. The digitized articular surface is then used to align the specimen mesh geometry and local coordinate system to the rigid body marker's coordinate system in which the experiment was recorded (Figure 3.6). This dissertation uses a femur-fixed coordinate system to define TF and PF kinematics (translation and rotation) of the tibia and patella relative to the femur, respectively. Kinematics are reported using the Grood-Suntay open-chain kinematic descriptors of motion. Correspondence of motion between subjects was based on TF flexion; all other DOF were described with respect to tibial flexion and resampled to a consistent number of data points in order to compare joint motion across the training set.

3.2.4. Principal Component Analysis

Principal Component Analysis (PCA) is a mathematical process meant to describe large datasets of data where patterns and trends are difficult to characterize with simple linear regression models. The goal of PCA is to reduce the dimensionality of the dataset by defining the data based on its covariance (Jolliffe, 2002). By measuring the variability in the dataset, relationships between the data points can be exposed and utilized to explain large subsets of the data with a single quantity.

PCA answers the question, “*Is there another basis, which is a linear combination of the original basis, that best re-expresses our data set?*” (Shlens et al., 2014). To that end, PCA operates on an $n \times N$ dataset, V , which contains N trials or observations each defined by a common set of n variables. The original basis is the coordinate system(s) used to describe the input variables which, in the case of anatomy and kinematics, is the 3D Cartesian coordinate system. While this coordinate system has proven useful in describing clinically relevant shape and function, it is limited in its ability to easily describe underlying patterns or structure in the data. Representation of the dataset, V , in Principal Component space can be defined simply as

$$PV = Y \tag{3.1}$$

where P is an $n \times n$ matrix and each row represents a new basis vector transforming V into Y . Choosing the bases (rows) of P are done so by performing an eigenvalue decomposition on the covariance matrix of the dataset

$$C = \frac{1}{n-1} VV^T \tag{3.2}$$

where C is $n \times n$. The nature of eigenvalue decomposition results in a ranked order of eigenvalues representing principal component variances from largest to smallest. The first eigenvalue describes the largest amount of variability in the data, thus indicating the most important structure. The associated eigenvector describes orientation of the basis or, in terms of shape, the mode by which the most geometric difference exists. In the context of biological structures, this is most often a scaling mode. PC scores are a representation of each training set subject in Principal Component space. Mathematically, each subject of the training set can be described by a vector, v , which is a summation of the mean subject vector, \bar{v} , and k principal components

$$v = \bar{v} + \sum_{i=1}^k p_k * e_k \quad (3.3)$$

where p_k is the k th PC score and e_k is its associated eigenvector. A training set subject may be fully reconstructed by summing together all PC scores to reconstruct the centered data and then adding in the mean variable vector.

If the training set data contains redundant information or in mathematical terms, linearly dependent variables, the off-diagonal components of the covariance matrix will be nonzero. In order to describe the bases containing maximal variance in the dataset, a row matrix of bases, P , are chosen to minimize the off-diagonal terms. While PCA seeks to minimize the off-diagonal terms in order to find the most appropriate bases by which to explain the maximal variance, mathematical redundancy may be a valuable asset when considering biological systems where relationships between variables is expected and important. Applications suggesting the benefits of redundancy were previously discussed in Chapter 2.1.

On large datasets, PCA can be a cumbersome process even for powerful computers requiring a significant amount of memory to calculate full covariance matrices. To reduce the memory requirements of PCA, Matlab® has developed an ‘Economy’ mode where only the eigenvectors associated with nonzero eigenvalues are calculated thus reducing the size of the covariance matrix to a $n \times m$ matrix where m is the number of observations or columns of the original dataset V . Since only the nonzero eigenvalues are relevant to the SSM, there is no loss of information (Turk and Pentland, 1991). Moreover, predictive algorithms developed around PCA do not require the full eigenvector matrix as only the vectors associated with nonzero eigenvalues are utilized in the prediction.

3.2.5. Parallel Analysis

The reorientation of bases that PCA performs on the data to achieve a ranked order of variance begs the question of how many principal components are actually significant and how many describe noise. Noise in the data may be due to factors such as geometric tolerances or measurement tool resolution. In the case of point distribution models, unexplained variance in size and shape of the point clouds contributes to noise and provides no useful information to studies of shape and function. A technique called Parallel Analysis seeks to describe the inherent noise by performing PCA on a set of data where point correspondence is randomized between observations (Ledesma et al., 2007). The technique requires multiple iterations of PCA; for each iteration on the data, observations and variables are randomly reorganized within each variable. The result is a data set of uncorrelated variables on which PCA now tries to define any remaining

structure. The remaining structure is considered noise, which is not likely to contribute valuable information in predictive scenarios. By evaluating multiple randomized sets of the same data, the Parallel Analysis technique calculates 95% confidence bounds on the results (eigenvalues, eigenvectors, and PC scores) for a randomized data set. The number of significant PC scores in the original, correlated dataset is said to be the number of PCs for which explained variance is greater than the variance described by noise (Figure 3.7).

3.3. Visualization of the Statistical Model

PCA describes each specimen in the training set with a set of PC scores and associated eigenvalues and row vectors corresponding to the magnitude and direction by which that specimen differs from the average of the training set. By varying these PC scores according to the standard normal distribution, 3D models and associated kinematics can be generated to represent virtual instances that are different from the actual training set specimen. Although these new instances are limited to the range of variability present in the model, this ability to generate more virtual models is useful to population-based studies where a large cohort of physiologically relevant specimen are required (Bryan et al., 2009). By perturbing one score at a time, each PC mode can be combined with its respective eigenvector (equation 3.3 in section 3.2.4) to return the geometric variables (Figure 3.8) and 6-DOF kinematics (Figure 3.1) for that PC mode. A custom Matlab script organizes 3D geometry variables (Cartesian coordinates) into node sets associated with the element definition of the template bone mesh. The script creates a .tcl command file that operates on the cartilage template hexahedral mesh in Hyperworks (Altair, Troy, MI) to adopt the shape of the cartilage for the given instance (e.g. a

specimen from the training set or a vector of PC scores). TF flexion is the dominant motion in knee joint motion for most activities and, thus, is the most useful measure against which to visualize all other joint motions. This method allows comparisons to be made between specimens who have performed the same activity by “normalizing” their motion to a specimen-specific DOF.

Soft tissue representation is an important component of computational finite element modeling. Ligaments, tendons, and muscles impart tremendous influence on joint loads, kinematics, and ultimately cartilage stress. While accurate models of the knee joint can be represented with 1D ligaments (Baldwin et al., 2009), the development of more complex models i.e. 2D or 3D) can lead to an improved understanding of soft-tissue constraint. 2D and 3D models have been developed and validated (Fitzpatrick et al., 2010; Kiapour et al., 2014); however, model development methods are primarily manual and subject-specific, making large population-based studies impossible.

Accordingly, an algorithm was developed to automatically generate computationally efficient 2D membrane representations for the soft-tissue structures of the knee. The algorithm seamlessly interfaces with the current workflow to process subjects for SSM evaluations. During MR segmentation, attachment sites and lines of action are located for the soft tissue structures described earlier in this chapter. Once the attachment sites have been properly registered to a consistent numbering scheme, a Matlab algorithm conducts a series of interpolations and curve-fits to connect insert and origin sites with 2D curvilinear node sets. For structures such as the posterior capsule, which cannot be located in most MRIs, bony anatomy is used to locate the origin and

insertion sides for these structures according to published literature (Laprade, et al. 2007). These node sets are then organized into the proper arrays and associated with element sets, which include membrane, rotary inertia, mass, and spring element types. The result is a 2D representation of the soft tissue structures surrounding the knee joint (Figure 3.8). The benefit of this approach is three-fold: only attachment sites and lines-of-action need to be segmented, no manual meshing is required, and registration of attachment sites is an efficient way to describe soft-tissue geometric data in statistical models.

3.4. Explicit Finite Element Evaluation of the Statistical Model

Population-based FE evaluations require efficient development of unique virtual models for the knee. This section describes a high-level evaluation of kinematic and contact mechanics on a natural knee model developed from an SSM. The SSM included bone, cartilage, ligament attachment sites, and experimental kinematics. The FE model was constructed using the methods described above and evaluated in a dynamic simulation with Abaqus/ExplicitTM 11.3-1 (Dassault Systemes, Providence, RI). The 3D model represented the mean geometry of the SSM where all PC scores were set to zero (Figure 3.9). The femoral, tibial, and patellar bones were represented with 2D triangular meshes. The associated cartilage structures were represented with 3D hexahedral elements. In the analysis, bones and cartilage were considered rigid structures. Contact between the cartilage structures was defined by a pressure-overclosure relationship with a slope equal to 3.2 and friction coefficient of 0.04 (Halloran et al., 2005).

The RF, VASTI, PL, MPFL, LPFL, MCL, sMCL and LCL ligaments were used to constrain the knee joint. Each structure was generated by the automated ligament

generation algorithm described in the previous section, which consisted of deformable hyperelastic 2D membrane elements. Material properties were represented by uni-axial tension properties from literature values (Stäubli et al., 1999). ACL and PCL ligaments were modeled as 1D spring elements. Linear actuators representing the quadriceps muscles were attached to the proximal portions of the VASTI and RF tendons to distribute a quadriceps load across the actuators according to physiological cross-sectional area (RF=15%, VI=20%, VLL=35%, VLO=10%, VML=15%, VMO=10%) and orientations described in the literature (Farahmand et al., 1998). Linear actuators at the insertion sites were used to bring ligaments into initial tension during the settling step of the analysis.

The simulated loading conditions consisted of average experimental kinematics from the testing of 20 cadavers in a simulated squat cycle on the KKS. The full experimental data are discussed in Chapter 4. The model started in the average initial alignment position and was driven primarily by TF flexion; TF AP and IE motions were also prescribed; however, all other DOF for the TF and PF joints were left free. The PF joint was constrained by the geometry of the femur trochlear groove and several ligamentous structures including the PAT-LIG, MPFL, LPFL, RF, and VASTI. A simulated quadriceps load of 1000 N was ramped during the flexion cycle to maintain the patella to the trochlear groove. A compressive load on the TF joint of 1000 N was also applied to constrain the tibia in the ML direction. AP and IE were constrained by averaging the motions across experimental results from the KKS cadaver study.

Tibial and patellar kinematics were described using the open-chain description of motion (Grood and Suntay 1983). PF kinematics shows similar trends between the FE and experimental results (Figure 3.10), which illustrates the utility of the cartilage and ligament morphing algorithms to efficiently generate suitable geometry. The hexahedral cartilage reasonably described joint contact mechanics, illustrating the ability of the cartilage template to morph and preserve element shape (Figure 3.11). The evaluation performed here illustrates the ability of an SSM to develop FE-ready geometries for population-based and subject-specific natural knee evaluations.

3.5. Automated Measurements on the SSM and its Training Set

A consistent method for measuring geometry and kinematic alignment of the knee joint is crucial to understanding population variability and the relevant relationships to function. A computational tool was developed to automate the process of obtaining these measurements on the training set and subsequent instances of the SSM. The tool included clinically relevant measurements such as femur epicondylar width, femur anterior sulcus angle, femur medial and lateral trochlear angle, bisect offset, tibial posterior slope, tibial tuberosity-trochlear groove (TT-TG), patella angle, and the Insall-Salvati index (Figure 3.12). Other measures refer to geometric features that are less common clinically but provide insight into the goals of this research (Mahfouz et al., 2012; Stefanik et al., 2013). These measures included femur trochlear angle, distal sulcus angle, distal condylar angle, sulcus groove height, sulcus width, width of the intercondylar notch, antero-inferior sulcus angle, and anterior-posterior to medial-lateral distance ratios. Kinematic measures included initial and flexion-specific alignment as

well as range-of-motion (ROM) in all 6-DOF. By registering all training set geometries to a common LCS, two positions are available on which to take measurements: within the LCS for a particular bone or in a specimen-specific flexion-angle alignment. For example, an accurate Insall-Salvati index requires patellar height and patellar tendon length measurements. Patellar tendon length is estimated as the distance between the most distal point on the patellar apex and the tibial tuberosity. Patellar height, however, is measured with the bone in its LCS so as to reduce the effects of variability in alignment (namely flexion) and provide a consistent position for all patellae for such a measurement.

3.6. Building 3D Models from Radiographs using Statistical Modeling

The high speed stereo radiography (HSSR) system at the University of Denver is capable of capturing *in vivo* dynamic motion of the skeletal system in two independent image planes (Figure 3.13). High speed cameras in each perspective are synced to provide sequences of linked radiographic images for subsequent 3D tracking of bones and, in patients with TKRs, metallic components. In the natural case, bone segmentation from MR or CT scans provides the 3D geometry for tracking. Chapter 2 discussed algorithms that have reconstructed 3D natural femur and tibia bone geometry directly from the radiographic images using SSMs and automatic edge detection methods. This section describes a new digitization process to extract the visible edges of an object and object plane using XMA Lab (Version 1.2.18, XROMM, Brown University). The process is suitable for the resected patellar bone and thus makes reference to that application.

XMALab is a free, downloadable program that was developed to digitize and track points on moving objects from a series of biplane fluoroscopic images. The program processes all of the HSSR system files to perform undistortion, calibration, and associated direct linear transformation (DLT) coefficient calculations. DLT coefficients describe the 3D-2D transformation between a 3D object and its 2D projection onto an image plane (Brainerd et al., 2010). In a biplane setup, the coordinates of a projected point in image planes A and B are defined by the equations

$$u_A = \frac{A_1x + A_2y + A_3z + A_4}{A_9x + A_{10}y + A_{11}z + 1} \quad (3.4)$$

$$v_A = \frac{A_5x + A_6y + A_7z + A_8}{A_9x + A_{10}y + A_{11}z + 1} \quad (3.5)$$

$$u_B = \frac{B_1x + B_2y + B_3z + B_4}{B_9x + B_{10}y + B_{11}z + 1} \quad (3.6)$$

$$v_B = \frac{B_5x + B_6y + B_7z + B_8}{B_9x + B_{10}y + B_{11}z + 1} \quad (3.7)$$

where the coefficients, A_i and B_i ($i = 1$ to 22), make up the DLT that transforms 3D coordinates (x, y, z) into 2D image plane coordinates $u_A, v_A, u_B,$ and v_B , for cameras A and B, respectively. Estimation of these coefficients is conducted by solving a system of equations that describe the known calibration cube points in the image planes. Chapter 6 uses the DLTs to project an SSM instance on the camera image planes.

The utility of XMALab is illustrated by its ability to describe object edges from both camera views with a single set of 3D points. The edges of an object in each camera are independent projections based on the configuration of the x-ray sources and cameras and therefore cannot be used to directly digitize the surface of the object for direct 3D point matching. This is the fundamental difference between digitization of edges and

points. During edge digitization, a point selected on the outer profile of the object in one camera view yields an epipolar line in the other camera view that intersects the object twice. Since the goal is to reconstruct a single set of 3D points to represent any part of the object profile, selection of either one of the intersections is valid.

In scenarios where digitization of a plane (e.g. patellar implant resection cut) is required, a method was developed to extract the plane from a single pair of images. The object plane must be perpendicular to the both image planes and three points must be selected to define the location and orientation of the plane (Figure 3.14). Figure 3.14 illustrates the sequence by which points may be selected on each image plane to create the triangle. A more detailed protocol on the use of XMA Lab to create the digitized points file and DLT coefficients is presented in Appendix B.

Alignment of an SSM instance to the digitized points of an object is achieved by first projecting the instance's 3D surface point cloud onto both image planes via the DLTs. The resulting projections are 2D point-filled patches in the image plane whose boundaries represent the edges of the instance. An alpha shapes algorithm operates on the patch to determine which points describe the boundaries and which points are considered internal. Alpha shapes are a generalization of the convex hull and useful for outlining point clouds with varying levels of complexity (Edelsbrunner et al., 1983). The algorithm is an expansion of Delaunay triangulation in which a characteristic radius controls which adjacent points across the entire patch are connected, creating a well-formed network of triangles, or faces. The additional component of the alpha shapes

algorithm then analyzes the triangulated patch, eliminating the triangle sides that are shared, which indicates an interior edge, thereby isolating the boundary of the patch.

Table 3.1 Scan data and research study usage.

Source	Qty.	Chapters	In-plane Resolution & Slice Thickness (mm)	Protocol
Osteoarthritis Initiative (OAI)	25	Patellar Prediction <i>Chapter 6</i> Cartilage Prediction <i>Chapter 7</i>	0.36 x 0.70	SAG 3D DESS WE
University of Kansas & DePuy-Synthes	20	Shape-Kinematics <i>Chapter 4</i> Patellar Prediction <i>Chapter 6</i> Cartilage Prediction <i>Chapter 7</i>	0.35 x 1.00	t2.trufi3d.we.SAG NEW
University of Denver & Depuy-Synthes	5	Patellar Prediction <i>Chapter 6</i> Cartilage Prediction <i>Chapter 7</i>	0.35 x 1.00	t2.trufi3d.we.SAG NEW t2.fi3d.fs.SAG

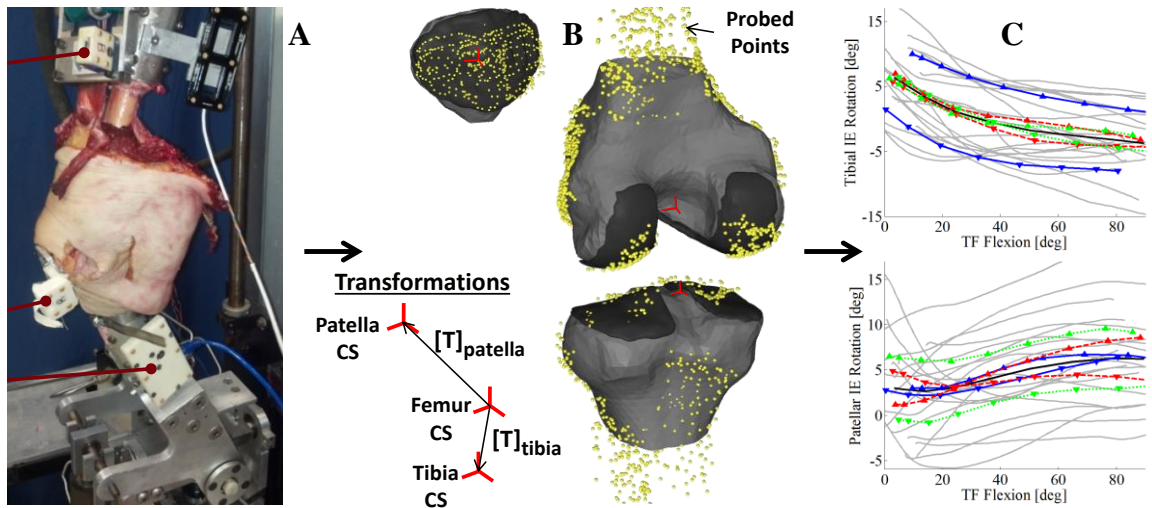


Figure 3.1 The process of extracting joint kinematics for the statistical shape and function model: Rigid body markers (white) fixed to the femur, tibia, and patella are tracked during *in vitro* cadaveric knee testing (A). Alignment of specimen-specific geometry (gray) and local anatomical coordinate systems (red) to probed cadaver surface points (yellow) defines position of the bones with respect to the rigid bodies. Grood-Suntay open-chain kinematics are calculated from the relative motion of the local bone coordinate systems (C).

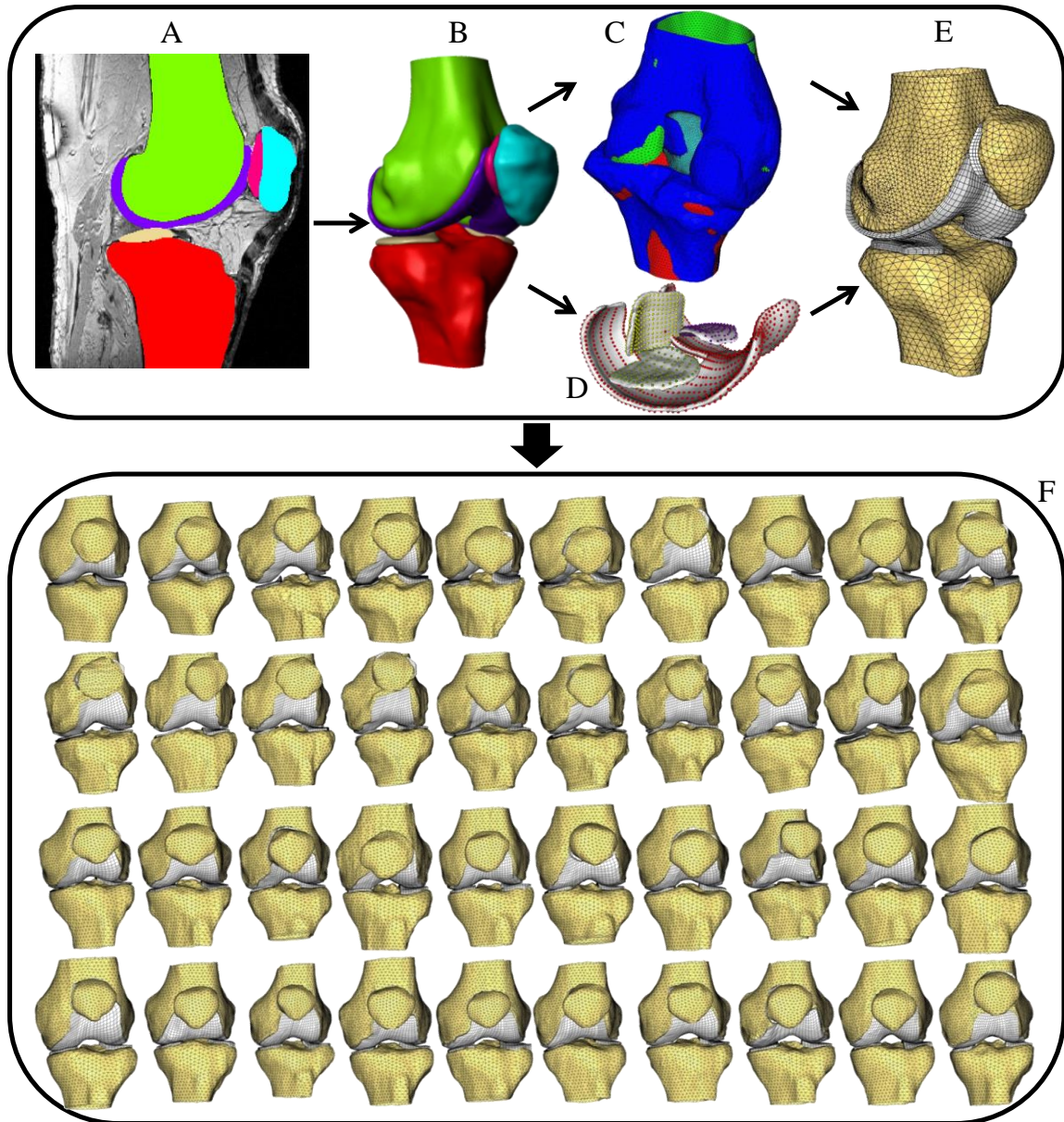


Figure 3.2 The process of building a training set for the statistical shape model: Segmentation of a MR scan (A), the resulting 3D stereolithography model (B), alignment to bone template mesh (C) and handle placement on articular cartilage (D), “as-scanned” alignment of template mesh-registered specimen-specific geometry (E), Completed training set of 40 specimens (F).

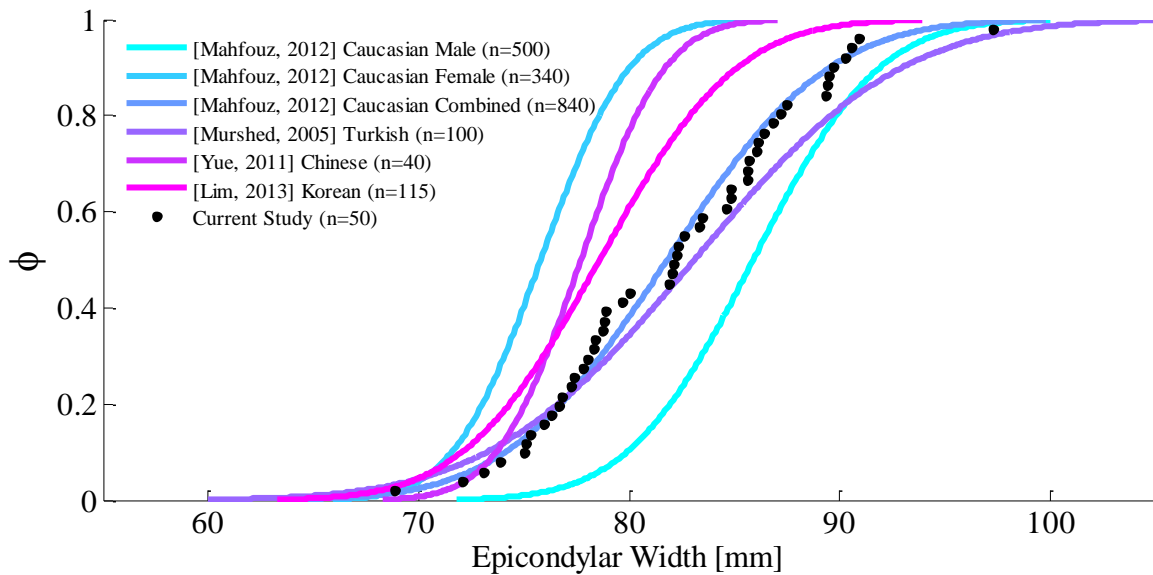


Figure 3.3 A comparison of the cumulative distribution functions (CDF) for the femur epicondylar width measurement across multiple populations shows a similar range of geometric size in the current training set.

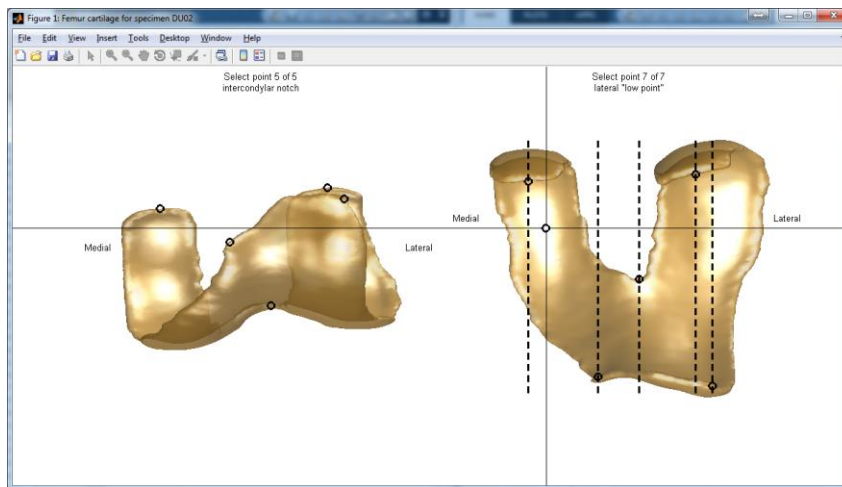


Figure 3.4 Cartilage registration graphical user interface (GUI) with representative femur cartilage from segmentation. Black points represent the manually selected landmark sites to guide the placement of surface handles on the stereolithography (STL) mesh.

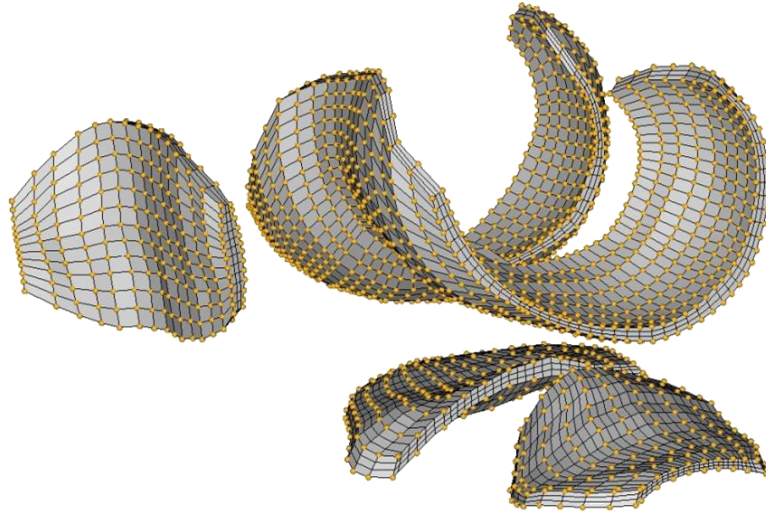


Figure 3.5 Template hexahedral cartilage mesh with surface handles (yellow) (Baldwin et al., 2010).

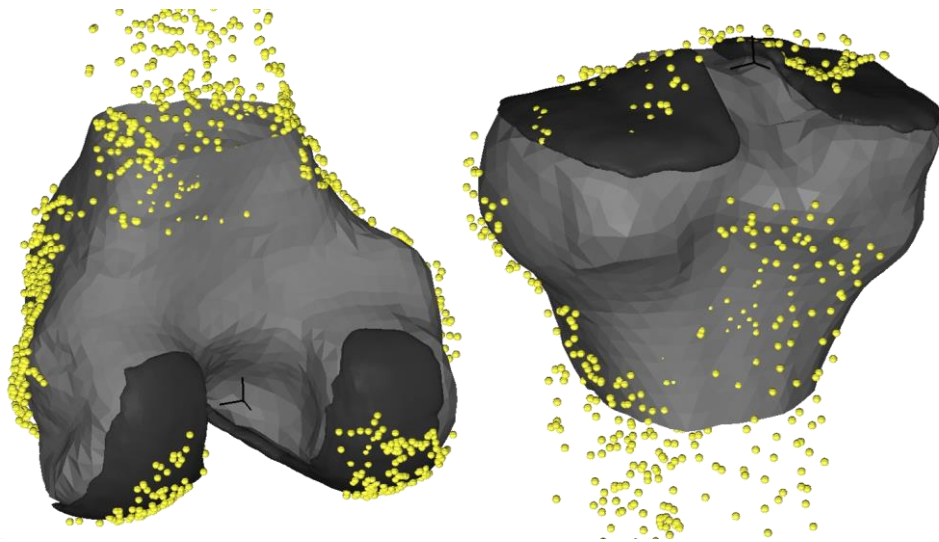


Figure 3.6 Alignment of registered specimen-specific geometry to their digitized position (yellow points) in the Kansas Knee Simulator (KKS).

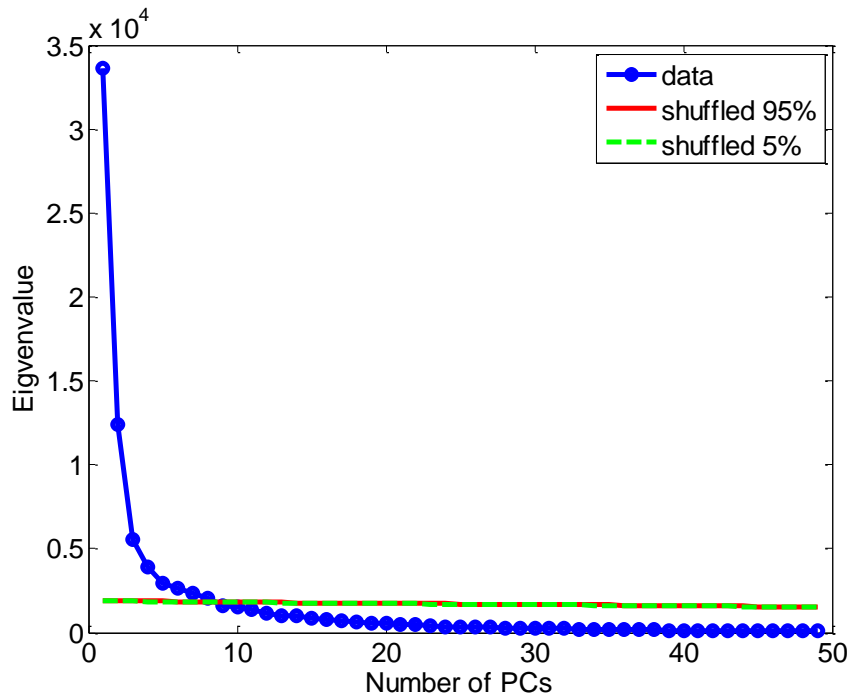


Figure 3.7 Eigenvalues for each principal component (PC) are ranked by magnitude (variance). The number of significant PCs in a model (blue) are those with variances greater than the variances in 5-95% bounds of models built from randomized instances of the same dataset (green and red).

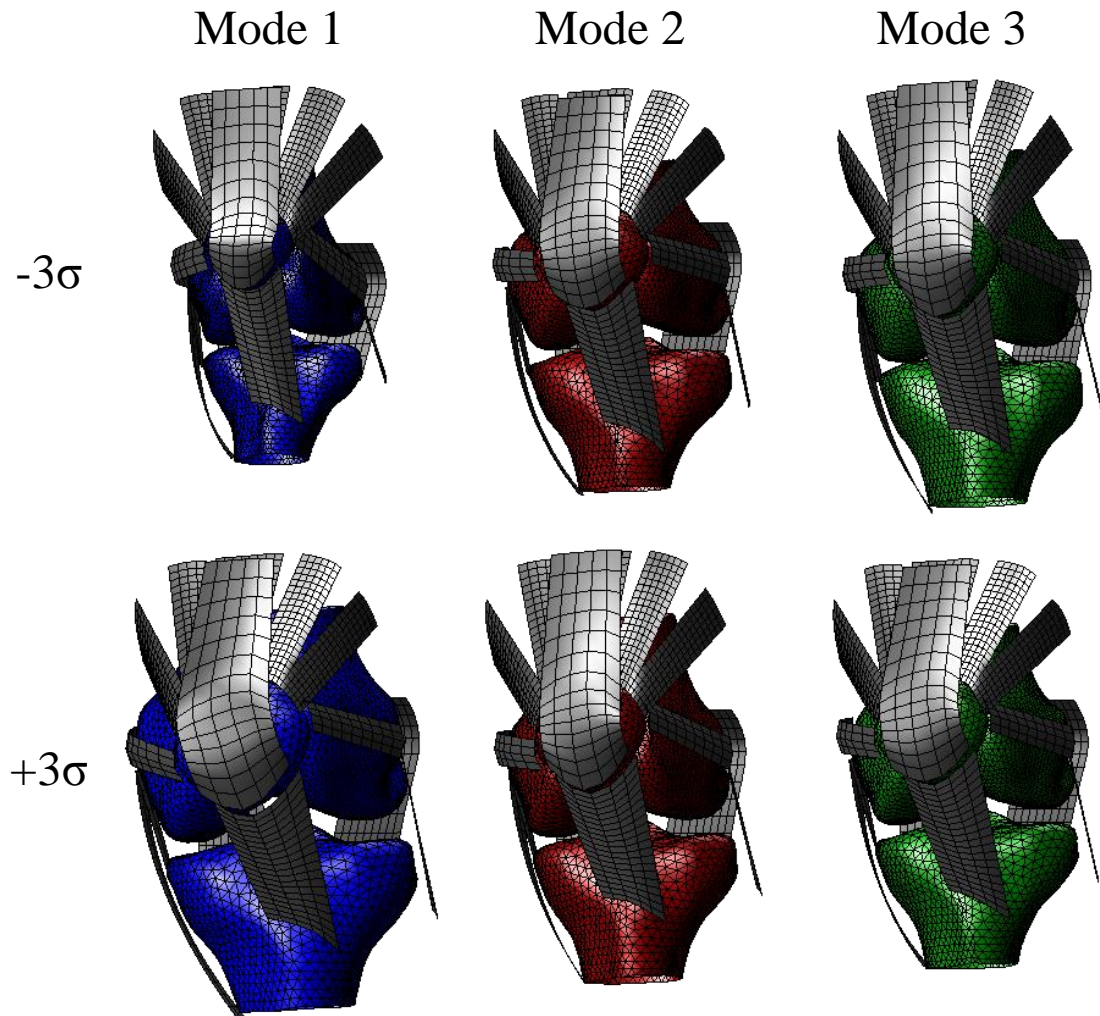


Figure 3.8 The automated ligament morphing algorithm wrapped soft tissue structures (gray) around the first three principal component shapes of bone for a representative SSM. Structures shown include the rectus femoris (RF), vasti, patellar ligament (PAT-LIG), medial collateral ligament (MCL), superficial MCL (sMCL), lateral collateral ligament (LCL), medial and lateral patellofemoral (MPFL and LPFL), and posterior capsules (PCAP).

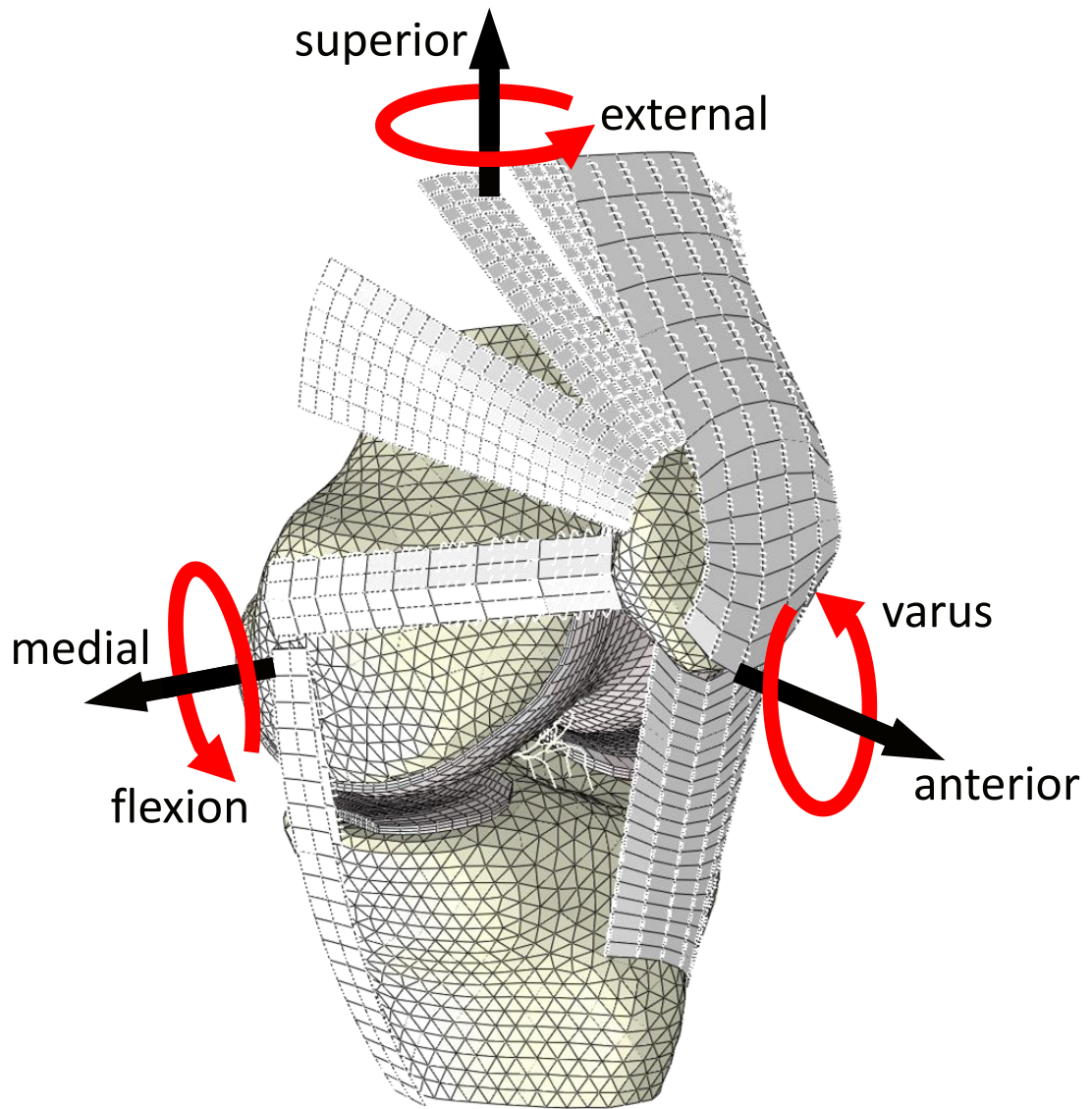


Figure 3.9 FE model of the mean geometry used in the computational analysis. The position shown is in initial alignment of approximately 15 degrees.

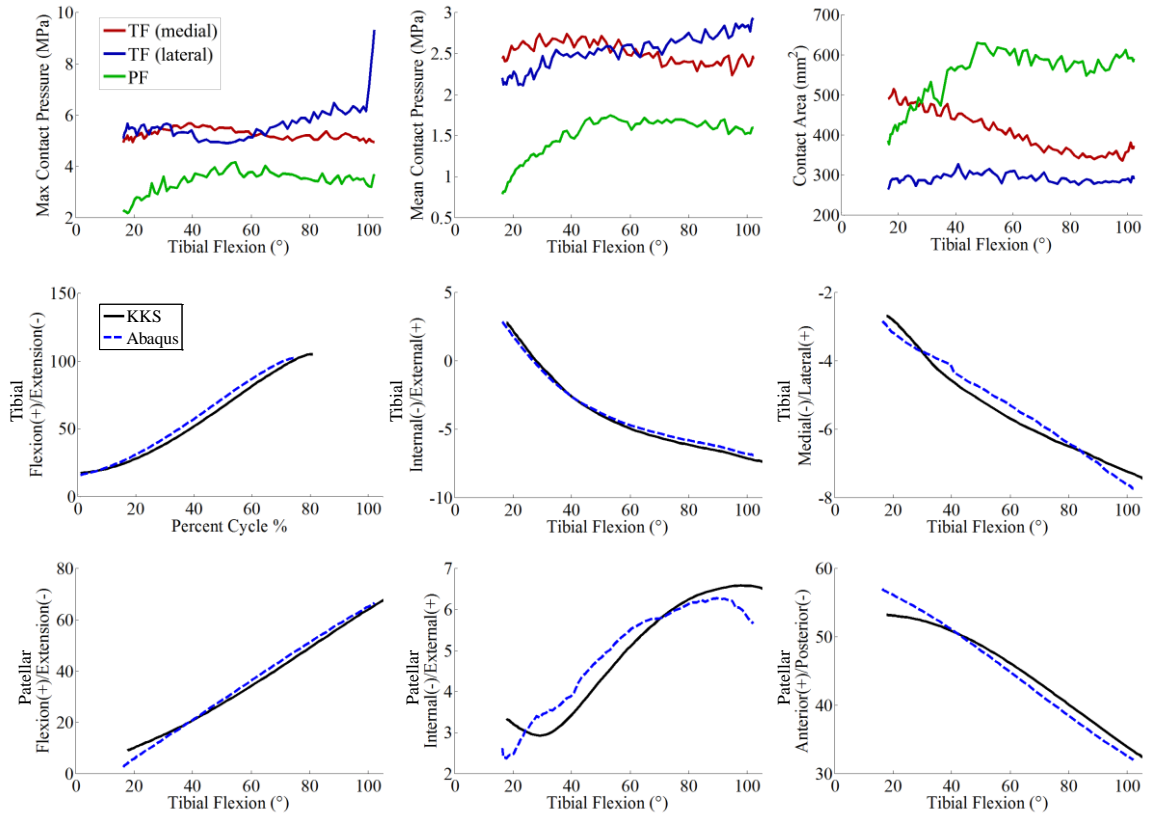


Figure 3.10 Kinematics and contact mechanics for the mean geometry. Maximum contact pressure, mean contact pressure, and contact area (top) for the TF and PF joints. Imposed KKS (black) and measured Abaqus (blue) tibial kinematics (middle) and patellar kinematics (bottom).

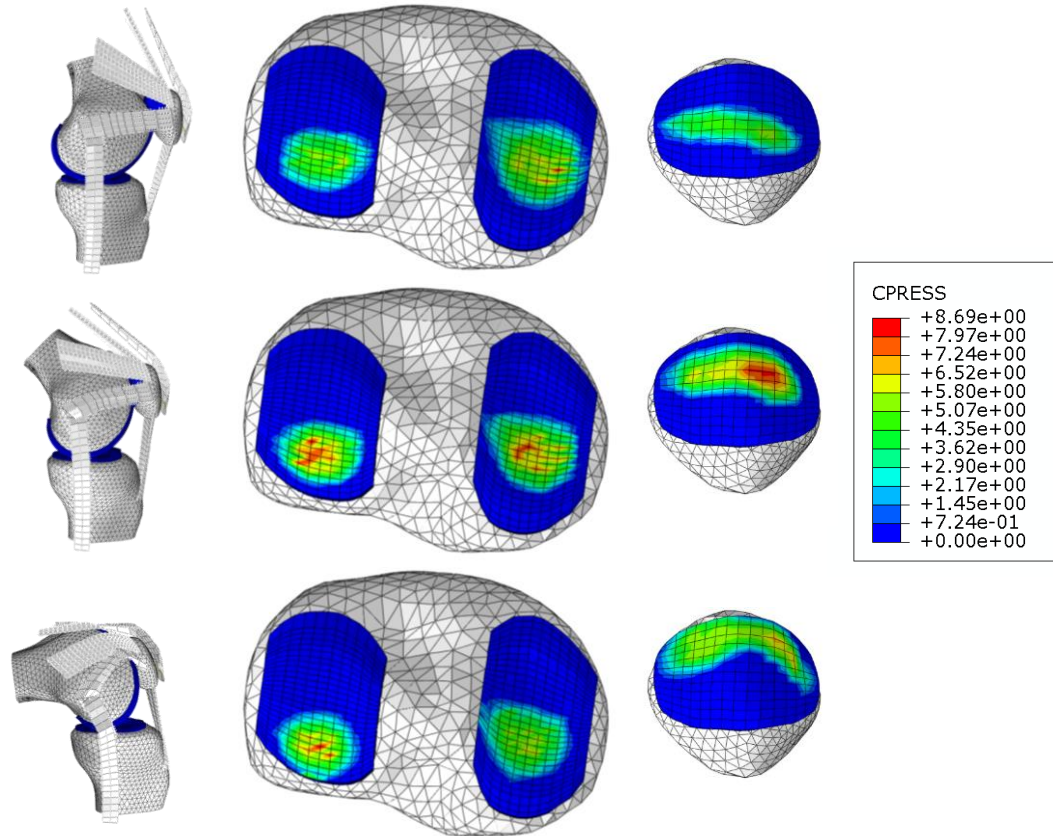


Figure 3.11 Contour maps of the contact pressures from the FE analysis for the tibia and patellar cartilages. The full geometry on the left shows the relative position of the joint for each of the three flexion angles.

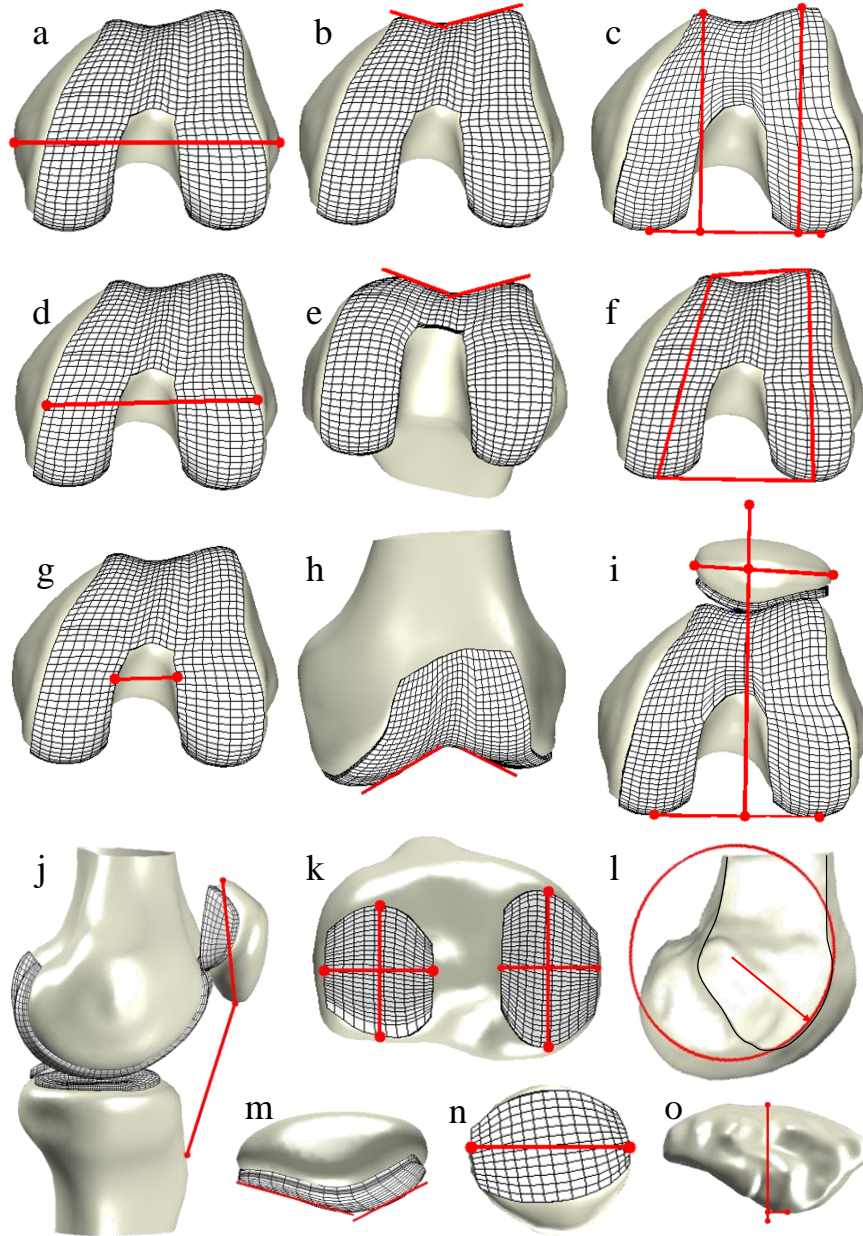


Figure 3.12 Illustrations of some of the automated linear measures: epicondylar width (a), anterior sulcus angle (b), sulcus width (c), cartilage width along epicondylar axis (d), antero-inferior sulcus angle (e), condylar ML and AP widths (f), intercondylar notch width at the distal aspect (g), distal sulcus angle (h), bisect offset (i), Insall-Salvati index (j), tibial cartilage ML and AP widths (k), trochlear groove radius of curvature (l), patellar angle (m), patellar ML width (n), and patellar ridge medialization (o).

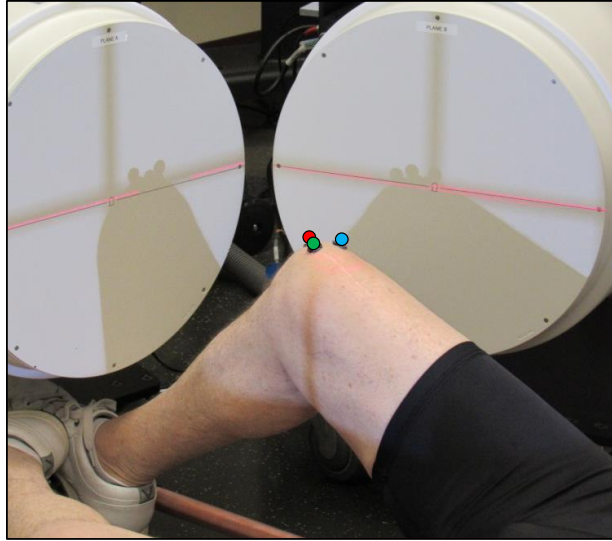


Figure 3.13 Orientation of a right knee in the HSSR for imaging. Light sources at the X-ray generators create a shadow of the object on the image-intensifiers to aid in alignment of the knee.

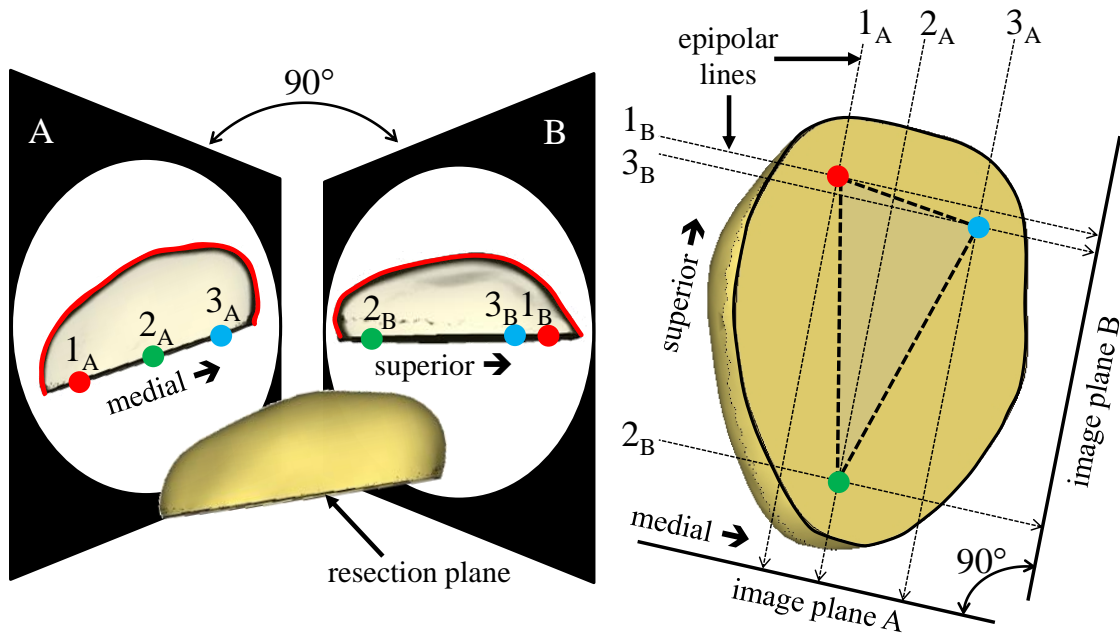


Figure 3.14 Digitization of the resection plane from stereo radiographic images (left) for the implanted patellar bone. Epipolar lines 1_A-3_A are projected across image plane B to inform the selection of associated points, 1_B-3_B , on the resection plane projection. The resulting 3D position of the points (red, green, blue) represents the resection plane in the patellar local coordinate system (right).

CHAPTER 4. STATISTICAL MODELING TO CHARACTERIZE RELATIONSHIPS BETWEEN KNEE ANATOMY AND KINEMATICS

4.1. Abstract

The mechanics of the knee are complex and dependent on the shape of the articular surfaces and their relative alignment. Insight into how anatomy relates to kinematics can establish biomechanical norms, support the diagnosis and treatment of various pathologies (e.g. patellar maltracking) and inform implant design. Prior studies have used correlations to identify anatomical measures related to specific motions. The objective of this study was to describe relationships between knee anatomy and tibiofemoral (TF) and patellofemoral (PF) kinematics using a statistical shape and function modeling approach. A principal component (PC) analysis was performed on a 20-specimen dataset consisting of shape of the bone and cartilage for the femur, tibia and patella derived from imaging and 6 degree-of-freedom TF and PF kinematics from cadaveric testing during a simulated squat. The PC modes characterized links between anatomy and kinematics; the first mode captured scaling and shape changes in the condylar radii and their influence on TF anterior-posterior translation, internal-external rotation, and the location of the femoral lowest point. Subsequent modes described relations in patella shape and alta/baja alignment impacting PF kinematics. The complex

interactions described with the data-driven statistical approach provide insight into knee mechanics that is useful clinically and in implant design.

4.2. Introduction

“*Form ever follows function*” is the credo in design attributed to architect Louis Sullivan. Shape of the articular geometry is known to influence the mechanics of the knee (Iwaki et al., 2000; Eckhoff et al., 2001; Martelli et al., 2002; Varadarajan et al., 2010) and differences in knee morphology have been shown to exist across the population (Yue et al., 2011; Mahfouz et al., 2012). Accordingly, the anatomy and function of the structures of the knee have been well studied to establish biomechanical norms, diagnose pathology, guide surgical treatments, and inform implant design (Dennis et al., 2011; Pal et al., 2013; Clary et al., 2013).

Knee kinematics are measured from *in vitro* cadaveric experiments (Farahmand et al., 2004; Amis et al., 2006; Maletsky et al., 2005; Baldwin et al., 2009) and *in vivo* data collections with fluoroscopy (Dennis et al., 2001; Li et al., 2004) and open magnetic resonance (MR) imaging (Pal et al., 2013; Harbaugh et al., 2010). Subject-specific kinematics are described after registering representations of the anatomy derived from MR or computed tomography (CT) imaging. The kinematics of the knee are characterized by a combination of sliding and rotation marked by anterior translation and internal rotation of the tibia relative to the femur combined with lateral translation and external rotation of the patella relative to the femur during flexion (Freeman et al., 2005; Masouros et al., 2010).

Prior research has investigated relationships between anatomy and functional behavior. Freeman et al. described sagittal plane condylar geometry as a sequence of arcs with different radii that interact with a flat medial and convex lateral tibial plateau (Freeman et al., 2005). Due to varying radii, tibiofemoral (TF) conformity changes during flexion and the medial condyle remains relatively motionless while the lateral condyle translates posteriorly on the tibia, contributing to characteristic tibial rotation. In the natural knee, Hoshino et al. identified correlations between the condylar offset ratio and anterior-posterior (AP) translation and between condylar twist angle and internal-external (IE) rotation (Hoshino et al., 2012). While considering total knee replacement (TKR) implants, Clary et al. investigated abrupt versus gradually reducing changes in the femoral sagittal radius of curvature and their impact on TF AP motion, particularly at mid-flexion (Clary et al., 2013).

Incorporating the patellofemoral (PF) joint, Li et al. described the effects of TF rotation on PF contact mechanics (Li et al., 2004). Other studies have used image-based measurements of the articular surface of the patella and femoral trochlear groove to investigate differences between patellar pain or maltracking groups and normal subjects. Correlations have been identified between patellar kinematics and depth of the trochlea or sulcus angle (Powers et al., 2000). Considering lateral and nonlateral maltrackers and controls, Harbaugh et al. found morphological differences in sulcus angle, patellar height, articular cartilage depth, and lateral trochlear inclination (the angle between the tangent to the lateral trochlear edge and posterior condylar line) between groups (Harbaugh et al., 2010). Recently, Pal et al. showed that patellar maltracking in early flexion was more

prevalent in patellar pain subjects than in pain-free subjects, with the patellar pain cohort having more alta patellar alignment (Pal et al., 2013). While correlations importantly identify influential parameters, they do not quantitatively define the relationships or provide thresholds for diagnosis. Freedman and Sheehan applied a regression-based approach to predict three-dimensional (3D) PF kinematics from two-dimensional (2D) static measures of geometry and alignment, although the technique was not able to fully predict the kinematic results (Freedman et al., 2013).

As an alternative to 2D measurements, Fitzpatrick et al. applied principal component analysis (PCA) to investigate relationships between shape morphology represented by a statistical shape model (SSM) and PF kinematics predicted by finite element analysis (Fitzpatrick et al., 2011). Statistical or active shape models quantify the variation between members of a population (Cootes et al., 1995; Behiels et al., 2002), and have been used previously to characterize variability in bone morphology and density (Bryan et al., 2010; Shim et al., 2008). Prior SSM studies have focused on individual bones with applications to fracture risk (Bryan et al., 2009; Fritscher et al., 2009) and sizing lines for implants (Fitzpatrick et al., 2007; Dai et al., 2013). Recently, statistical models have been applied to consider multiple structures of a joint (Baldwin et al., 2010; Bredbenner et al., 2010; Rao et al., 2013).

As imaging is typically part of the kinematic measurement process, there is an opportunity to use the combination of anatomy and kinematic data to gain insight into the functional interactions of the knee joint in a more holistic way. Accordingly, the objectives of this study were to characterize relationships between knee anatomy and

kinematics using a *statistical shape and function modeling* approach. The current approach is unique in that the PC modes defining the relationships between anatomy and kinematics are determined from the data, in contrast to other studies which required *a priori* identification of the anatomical measure and kinematic output to be investigated. Further, the statistical shape model more fully accounts for the geometry and alignment by using the complete articular geometry instead of a limited set of linear measurements. Lastly, the approach enables the prediction of kinematics for a knee's geometry, which is not possible with correlation-based evaluations.

4.3. Methods

This study utilized a combination of imaging and *in vitro* kinematic data from a cohort of 20 cadaveric specimens to develop a statistical shape and kinematics model of the knee joint (Figure 4.1). The specimens were male with an average age of 64 years (range: 44 to 80), average weight of 78 kg (range: 60 to 127 kg) and average body mass index (BMI) of 25 (range: 19 to 41). The specimens were all considered healthy normal with no signs of osteoarthritis; cartilage, ligaments and menisci were all intact. Each specimen was imaged using MR (Siemens Avanto 1.5T, 3D balanced gradient echo sequence, centered on a 150 mm field of view, in-plane resolution of 0.35 mm, axial slice thickness of 1 mm) and subsequently tested in the Kansas knee simulator under a simulated squat activity (Maletsky et al., 2005). The loading condition used a combination of load-controlled actuators at a simulated hip and ankle and a position-controlled quadriceps actuator to simulate a 90° knee bend (Baldwin et al., 2009). An

Optotrak motion capture system (Northern Digital Inc., Waterloo, CA) recorded the movement of rigid body markers attached to the femur, tibia and patella.

Bone and cartilage geometry for the femur, tibia and patella were reconstructed from the MR images using ScanIP (Simpleware, Exeter, UK). A template mesh, including local anatomic coordinate systems, was developed for the median subject (Rao et al. 2013). An iterative closest point (ICP) algorithm registered each knee to the template mesh resulting in a consistent mesh and coordinate system for all specimens (Figure 4.2). The bone template mesh contained 2384, 1101 and 472 nodes for the femur, tibia and patella, respectively. A template hexahedral mesh of each cartilage structure was morphed for each specimen using a mesh-morphing approach with Hyperworks (Altair, Troy, MI) (Baldwin et al., 2010).

The local anatomic coordinate systems for each bone were established based on the articular surface geometry and anatomical landmarks (Rao et al., 2013). The femoral coordinate system was defined by the axis of a cylinder fit through the flexion facet of the medial and lateral condyles of the femur and the line passing through the centroids of three image slices in the transected diaphysis of the femur (Pandy et al., 1997; Morton et al., 2007). The origin was located at the midpoint between the medial and lateral epicondylar points. The tibial coordinate system was constructed with the origin at the medial tibial eminence, using lines passing through centroids of three image slices in the transected diaphysis, and through the centers of the tibial condyles (Morton et al., 2007). The patellar coordinate system was developed using the proximal, distal, and lateral points around the articular periphery with the origin located at the geometric centroid

(Morton et al., 2007). Experimentally-measured kinematics from the squat cycle were converted to 6 degree-of-freedom (DOF) TF and PF kinematics using a three-cylindrical open-chain description of motion (Grood and Suntay, 1983). Joint kinematic data for all specimens were normalized from 0 (0° flexion) to 100% (90° flexion) of the cycle and discretized at 1% intervals for each DOF.

The *statistical shape-function model* was established by applying PCA to the training set data consisting of nodal coordinates (3D Cartesian coordinates for each node in its local coordinate system) for each bone and cartilage structure and discretized TF and PF kinematics (101 points for each DOF). The array of raw data, V , consisted of an $n \times N$ matrix with n corresponding variables (18153 describing shape and 1212 describing kinematics) for N specimens. PCA was performed on the covariance matrix of V ; PCA is a widely-used statistical technique to decompose a large data set into its primary modes of variation or principal components. The analyses resulted in a series of non-zero eigenvalues characterizing the amount of variability explained and associated eigenvector matrix, E . Each of the subjects was represented by a series of PC scores, P . Note: ' corresponds to transpose, which is equivalent to the inverse for an orthogonal matrix.

V = raw data containing subjects ($n \times N$)

where $v = (n \times 1) = \{v_{shape} \ v_{kinematics}\}'$ for one subject

C = covariance matrix ($n \times n$) of V

E = eigenvector matrix ($n \times N-1$) from PCA on C for non-zero eigenvalues

$$E = \begin{Bmatrix} E_{shape} \\ E_{kinematics} \end{Bmatrix}$$

$$P = v' * E = \text{PC scores (1 x } N-1) \text{ for one subject}$$

$$v' = P * E' = \text{subject representation (1 x } n)$$

The modes of variation were perturbed by +/- 1.5 standard deviations (denoted hereafter simply by + or -) from the mean to visualize the changes in size, shape, alignment or initial position, and kinematics through the squat cycle. This level was set to balance emphasizing the geometric differences, while maintaining realistic instances given the size of the training set. As a composite of the AP and IE kinematics and to enable comparisons to *in vivo* studies, the location of TF contact was estimated using the lowest point on the medial and lateral femoral condyles relative to the tibial SI axis (Banks et al., 2003; Dennis et al., 2005). To describe variations in shape and alignment, a series of measurements used commonly in clinical and radiographic assessments were automatedly performed on the 3D representation; measurements included epicondylar width, Insall-Salvati index, sulcus angle, and bisect offset (Insall and Salvati, 1971; Kalichman et al., 2007; Pal et al., 2011; Stefanik et al., 2013) (Table 4.1¹). Pearson's correlation coefficients were computed between the measurements and PC scores representing each specimen, as well as between the measurements, initial alignment and range of motion (ROM) kinematics.

Lastly, a leave-one-out (LOO) evaluation was performed to assess the ability of the model to predict the shape and kinematics of a new subject from outside of the training set. To perform kinematic predictions from the geometry of a new or left-out subject, an approach similar to Fitzpatrick et al. was applied (Fitzpatrick et al., 2011).

¹ See Appendix B for measurement descriptions.

The geometry was described as the shape-only variables of the raw subject vector (v_{shape}). Using the shape portion of the eigenvectors, the shape representation was transformed into PC scores (P_{new}) corresponding to each mode. Then, the PC scores and full eigenvector matrix were used to predict the shape and kinematic vector for the new specimen. All PC modes were utilized in these predictions.

$$P_{\text{new}} = v_{\text{new shape}}' * E_{\text{shape}} = (1 \times n_{\text{shape}}) * (n_{\text{shape}} \times N-I) = (1 \times N-I)$$

$$v_{\text{new}}' = \{v_{\text{new shape}} \ v_{\text{new kinematics}}\}' = P_{\text{new}} * E'$$

$$= (1 \times N-I) * (N-I \times n) = (1 \times n)$$

Mean absolute errors were calculated between actual and model-estimated shape and location of the lowest contact point.

4.4. Results

The statistical model identified relationships between shape and kinematic variation in the training set as a series of modes of variation. As the earliest modes captured the largest amount of variability in the data, they are emphasized here. For example, the first 3 modes of variation explained 49.0% of the variability, with 6, 15 and 19 modes capturing 69.4%, 95.1% and 100%, respectively (Table B.1). By perturbing individual modes, the corresponding changes in anatomy and TF and PF kinematics are shown in Figure 4.4 and Figure 4.5² for Modes 1-3 and in Appendix B for Modes 4-6. Additionally, correlations described the shape and kinematic parameters captured in each mode (Table 4.2).

² Absolute and relative kinematics for all degrees of freedom are presented in Appendix B, Figure B.1 & Figure B.2.

In addition to describing scaling of the knee (Figure 4.3), Mode 1 captured changes in the medial and lateral AP condylar geometry, AP and IE kinematics and the location of the lowest contact point (Figure 4.4 and Figure 4.6). The sagittal radius of curvature for the medial condyle scaled uniformly between Mode 1+ and Mode 1- (Figure 4.6). The sagittal radius for the lateral condyle was relatively constant between 20° and 50° flexion, albeit with offset centers, but varied in deeper flexion (Figure 6); between 60° and 90° flexion, the radius of curvature for the lateral condyle was up to 1.45X larger for Mode 1+, while it remained relatively constant (within 0.96X) over the same range for Mode 1-. The initial TF position of the Mode 1+ (larger) knee was more flexed, external, and posterior compared to the Mode 1- (smaller) knee (Figure 4.4). During the flexion cycle, both knees rotated internally a similar amount; however, the majority of the motion occurred in early flexion for the Mode 1- knee. The Mode 1+ knee exhibited a steady anterior tibial motion with flexion, while the tibia initially moved anteriorly, followed by posterior translation after 20° flexion for the Mode 1- knee. The lowest point data showed little motion of the medial contact point, while the lateral contact point moved posteriorly, capturing the differences in the amount of IE rotation in early flexion with Mode 1 (Figure 4.6). In the PF joint, Mode 1 described variation in ML translation (Figure 4.5), which was linked to differences in the anterior aspects of the condylar geometry. PC scores for Mode 1 were strongly correlated to anatomic size measurements, including femoral epicondylar width (correlation $r = 0.91$) (Table 4.2).

Mode 2 described anatomical shape changes in the bone and cartilage, alta-baja (SI) alignment of the patella relative to the femur and PF kinematic changes in AP and SI

translation and IE rotation (Figure 4.3 and Figure 4.5). Illustrating alta-baja alignment of the patella, PC scores for Mode 2 were correlated to the Insall-Salvati index ($r = -0.61$, Table 4.2). The alta patella for Mode 2- had consistently larger AP and SI kinematics than the baja patella of Mode 2+, which affects the moment arm of the quadriceps. Further, the Mode 2- geometry with the alta patella had a shallower trochlear angle of 2.5° and exhibited internal patellar rotation during early flexion, compared to the baja patella in Mode 2+ with a steeper trochlear angle of 4.9° and external patellar rotation during flexion (Figure 4.5). Both models (Mode 2+ and 2-) realized a similar IE position at roughly 25° flexion when the patella engaged the trochlear groove. Differences in cartilage coverage on the bone were also noted in Mode 2 (Merchant view of Figure 4.3).

Mode 3 accounted for further anatomic shape changes in the femur and patella, and patellar alignment, including some alta-baja variability ($r = 0.54$) and initial PF IE and VV position. Differences were observed in the anterior-lateral aspect of the femur and trochlear groove; correlations between the antero-inferior femoral sulcus angle, measured in a 45° merchant view, and PC score for Mode 3 were -0.52 . The prominence of the anterior-lateral facet influenced both the initial PF IE (Figure 4.5) and VV (Figure B.2) alignment, although motions through the flexion cycle were similar (Figure 4.5). Mode 3 also resulted in the largest differences in the AP location of the lateral contact point (Figure 4.6) and ROM for TF IE rotation with 8.8° and 11.5° for Mode 3+ and 3-, respectively (Figure 4.4, Figure B.1). While not significantly correlated ($r < 0.5$), Mode 3 described differences in the distal sulcus angle of 7° between the +/- models, versus 3° and 4° in Modes 1 and 2, respectively.

Using data for the specimens in the training set, significant correlations were identified between 2D anatomical measurements and kinematics (Table 4.3, Figure B.3). The size measures, largely captured in Mode 1, were strongly correlated to many of the initial alignment DOF, particularly SI, AP and ML translation. A greater distal sulcus angle corresponded to greater tibial IE ROM through the flexion cycle ($r = 0.83$), while a greater distal condylar angle was correlated to a more valgus TF VV alignment ($r = 0.73$). As described in Modes 2 and 3, the Insall-Salvati ratio was correlated to initial PF FE ($r = -0.54$), SI ($r = 0.46$) and AP ($r = 0.50$) alignment. Bisect offset, a measure of patellar tracking, increased with more laterally-aligned PF joints ($r = 0.67$). Further, strong correlations were identified between TF and PF kinematics through the cycle, specifically between PF FE and TF FE, between PF VV and TF VV, and between PF ML and TF IE (Table B.2).

Results of the LOO evaluation characterized the predictive ability of the model with errors computed between the actual and model-predicted geometry and lowest point locations for the left-out knee. The absolute geometric error averaged across all nodes and for all specimens was 1.90 mm with a standard deviation of 0.39 mm. Differences between predicted and actual femoral lowest point were typically smaller in the medial compartment than the lateral and smaller in the ML direction compared to the AP direction (Figure 4.6, Table 4.4). Averaged over the flexion range and for all specimens, the mean absolute errors were 2.11 mm and 2.87 mm for the ML and AP directions on the medial condyle and 2.22 mm and 4.53 mm on the lateral condyle, respectively.

4.5. Discussion

The data-driven statistical modeling approach developed in this study demonstrated the ability to capture the role of complex anatomic and kinematic interactions and present them in a way that provides design and surgical insights. Relationships described between anatomy, initial alignment, and TF and PF motions through a squat cycle confirmed findings from several other studies, with the current approach enabling a more holistic consideration of the interactions. The benefits of the PCA-based approach are as follows:

- the PC modes describing the relationships between anatomy and kinematics are elucidate from the data without requiring *a priori* identification of the inputs and output measures to compare,
- evaluations are performed with the full articular geometry rather than a limited set of linear measures, and
- the resulting model enables predictions of kinematics for a new subject's geometry.

Traditionally, studies have identified sets of measurements and investigated relationships with correlations between measures of interest. For instance, Harbaugh et al. focused on lateral trochlear inclination angle (LTI) and patellar height, and reported a correlation between LTI and medial patellar tracking in their healthy control group ($r = 0.35$) (Harbaugh et al., 2010). Investigating the patellar anatomy of 907 subjects, Stefanik et al. reported the highest correlation between bisect offset and LTI ($r = -0.38$) (Stefanik et al., 2013). Further, Powers et al. reported correlations between bisect offset

and sulcus angle ($r = 0.74$) (Powers et al., 2000). The approach taken in the current study can be used to report similar correlations to these prior studies; for example, this data elucidated links between bisect offset and LTI ($r = -0.62$), between LTI and PF ML alignment ($r = -0.46$), between bisect offset and PF ML alignment ($r=0.67$), and between bisect offset and sulcus angle ($r=0.50$). However, the PCA-based approach implemented in the current work utilizes three-dimensional representations of the bones and cartilage, which enabled a more comprehensive analysis, including the potential to discover unanticipated links between anatomy and kinematics and the ability to investigate inter-relationships between measurements when interpreting findings, which may not be possible with the traditional approach. This approach does not require a priori knowledge of factors which are anticipated to be linked; instead, the entire shape and kinematic database is interrogated and relationships within that dataset emerge within each of the modes of variation. This extended beyond correlation of a single shape metric with a single kinematic metric to a more holistic interpretation of the data and the relationships within. For example, Mode 2 showed a relationship between an alta patella with shallow trochlear angle and internal patellar rotation.

The first 6 PC modes of variation were investigated to describe associations between changes in anatomy and kinematics. Emphasis was placed on the early modes which captured the largest amount of variance in the data. Further, a parallel analysis, which involved randomizing the variables within each observation and performing PCA on this new dataset in an effort to quantify the inherent noise in the data (Horn, 1965), found the first 6 modes were significant.

Described by Mode 1 with the most variation explained, changes in the sagittal femoral condyle geometry or J-curve were directly linked to the AP and IE kinematics and, ultimately, the location of the lowest point. The finding that more gradual radius changes through the flexion facet of Mode 1- led to reduced posterior tibial translation (or anterior femoral translation) (Figure 4.4 and Figure 4.6) agreed with Clary et al., which observed that an increasing "braking" radius results in less anterior motion and more rollback of the femur with respect to the tibia (Clary et al., 2013). Early flexion differences in the lowest point representation were affected by shape of the distal region of the femoral condyles with Mode 1- having a more flattened profile. Coupled with a steeper slope for tibial IE rotation, the lowest-point behavior near extension was characteristic of the screw-home mechanism (Piazza et al., 2000). The lowest point location provides a surrogate measure of contact and enables comparisons to prior fluoroscopic studies (Banks et al., 2003; Dennis et al., 2005). Alternatively, a contact or patch-based analysis of the kinematics could provide additional information, but was not considered in the current study.

Further, differences in TF IE rotation during the cycle were described in Modes 3, both in ROM (Figure 4.4 and Figure B.1) and the location of the femoral lowest point (Figure 4.6). Hoshino et al. noted the importance of distal femur morphology, particularly a correlation between condylar twist angle and internal tibial rotation (Hoshino et al., 2012). Changes in the morphology of the distal femur were also described in Mode 3 with differences reported in distal sulcus angle. According to Freeman et al., the inner facets of the condyles and tibial eminence interact to guide tibial

rotation (Freeman et al., 2005). Lastly, the more general correlation between tibial IE rotation and patellar ML translation is consistent with Sheehan et al. and underscores the shape-driven interactions between TF and PF joints (Sheehan et al., 2009).

PF kinematics were dependent on the anatomy of the patella and trochlear groove, and initial patellar alignment. A deeper trochlear groove or smaller sulcus angle led to more PF external rotation (Mode 2), while the anatomy of the anterior-lateral facet and trochlear groove influenced the initial PF IE alignment. Regarding patellar alta-baja, the Insall-Salvati index, PC score for Mode 2 and PF AP alignment all shared strong correlations (Table 4.2 and Table 4.3). Fitzpatrick et al. showed that quadriceps efficiency during a deep knee bend was affected by patellar resection thickness (Fitzpatrick et al., 2013), highlighting that the AP position of the patella serves as an effective moment arm. Accordingly, the current model may be useful in developing subject-specific representations for musculoskeletal simulations considering shape and alignment variability in the population.

Numerous studies have used shape of the femur, patella and relative alignment as measures to differentiate healthy normal and pathologic groups. This study confirmed the importance of alta-baja, bisect offset and sulcus angle in PF mechanics, and notes their established links to PF pain and maltracking (Pal et al., 2013; Harbaugh et al., 2010). This study also demonstrated the ability to efficiently measure these important parameters within the SSM and evaluate them with respect to dynamic motions, rather than static poses used in prior MR based studies. Both of these considerations are

important in enabling evaluations of larger-scale populations under clinically relevant conditions.

As subject-specific measurement of kinematics is time consuming and expensive, it is rare to have a dataset of 20 natural knees for the same activity. Many studies have presented kinematics for datasets with smaller numbers of subjects. However, the size of the dataset remains relatively small when compared to the overall population. The all-male training set is not representative of the overall population and is a limitation of the study; however, the group does represent a subset of the potential total knee replacement population. A further limitation is that the kinematic data were measured from cadaveric specimens in a simulator. The applied loading condition was identical for all specimens and not scaled with size or body weight, which will influence the kinematics. The shape-function approach could be similarly implemented using *in vivo* data from biplane fluoroscopy, which potentially allows for consideration of larger numbers of subjects and a greater variety of activities. As the data required to represent the subject's shape is part of the workflow, implementation can be performed with minimal additional processing. Interestingly, SSM has recently been used to represent the subject's geometry using an optimization to the fluoroscopy data alone, alleviating the need for additional imaging and segmentation (Baka et al., 2012).

This study did not directly investigate the role of soft tissue structures, which are known to provide constraint and impact knee mechanics. The cadaveric simulator data notably captured intersubject variability in anatomy, alignment and soft tissue constraint, and thereby considered factors not included in Fitzpatrick et al., which used kinematics

derived from finite element analyses with a constant soft tissue representation (Fitzpatrick et al., 2011).

The predictive capability of the SSM was evaluated using the LOO test; results demonstrated the ability of the model to accurately recreate the shape and kinematics of the left-out specimen. The errors in shape representation were comparable to those reported in Rao et al. and other SSM models (Rao et al., 2013). Errors in the lowest point predictions were dependent on the condyle and DOF, but less than 3 mm on average for all DOF. The ability to represent new subjects accurately provides confidence in using the approach in larger population studies which require the generation of virtual instances.

Insight into relationships between knee anatomy and kinematics has broad reaching impact in biomechanics. Relationships for the healthy normal dataset can address current areas of interest in knee mechanics and the design of total knee replacement implants, particularly regarding the impact of shape of the condylar geometry or j-curve and identifying anatomical features that drive motion (e.g. rotation or rollback). Additionally, insight into the kinematics associated with patients with certain characteristics (e.g. patella alta or a narrow trochlear groove) may lead to altered surgical decision-making related to implant selection, sizing and placement to avoid overloading regions of bone, crepitus and other complications (Dennis et al., 2011; Fitzpatrick et al., 2013). The approach can be extended to further investigate differences between healthy normal and pathologic groups, especially when shape and alignment are contributing factors, as in patellar maltracking, PF pain and varus/valgus deformities.

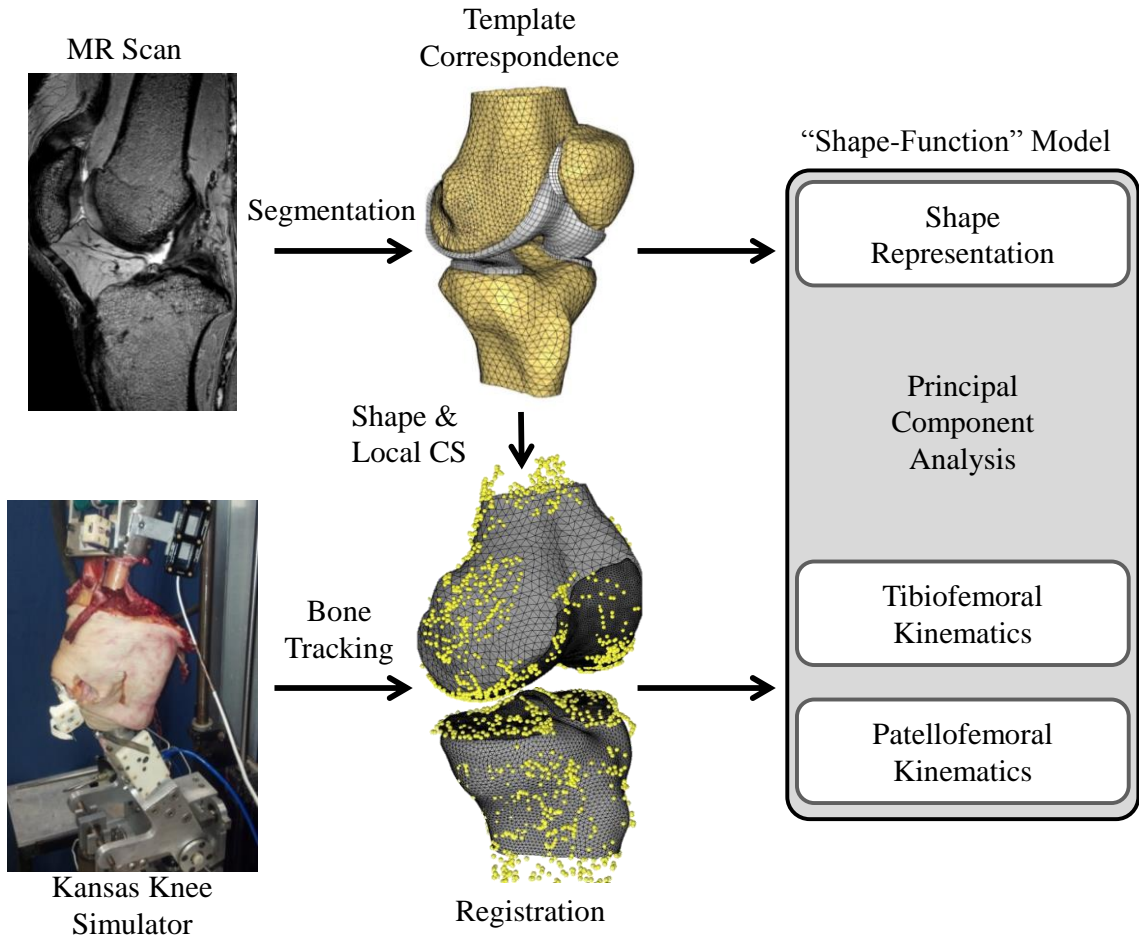


Figure 4.1 Development of a statistical shape and function model. The shape representation was derived from image data by segmenting and establishing correspondence to a template mesh, and tibiofemoral and patellofemoral kinematics were obtained from cadaveric testing and registration of the anatomy and local coordinate systems (CS) to experimentally probed points.

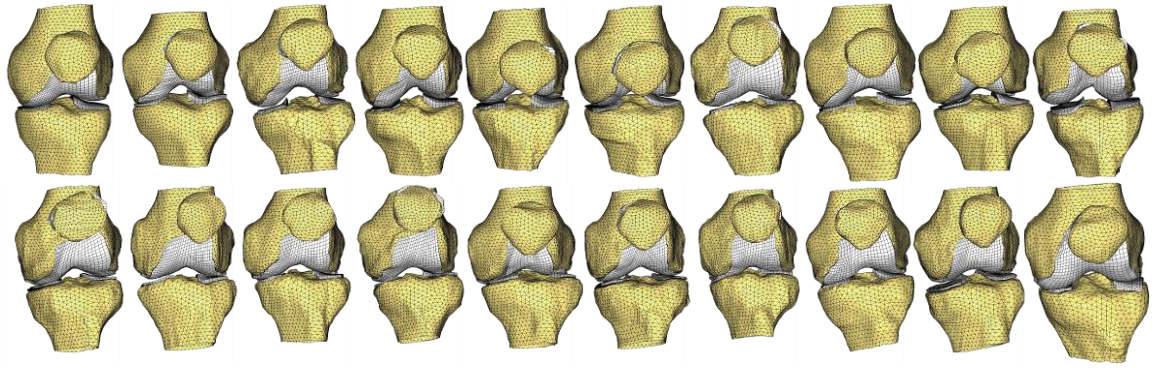


Figure 4.2 Training set of 20 specimens used to create the statistical shape-kinematics model. Specimens are represented with the template mesh in the initial kinematic position.

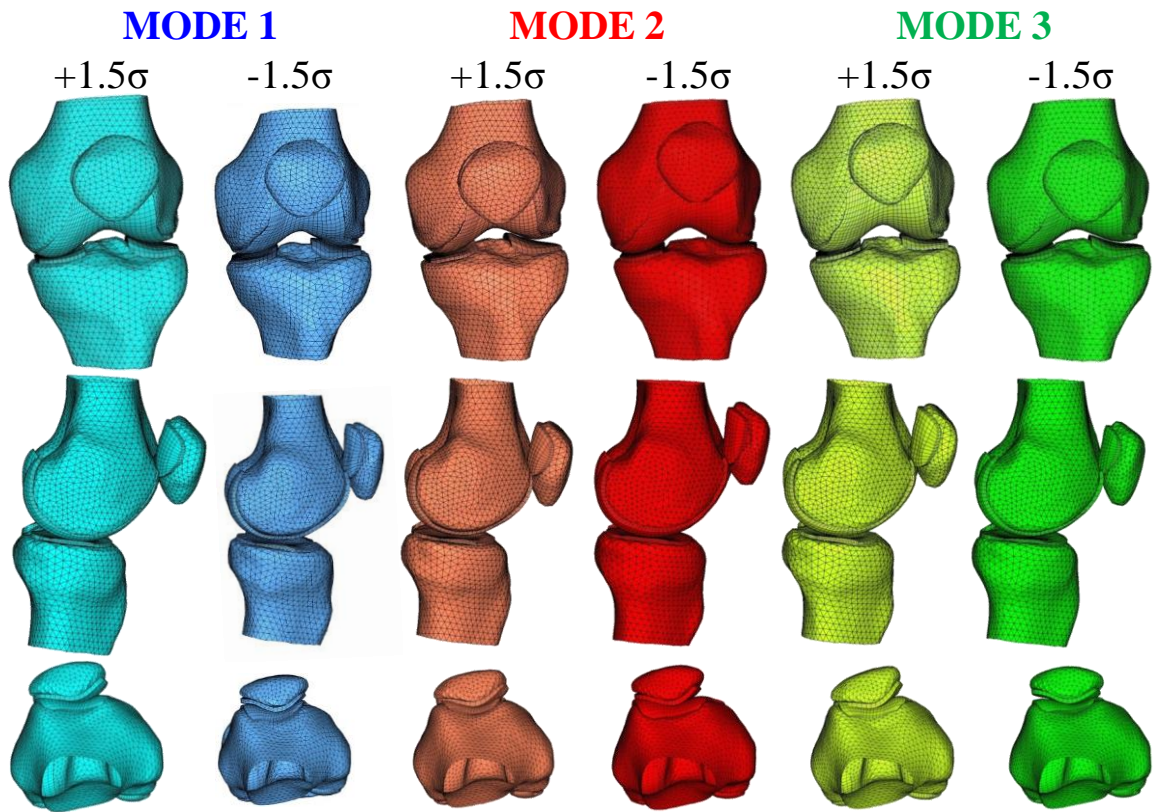


Figure 4.3 Representations of bone and cartilage for the first three principal component modes. Knees are shown at +/- 1.5 standard deviations. Coronal and sagittal views at initial alignment with merchant view at 45° TF flexion.

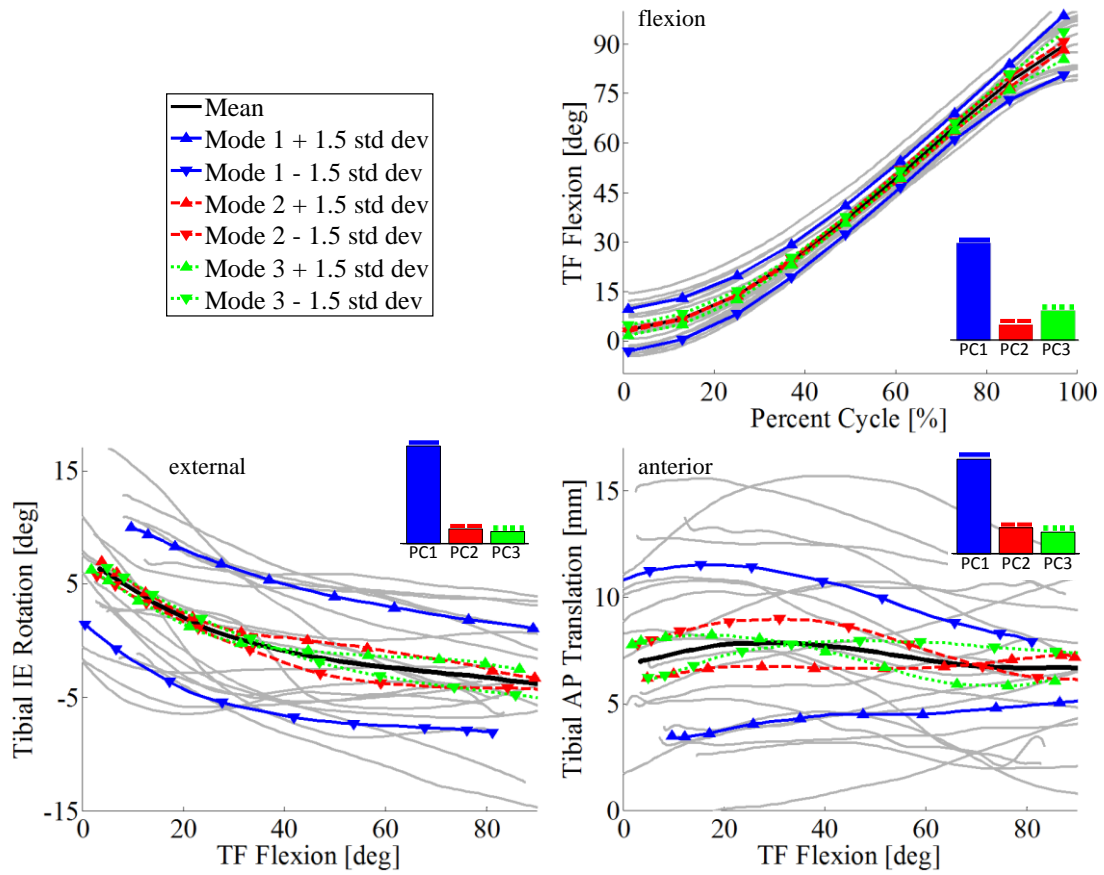


Figure 4.4 Tibiofemoral kinematics for the first 3 principal component modes and all specimens (gray lines). Clockwise from top: Tibial flexion-extension, anterior-posterior (AP) translation and internal-external (IE) rotation. Inset bar charts show relative contribution of each mode.

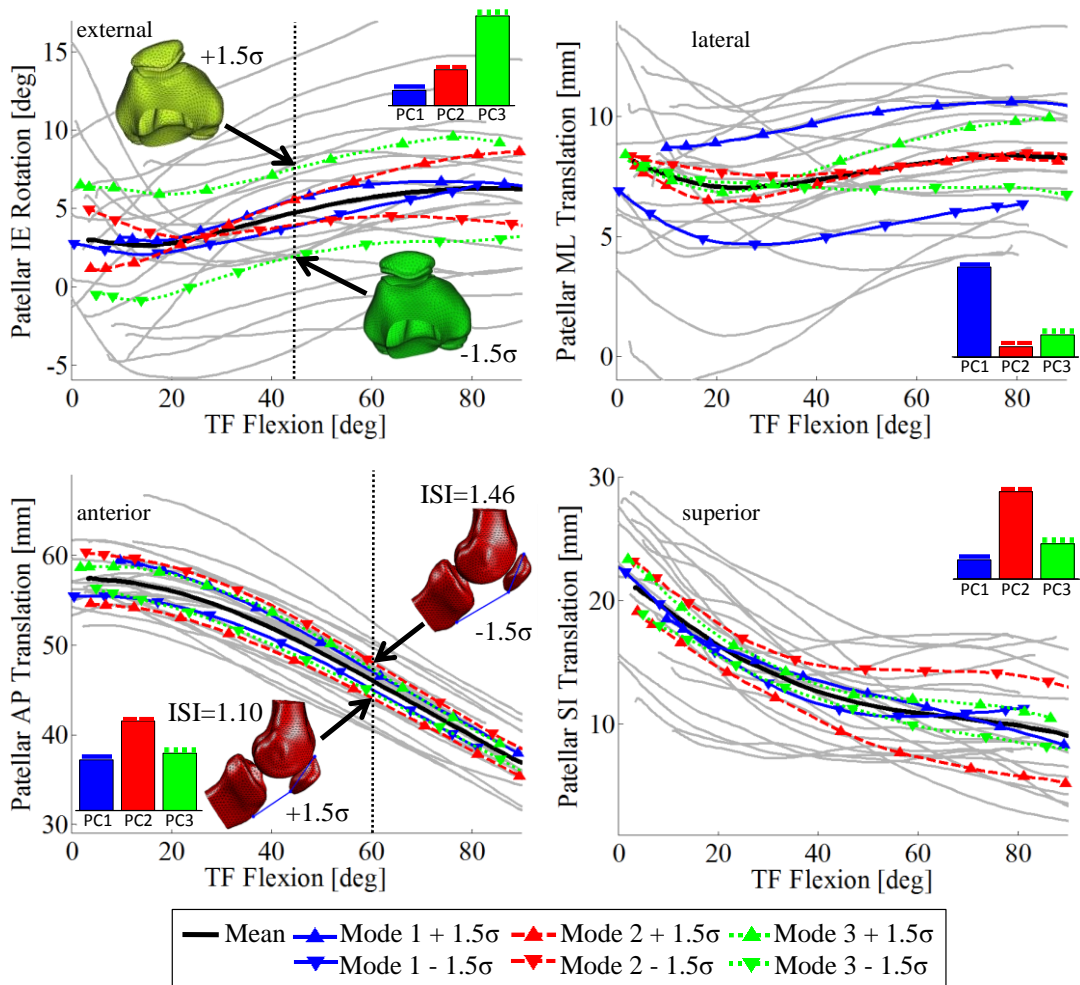


Figure 4.5 Patellofemoral kinematics for the first 3 principal component modes and all specimens (gray lines). Clockwise from top-left: Patellar internal-external (IE) rotation, medial-lateral (ML) translation, superior-inferior (SI) translation and anterior-poster (AP) translation. Inset bar charts show relative contribution of each mode. ISI = Insall-Salvati Index.

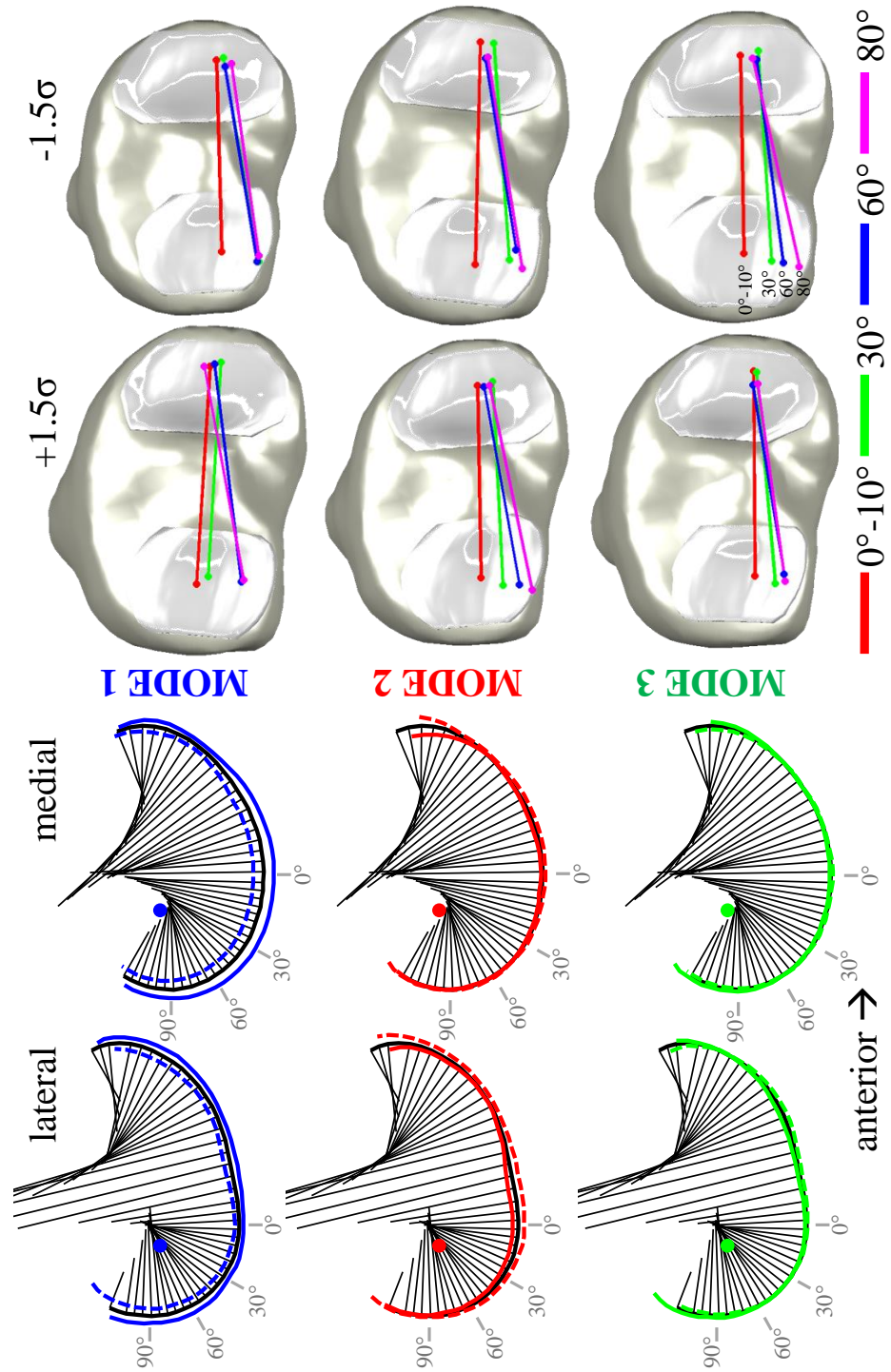


Figure 4.6 Sagittal condylar geometry (with radius of curvature lines) for the mean and first three modes (left). Femoral lowest point representation of the TF contact points for the first three modes at +/- 1.5 standard deviations (right).

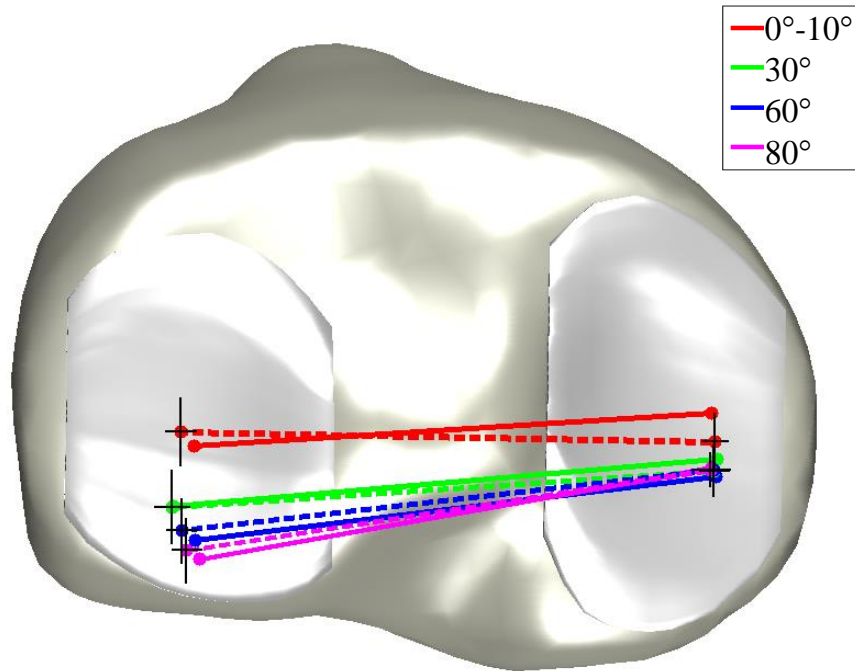


Figure 4.7 Comparison of actual (solid) and predicted (dashed) lowest contact point for a leave-one-out evaluation with varying flexion. Predictions were made with each member of the training set left out of the analysis. Error bars shown for anterior-posterior (AP) and medial-lateral (ML) degrees of freedom on each condyle. Full extension results reported as 0-10° flexion as not all specimens achieved 0°.

Table 4.1 Descriptive statistics and anatomical measures for the training set.

Anatomic Measure	Mean	Standard Deviation	Min.	Max.
Age [yr]	64	10.8	44	80
Weight [kg]	78	16.2	61	127
Body Mass Index [BMI]	25	5.2	19	41
Epicondylar Width [mm]	87.4	4.0	81.0	98.3
Femur AP Width [mm]	66.4	2.8	62.1	75.2
Tibia ML Width [mm]	80.3	3.5	73.8	89.4
Patella AP Thickness [mm]	19.0	2.3	14.9	22.8
Patella Angle [°]	146.5	6.4	136.2	155.7
Insall-Salvati Index	1.2	0.2	0.8	1.5
Trochlear Angle [°]	4.2	2.3	0.3	8.7
Anterior Sulcus Angle [°]	144.3	8.8	131.6	171.5
Medial Trochlear Inclination [°]	163.1	6.0	152.5	179.8
Lateral Trochlear Inclination [°]	18.8	3.7	8.4	24.9
Antero-inferior Sulcus Angle [°]	72.2	13.8	56.3	118.1
Distal Sulcus Angle [°]	132.4	6.2	122.4	145.0
Distal Condylar Angle [°]	6.7	2.0	3.6	10.9
Bisect Offset [%]	60.1	6.7	50.2	76.1

Table 4.2 Pearson’s correlation coefficients between the first six principal components and anatomical and kinematic measures. Initial alignment correlations were calculated at approximately 10 degrees TF flexion. Range-of-motion (ROM) was defined as the difference between the minimum and maximum values in a kinematic measure. Correlations are presented as absolute values. Anatomical measures with no significant correlations were omitted. White cells indicate no correlation.

		0.4 to 0.6	0.6 to 0.8	0.8 to 1.0	PC 1	PC 2	PC 3	PC 4	PC 5	PC 6
	Epicondylar Width				0.91					
	Femur AP Width				0.82	0.45				
	Tibia ML Width				0.82	0.40				
	Patella AP Width				0.59					0.46
	Insall-Salvati Index					0.61	0.54			
	Trochlear Angle					0.44			0.44	
	Lateral Troch. Incl.						0.46			
	Antero-inferior Sulcus Angle						0.52			
	Bisect Offset							0.52		
	Distal Sulcus Angle									0.40
TF	Alignment				0.70					
FE	ROM				0.42					
TF	Alignment							0.48	0.44	
VV	ROM				0.55					
TF	Alignment				0.63					
IE	ROM									0.51
TF	Alignment									
ML	ROM								0.77	
TF	Alignment							0.43		
AP	ROM									0.55
TF	Alignment				0.71				0.40	
SI	ROM				0.47			0.55		
PF	Alignment				0.55				0.47	
FE	ROM				0.51					
PF	Alignment						0.80			
VV	ROM				0.67					
PF	Alignment						0.44			
IE	ROM					0.56				
PF	Alignment							0.64		
ML	ROM									0.45
PF	Alignment					0.62				
AP	ROM				0.61			0.42		
PF	Alignment								0.58	
SI	ROM									

Table 4.3 Pearson’s correlation coefficients between anatomical and kinematic measures. Initial alignment correlations were calculated at 10 degrees TF flexion. Range-of-motion (ROM) was defined as the difference between the minimum and maximum values in a kinematic measure. Correlations are presented as absolute values. Anatomical measures with no significant correlations were omitted. White cells indicate no correlation.

		Epicondylar Width	Femur AP Width	Tibia ML Width	Patella AP Width	Insall-Salvati Index	Trochlear Angle	Anterior Sulcus Angle	Lateral Troch. Incl.	Antero-inferior Sulcus Angle	Distal Sulcus Angle	Distal Condylar Angle	Bisect Offset
		0.4 to 0.6											
		0.6 to 0.8											
		0.8 to 1.0											
TF	Alignment	0.56	0.77	0.54	0.51								
FE	ROM	0.51						0.50	0.62				
TF	Alignment											0.73	0.43
VV	ROM	0.53	0.53										
TF	Alignment	0.60		0.58								0.40	
IE	ROM										0.83		
TF	Alignment	0.41									0.49		
ML	ROM												
TF	Alignment	0.50	0.46										
AP	ROM												
TF	Alignment	0.69	0.64	0.62						0.40			
SI	ROM												
PF	Alignment	0.42		0.41		0.46	0.42	0.47					
FE	ROM	0.44	0.53			0.41							
PF	Alignment								0.41	0.42			
VV	ROM	0.65	0.64	0.67									
PF	Alignment												
IE	ROM		0.43								0.46		
PF	Alignment				0.51			0.44	0.46				0.67
ML	ROM					0.45							
PF	Alignment		0.68			0.41					0.46		
AP	ROM	0.53	0.57	0.48	0.61						0.57		
PF	Alignment					0.43							
SI	ROM											0.43	

Table 4.4 Mean absolute error between experimental and predicted lowest point results averaged across all specimens. All values are in millimeters.

Flexion Angle (°)	Medial				Lateral			
	ML		AP		ML		AP	
	μ	σ	μ	σ	μ	σ	μ	σ
0	1.98	1.34	3.76	2.81	2.20	1.56	4.53	3.35
30	1.99	1.46	2.77	2.56	2.49	1.76	4.03	3.69
60	1.83	1.56	2.56	1.75	2.46	1.52	4.49	3.23
80	2.65	1.91	2.39	1.69	1.74	1.51	5.06	3.20
Average	2.11	1.57	2.87	2.20	2.22	1.59	4.53	3.37

CHAPTER 5. MEASURES-DRIVEN PREDICTION OF PATELLOFEMORAL JOINT KINEMATICS

5.1. Abstract

Patellofemoral (PF) complications in the natural knee, including subluxation and dislocation, account for at least 25% of reported knee problems in active individuals. Clinical assessments and rehabilitation protocols rely upon a practical understanding of the anatomical factors influencing joint kinematics. The purpose of this study was to create a statistical shape-function model to isolate clinically relevant morphological factors influencing joint function and assess the predictive capability of linear measures on kinematics. Fifteen clinically obtainable 2D linear measures of shape and alignment of the PF joint were taken on twenty-four 3D finite element (FE) models. A statistical measures-only model was created using principal component analysis (PCA) to characterize variability in the training set. 6 degree-of-freedom (DOF) kinematics of the PF joint were adopted from a previous study and combined with the measures-only principal component (PC) scores to create a new statistical model. The first three PC modes primarily described scaling, trochlear groove geometry, and patellar mediolateral (ML) alignment, respectively. Linear measures such as trochlear groove angle in the coronal plane and intercondylar notch width at the distal aspect were correlated with PF ML range-of-motion. Mean RMS error across all knees between the FE-predicted and

statistical model-predicted kinematics were less than 3.0 degrees and 2.6 mm based on 5 PCs, which described 83.6% of the total variability in the statistical model, were used. The statistical modeling approach elucidated new relationships between clinically accessible measures and joint motion and the prediction of motion by a combination of linear measures suggests potential for developing clearer causal relationships.

5.2. Introduction

Patellofemoral (PF) complications in the natural knee, including subluxation and dislocation, account for at least 25% of reported knee problems in active individuals (Boling et al., 2010). PF joint function is influenced by a number of factors including the surrounding musculature, joint ligament laxity, and articular surface geometry (Jafari et al., 2008). Evaluation and diagnosis of PF joint complications are informed by an understanding of which factors contribute to a particular conditions or characteristics of motion.

Clinical measures such as patella alta, tilt, and the femur trochlear groove geometry have been correlated with PF joint function and pain (Pal et al., 2013; Stefanik et al., 2013; Harbaugh et al., 2010; Freedman et al., 2013). Pal et al., (2013) assessed the effects of patella alta-baja, a measure of patellar superior-inferior (SI) alignment in the sagittal plane, on PF pain syndrome; subjects with patella alta were more likely to experience pain during weightbearing (Pal et al., 2013). Harbaugh et al. (2010) evaluated femur trochlear shape measures in groups of pain and pain-free subjects, finding relationships between shape and tracking in all groups particularly for lateral trochlear inclination (LTI) and patellar height (Harbaugh et al., 2010). 2D linear measures of static

alignment from magnetic resonance (MR) images could only partially predict dynamic 6 degree-of-freedom (DOF) PF joint kinematics (Freedman et al., 2013), which suggests that contributions from only alignment may be confounded by the challenges of working with experimental kinematics.

Computer models of the PF joint have attempted to evaluate joint function by individually perturbing specific inputs in a design-of-experiments (DOE) analysis. Jafari et al. (2008) controlled joint characteristics such as femoral anterior sulcus angle (ASA), quadriceps line-of-action, and medial retinaculum laxity to study their effects on patellar subluxation and dislocation (Jafari et al., 2008). A mathematical model solved static equilibrium equations describing PF joint geometry and loads to assess geometric and ligamentous constraint effects on alignment. Each characteristic individually contributed to patellar maltracking; however, a combination of the characteristics resulted in the most severe lateral shift. More recently, a DOE analysis was combined with a validated finite-element (FE) model of the PF joint to evaluate factors associated with dislocation (Fitzpatrick et al., 2016). The study also reported the largest maltracking issues with a combination of factors and described sulcus angle as the most impactful factor.

Statistical models provide an alternative approach to evaluations of joint mechanics by characterizing and quantifying relationships between natural or implanted joint geometry and function. FE-based analyses have been combined with statistical models of bone shape and material properties to evaluate performance of the implanted tibia as well as the natural and implanted femoral head (Galloway et al., 2013; Bryan et al., 2009; Bryan et al., 2012), and articular surface geometry to evaluate PF kinematics

(Fitzpatrick et al., 2011). Studies have also combined 3D bone and cartilage models with experimental kinematics using principal component analysis (PCA) to quantify relationships in the natural knee (Smoger et al., 2015). Fitzpatrick et al. (2011) created a statistical shape and function model with FE predicted PF joint mechanics to study relationships between 3D joint geometry and function. FE modeling is particularly useful for its ability to efficiently assess whole joint variability in a controlled environment. A larger SSM consisting of the bones and cartilage for both the PF and TF joints was recently developed; elucidating similar relationships between shape and function as well as inter-joint relationships such as the influence of tibial internal rotation and patellar medial translation (Smoger et al., 2015). The use of statistical modeling to characterize and predict whole joint shape-function relationships supports the hypothesis that an array of clinical measures may equally inform these relationships, providing a more direct cause-effect relationship between shape and kinematics.

Thus, the purpose of this study was to build a statistical model of the PF joint to identify key shape measures influencing joint motion and assess their predictive capability. The statistical model included clinically relevant 2D linear measures and 6-DOF PF kinematics predicted by a validated dynamic FE simulation of the PF joint in Fitzpatrick et al. (2011). Measures were taken directly from the 3D FE models, thus measurements were not constrained to a single slice as is the case in scan-based approaches. The measures represent a comprehensive set of clinically obtainable dimensions from common knee radiographs. The FE simulation isolated articular surface shape variability from other factors influencing PF joint function; thus, the advantage was

a more explicit relationship between linear measures and function. 2D linear measures serve as simpler descriptors of joint morphology over whole joint representations; however, they are significantly easier to measure and thus their impact on joint function is useful for establishing norms and understanding natural knee joint complications.

5.3. Methods

Twenty-four 3D finite element (FE) models of healthy, subject-specific knee joints were adopted from a previous study (Fitzpatrick et al., 2011). The models had been developed from segmented magnetic resonance (MR) scans and consistent loading conditions and musculature were applied to each subject-specific bone and cartilage geometries. Joint function was described by 432 6-DOF PF kinematics (72 variables per DOF) also adopted from the aforementioned study. Kinematics were reported with respect to the femur using a three-cylindrical open-chain description of motion (Grood and Suntay, 1983). For the current study, an automated measurement algorithm extracted fifteen linear anatomical measurements from the 3D geometry (Table 5.1, Figure 5.1). The algorithm was developed in Matlab (Mathworks, Natick, MA, USA) and included calculations for single bone and joint alignment measurements. Measurements such as trochlear angle, sulcus width, and bisect offset are taken with respect to the posterior condylar line (PCL), which is a commonly used anatomical reference line (Stefanik et al., 2013; Harbaugh et al., 2010).

A statistical model of the fifteen measures was created by applying principal component analysis (PCA) to the training set measures. PCA calculates a new set of orthogonal bases, or PCs, to describe the linear measures. Components are ranked by the

amount of variance they describe and each subject is given a PC score that represents its measures in each component. The goal of the statistical model is to group like measures into a single PC. A subsequent statistical model combined the linear measure PC scores and FE-based kinematics to describe relationships between shape modes of variation and joint motion. Relationships between shape and function were elucidated by calculating Pearson's correlation coefficients between measures and characteristics of joint motion including range of motion (ROM), and alignment at various flexion angles throughout the cycle. Individual measures were correlated with a particular motion characteristic if both metrics varied significantly within a given PC mode of variation. Correlations above 0.5 were considered significant.

The predictive capability of the measure-kinematics model was assessed by a leave-one-out type of analysis. The number of measures included in the model was constrained to three and the leave-one-out evaluations of all possible combinations were performed. Three of the fifteen measures were selected to avoid overfitting model data and isolate the most influential measures. Each subject was successively left out of the training set and a new measure-kinematics statistical model was developed with the remaining subjects. The new model was then used to predict the left-out subject's kinematics given only their linear measures. A predictive PCA approach (Fitzpatrick et al. 2011) was employed wherein the predictors (measures) and predicted variables (kinematics) were separately correlated to the PC scores of the combined measure-kinematics model. These correlations described the strength of PCA to characterize the relationships between predictor and predicted variables. The linear relationship (slope)

between predictor and overall PC scores was used to modify the PC scores of a “new” subject. These modified PC scores were then projected from PC space back into their original coordinate system (degrees or millimeters). Accuracy was reported as the average across all knees of the RMS error between model-predicted and FE-based kinematics.

5.4. Results

The measure-only statistical model characterized relationships within the linear measures, describing 95% of the variability with the first 10 principal component modes of variation (Table 5.2). The first 3 modes of variation described 70.1% of the variability and were correlated to specific linear measures. Mode 1 primarily described scaling; the Pearson’s correlation coefficient between Mode 1 and femur cartilage ML width, R, was 0.95. Mode 1 was also the only mode to describe femur trochlear angle ($r = -0.66$). Mode 2 described several measures independent of scaling including femur anterior and distal sulcus angles ($r = -0.53$ & $r = 0.88$) as well as PF congruency at the same positions that sulcus angle measures were taken ($r = 0.57$ & $r = -0.64$). Mode 2 also described variability in the LTI ($r = 0.51$), a measure which was inversely proportional to patellar ridge medialization ($r = -0.54$). Ridge medialization was measured as the perpendicular distance from a sagittal plane at the centroid of patella to the middle of the ridge line. While not considered significant, Mode 2 was most highly correlated of any with Insall-Salvatti index ($r = -0.47$). Mode 3 described femur antero-inferior sulcus angle ($r = 0.63$) and bisect offset ($r = 0.65$).

The measure-kinematics model linked shape and kinematic metrics by trends in variability. Mode 1 was correlated with most kinematic measures likely due to the scaling factor whereas the next two modes described unique motion characteristics independent of size (Figure 5.2). Mode 2 described variability in patellar flexion-extension (FE), and SI alignment independent of scaling ($r = 0.83$ & $r = 0.76$). Mode 3 described variability in patellar mediolateral (ML) and internal-external (IE) alignment ($r = 0.53$ & $r = 0.62$, respectively). Mode 5 was correlated with PF ML ROM ($r = -0.50$) and mildly correlated with trochlear groove angle (TGA) ($r = 0.43$).

Relationships directly between linear measures and kinematics were also assessed. Descriptors of the trochlear groove geometry were correlated with PF ML ROM, particularly ASA ($r = 0.58$) and its medial and lateral components, MTI ($r = 0.55$) and LTI ($r = -0.50$). Two measures, LTI and intercondylar notch width at the distal aspect, were correlated to PF IE ROM ($r = 0.58$ and $r = -0.55$). In effect, as the intercondylar notch width grows, PF contact points move away towards the outer regions of the patellar facets, resulting in increased constraint of the patella. Trochlear groove angle (TGA) was consistently correlated to patellar ML alignment after 30 degrees TF flexion ($r = -0.6$) and trended toward significance with PF ML ROM ($r = -0.47$), which is notable considering the relationships between Mode 5 and both of these measures of shape and function.

The predictive capability of the measure-kinematics model was elucidated by the accuracy between model-predicted and FE-based kinematics. Overall, mean RMS differences across all knees were less than 3.0 degrees and 2.6 mm when 5 PCs

describing 83.6% of the total variability in the statistical model were used (Table 5.3, Figure 5.3). Separate sets of measures accurately predicted different kinematic DOF. PF flexion was predicted to within 3 degrees by the femur epicondylar width, AP width, and height of the patella (Table 5.3). PF IE rotation was the most challenging to predict at 2.6 degrees however the optimal measures included femur sulcus angle, medial trochlear inclination, and trochlear groove angle. PF ML translation was predicted to within 2.1 mm by the femur sulcus groove width, bisect offset, and trochlear groove angle. PF AP translation was predicted to within 1.3 mm by the distal sulcus angle, patellar ML width, and Insall-Salvati index. By comparison, the statistical model developed by Fitzpatrick et al. (2011) with the full articular geometry predicted kinematics with similar accuracy. A reconstruction test confirmed that when population-level variability was accounted for in the statistical model (by including that subject in the development of the model), the model predicted that subject's kinematics perfectly.

5.5. Discussion

Clinical measures are easily accessible and may provide causal information regarding how a joint functions under observed conditions. The purpose of this study was to quantify the ability of clinically obtainable measures to describe subject-specific FE-predicted PF joint kinematics. A statistical model of shape and alignment measures of the femur and patella quantified relationships between morphological features and grouped them by modes of variation. Measures of scaling were primarily described by the first mode of variation, which is a common trait of biological structure variability. Mode 2 described a significant amount of the trochlear groove variability, which

confirms existing studies that have reported the largest influences on PF kinematics from a combination of morphological changes (Stefanik et al., 2013; Nha et al., 2008). A notable inverse relationship between LTI and patellar ridge medialization was discovered; steeper and thus larger LTI angles in healthy individuals corresponded to a more centered patellar ridgeline, which likely keeps the patella from being forced medially by the groove. Femur trochlear angle in the axial plane has been described as a possible factor for patellar tracking (Stefanik et al., 2013). That measure was not found to influence kinematics in this study; however, trochlear angle was closely tied to measures of scaling, which may explain the variability in ML translation described by Mode 1 (Figure 5.2). The correlation between width of the intercondylar notch at the distal aspect and PF ML ROM is a new relationship that provides further insight into deep-flexion patellar stability.

The predictive capability of linear measures may directly impact clinicians as these measures are commonly retrieved from most imaging modalities (i.e. CT, MR, X-ray). The current study differs from the approach taken by Freedman et al. (2013); their predictions were based solely on alignment measures whereas the current study considered morphological measures in addition to several measures of alignment. Furthermore, the combined optimization and statistical modeling approach allowed for a search of the entire design space to identify the 3 key measures that influenced individual kinematics and ultimately increased accuracy over using all 15 measures. The increase in accuracy can be explained by eliminating measures that were not strongly correlated to a particular kinematic DOF and thereby reducing noise in the predictor variables. Key

predictive measures such as patellar height for PF SI and angular measurements of the trochlear groove for PF IE support the findings of Harbaugh et al. (2010) who reported that taller patellae tracked higher in the trochlear groove and an increase in LTI corresponded to internal patellar rotation (Harbaugh et al., 2010).

By including only the first several PC modes of variation from the measures-only statistical model to make the kinematic predictions, a reduced set of interrelated measure combinations was able to accurately reproduce subject-specific kinematics. By comparison, the statistical shape-function model developed by Fitzpatrick et al. (2011) reported mean errors of less than 3 degrees and 2.5 mm. This study has shown that a drastically reduced number of variables, particularly ones that are feasibly measured in a clinical setting, can achieve comparable levels of accuracy.

Factors other than shape are known to influence joint mechanics. The effects of tibiofemoral kinematics on patellar tracking have been well documented (Sheehan et al., 2009; Smoger et al., 2015; Mizuno et al., 2001). Specifically, tibial IE rotation is known to influence patellar ML translation (Sheehan et al., 2009; Smoger et al., 2015) and an increased Q-angle shifts the patella laterally with internal rotation (Mizuno et al., 2001). Musculature also plays a significant role; Shalhoub et al. (2014) reported PF kinematic variability due to changes in quadriceps loading. Quadriceps loading, however, was a controlled factor in the FE model from which the current study's kinematics were adopted. Furthermore, the geometries considered in this study were healthy, which limits conclusions for pathologic knees as their shape is often significantly different.

Overall, the approach highlighted several key benefits: combinations of interrelated measures were grouped into separate shape parameters without a priori knowledge of relationships, relationships between kinematics and both individual measures or groups of measures were quantified, and the relationships were strong enough to use in predictive studies to evaluate new geometries.

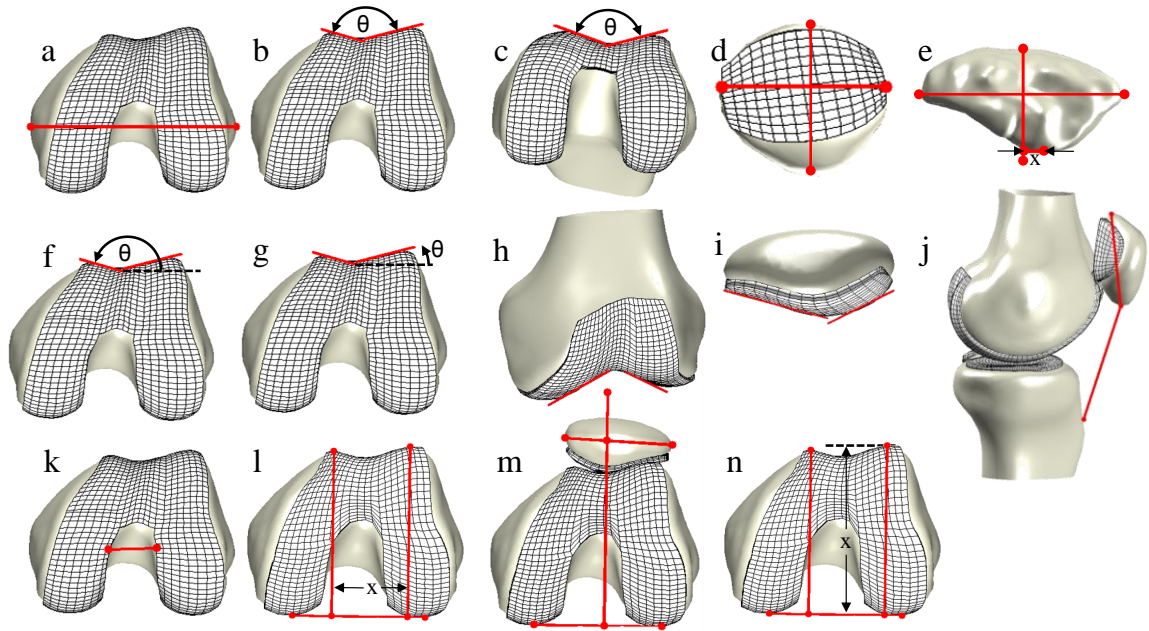


Figure 5.1 Illustrations of the automatically extracted linear measures. Measures include femur epicondylar width (a), femur anterior sulcus angle (b), femur antero-inferior sulcus angle (c), patellar cartilage width and height (d), femur cartilage width along the epicondylar axis (e), medial trochlear inclination (f), lateral trochlear inclination (g), distal sulcus angle (h), patellar angle (i), Insall-Salvatti Index (j), intercondylar notch width (k), femur sulcus width along the posterior condylar line (PCL) (l), bisect offset (m), and femur AP width (n). The angle formed by the PCL and the line connecting both anterior condylar points on the femur (image n) describes the trochlear angle (axial plane).

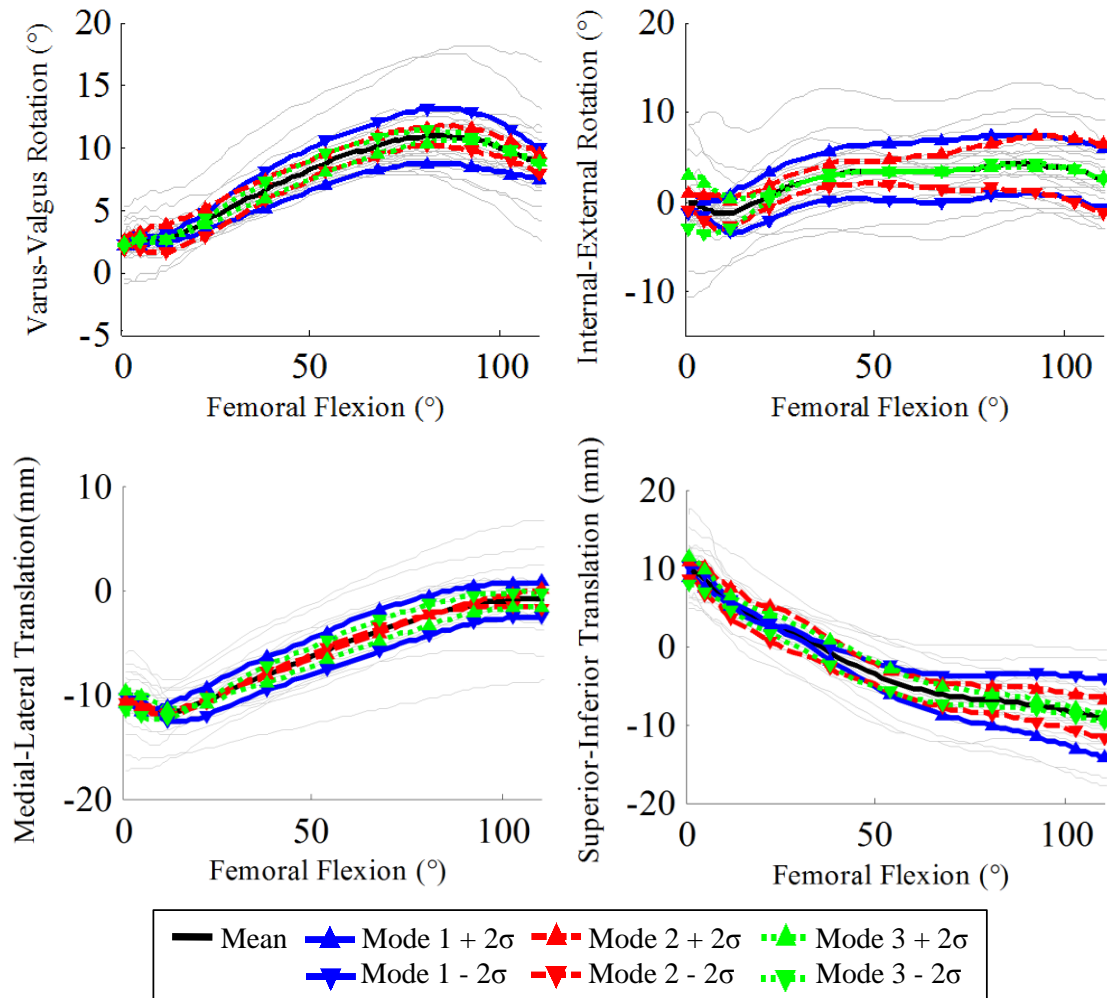


Figure 5.2 Patellofemoral kinematics for the first three principal component modes and all subjects (gray lines). Patellar varus-valgus (VV) and internal-external (IE) rotation (top), medial-lateral (ML) and superior-inferior (SI) translation (bottom).

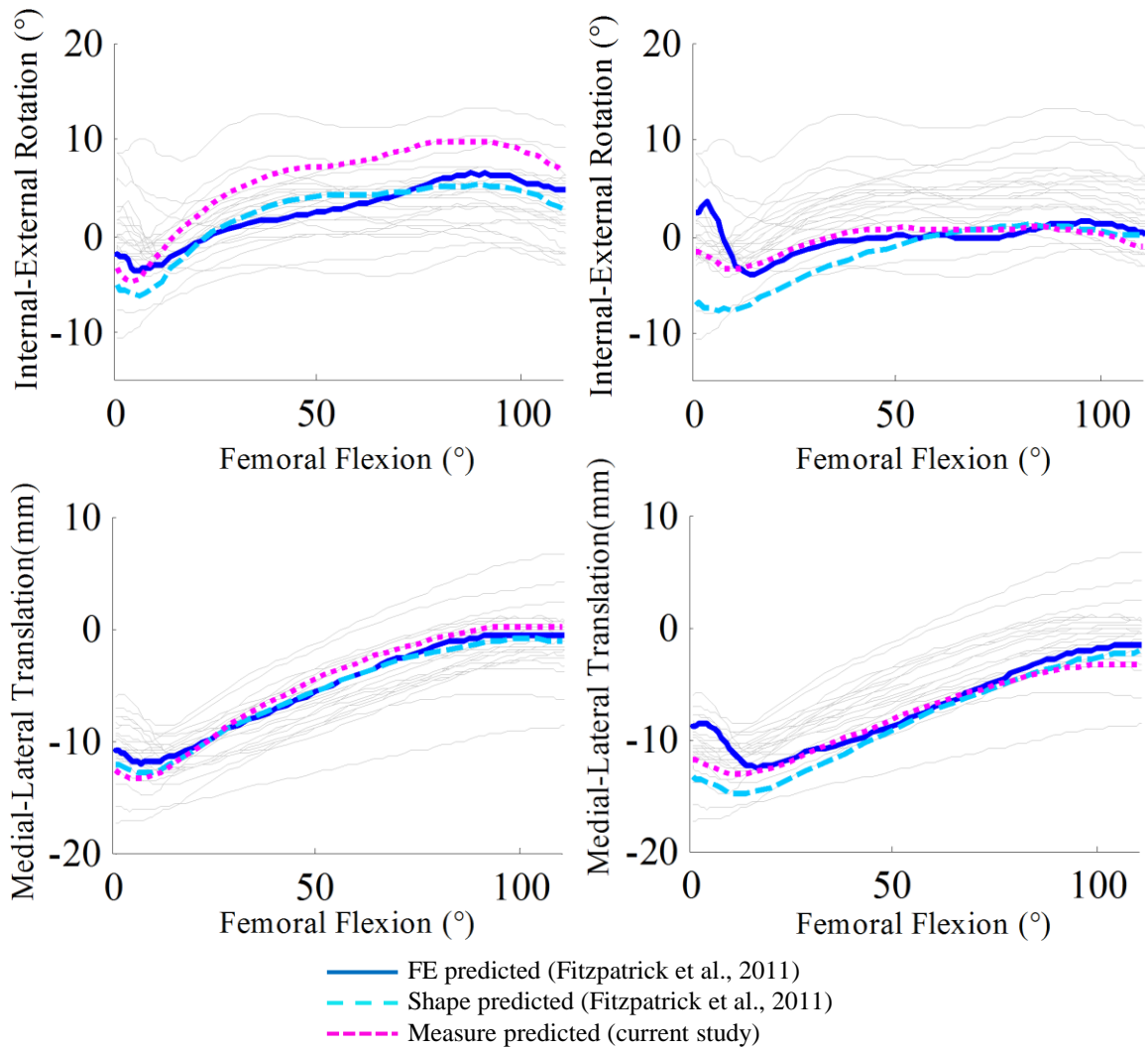


Figure 5.3 Comparison of measure-based (current study) and shape-based kinematics (Fitzpatrick et al. 2011) to training set kinematics (Fitzpatrick et al. 2011) for two representative subjects (bold curves). Training set kinematics (from FE) are shown in gray and illustrate the spread for each degree of freedom.

Table 5.1 Descriptive statistics for the linear measures of the PF joint.

Measurement	Mean	Standard Deviation	Min	Max
Femur Sulcus Width (mm)	32.6	5.8	15.3	42.0
Femur Anterior Sulcus Angle (deg)	150.2	9.2	134.2	165.0
Femur AP Width (mm)	60.7	4.6	51.6	68.0
Femur Distal Sulcus Angle (deg)	107.0	11.8	82.3	128.7
Femur Lateral Trochlear Inclination (deg)	16.0	3.8	10.4	21.5
Femur Medial Trochlear Inclination (deg)	166.2	6.8	154.9	177.7
Femur ML Width (mm)	79.4	7.4	66.6	92.8
Femur Trochlear Angle (deg)	4.3	2.7	0.3	11.1
Patella Angle (deg)	122.1	7.5	110.7	140.6
Patella SI Height (mm)	39.7	3.8	34.7	44.8
Patella ML Width (mm)	42.7	4.0	35.8	50.6
Insall-Salvati Index	1.4	0.2	1.0	2.0
Bisect Offset (%)	60.9	8.0	43.4	74.1
Intercondylar Notch Width (mm)	23.0	2.8	17.3	27.6
Trochlear Groove Angle (deg)	-4.2	4.9	-12.5	4.8

Table 5.2 Cumulative variability explained with the specified number of modes of variation.

Mode	Cumulative Variability (%)
1	40.1
2	59.1
3	70.1
4	76.7
5	82.7
6	87.1
10	95.7
23	100

Table 5.3 Mean RMS error and standard deviations (SD) for individual sets of predictive measures for each kinematic DOF. Difference is between FE-predicted and measure-predicted kinematics.

DOF	Predictive Measures	Top 3 Measures Mean (SD)	All 15 Measures Mean (SD)
FE (deg.)	Femur Epicondylar Width Femur AP Width Patella SI Height	2.91 (1.47)	3.22 (1.59)
VV (deg.)	Patella Angle Patella ML Width Patella SI Height	1.43 (0.98)	1.71 (0.86)
IE (deg.)	Femur Sulcus Angle Medial Trochlear Inclination Trochlear Groove Angle	2.59 (1.33)	2.84 (1.70)
ML (mm)	Femur Sulcus Width Bisect Offset Trochlear Groove Angle	2.05 (1.15)	2.27 (1.13)
AP (mm)	Femur Distal Sulcus Angle Patella ML Width Insall-Salvati Index	1.22 (1.38)	1.36 (0.98)
SI (mm)	Insall-Salvati Index Femur AP Width Patella SI Width	2.53 (1.47)	2.57 (1.47)

CHAPTER 6. STATISTICAL SHAPE MODELING PREDICTS PATELLAR BONE GEOMETRY TO ENABLE STEREO-RADIOGRAPHIC KINEMATIC TRACKING

6.1. Abstract

Complications in the patellofemoral (PF) joint of patients with total knee replacements include patellar subluxation and dislocation, and can require revision. Such complications are characterized by excessive rotation and translation between the patellar and femoral components and thus require accurate *in vivo* evaluation techniques. Stereo-radiographic and 3D-2D registration techniques are capable of high accuracy; however, the radiotransparent nature of the patellar component requires alternative means of tracking the patella. The objective of the current study was to develop a virtual stereo-radiographic platform for geometric prediction of subject-specific implanted patellar bone geometries from 2D radiographic images for use in 3D-2D tracking. A statistical shape model (SSM) of the patellar bone was developed from magnetic resonance images of 50 subjects and each subject's geometry was separately predicted in a leave-one-out approach to evaluate the necessary number of simulated 2D target profiles of the bone. Five unique radiographic perspectives of the bone provided optimal 2D target matching and an average 3D geometric error of 0.45 ± 0.07 mm (mean \pm standard deviation), which is comparable to the accuracy of traditional imaging segmentation errors. The ability to predict the remaining natural patellar bone geometry of the implanted PF joint

instead of CT segmentation can reduce radiation exposure and eliminate time and cost from *in vivo* kinematic analyses.

6.2. Introduction

Patellofemoral (PF) joint complications continue to account for a significant percentage of total knee replacement (TKR) revisions (Dalury et al., 2003; Rhee et al., 2008). Pathologies such as patellar subluxation and maltracking are characterized by medial-lateral (ML) translation and internal-external rotation of the patella (Singerman et al., 1997; Kawano et al., 2002) and are a common cause of TKR revisions (D’Lima et al., 2003). Measuring dynamic *in vivo* PF joint kinematics to understand these complications continues to be a challenge for patients with total knee replacements (TKR) because of the need for accuracy in multiple degrees of freedom (DOF) and the difficulty in tracking the implanted patellar bone or component. Current *in vivo* kinematic measurement techniques for the knee include static (Fellows 2005) and dynamic (Powers et al., 2003; von Eisenhart-Rothe et al., 2004; von Eisenhart-Rothe et al., 2007; Sheehan et al., 2009; Carpenter et al., 2009) magnetic resonance (MR) imaging; however, static MR images have been unable to reproduce dynamic joint motion and dynamic MR studies have relied on combining scans from multiple cycles (Bey et al., 2008). Dynamic single-plane fluoroscopy has also been used to evaluate sagittal plane *in vivo* PF kinematics for TKR patients during high-flexion activities (Komistek et al., 2000, Stiehl et al., 2001, Argenson et al., 2005, Leszko et al., 2010). In particular, the sagittal angle of the patellar bone resection surface was tracked relative to the tibial long axis and an assumed PF

contact location was defined by the shortest perpendicular distance between the femoral component and patellar mass center.

Stereo-radiography or biplane fluoroscopy has enabled *in vivo* kinematic analysis of the natural tibiofemoral (TF) (You et al., 2001; Li et al., 2008, Bey et al., 2008) and patellofemoral (PF) (Nha et al., 2008; Bey et al., 2008) joints, as well as in the implanted TF joint (Bingham 2006; Hanson 2006). Studies have used three-dimensional to two-dimensional (3D-2D) registration of virtual bone models or computer-aided-design (CAD) models of metallic implants to fluoroscopic images for 3D pose extraction of the joint (Mahfouz et al., 2003; Bingham et al., 2006). Comparing a 3D-2D registration method between dual-plane and single-plane systems, Zhu et al. reported sub-millimeter and sub-degree accuracies for TF joint tracking with a dual-plane system; this amounted to 2x in-plane and 10x out-of-plane improvements in accuracy over their single-plane system (Zhu et al., 2012). Recently, a high speed stereo-radiographic imaging system was developed at the University of Denver for tracking *in vivo* joint kinematics (Ivester et al., 2015). Using a 3D-2D registration method of digitally reconstructed radiographs (DRRs) from a CT-based 3D model, tracking error for a phantom knee joint was 0.15 mm (S.D. 0.13 mm) and 0.41° (S.D. 0.30°) in translation and rotation, respectively. Stereo radiographic tracking of the implanted patella is challenging because the patellar implant is radiotransparent and while tracking embedded beads is accurate to <0.1 mm and 0.1° (Bingham et al., 2006), this method requires custom modified implants and does not translate easily to large-population studies. Without beaded implants, the resected patella requires either pre-surgical imaging of bones and precise implant placement or

post-surgical imaging, which is challenging due to imaging artifacts, expensive, and increases patient exposure.

Statistical shape models (SSMs) offer an alternative means of obtaining subject-specific bone geometry. SSMs have been used to characterize the morphology of individual bones and whole joints (Yang et al., 2008; Bryan et al., 2010; Rao et al., 2013; Smoger et al., 2015) and, more recently, to estimate 3D shape and 6-DOF pose from 2D image sets (Laporte et al., 2003; Zheng et al., 2006; Kurazume et al., 2009; Zhu et al., 2011, Baka et al., 2012). Laporte et al. described a method for first optimizing scale and rigid body alignment of one generic model of the distal femur and then applying a kriging algorithm to deform the generic shape to match the 2D radiograph contours (Laporte et al., 2003). Zheng et al. improved upon the prior study by introducing an SSM of the distal femur to allow for physiologic perturbations of the shape and automatic Canny edge detection in the radiographs to reduce operator error (Zheng et al., 2006). Kurazume applied a similar SSM-based projection-radiograph optimization method to the proximal femur and achieved sub-mm errors (Kurazume et al., 2009). Their SSM was built from 56 subjects and ultimately 10 SSM shape parameters were used to make their predictions. Baka et al. have dually predicted shape and pose of the TF joint from biplane fluoroscopic images of a gait cycle, avoiding the need for additional scanning and reconstruction (Baka et al., 2012).

Limited work has been done to reconstruct subject-specific patellae from fluoroscopic images to track the motions of the PF joint. Furthermore, reconstruction of resected bones with limited shape profile information has also not been evaluated.

Accordingly, this study proposes an SSM-based reconstruction method that can accurately recreate 3D implanted patellar geometry from fluoroscopic images. The objective of this study was to develop a virtual platform of a stereo-radiographic imaging system and evaluate the predictive capability of an SSM to generate subject-specific 3D patellar geometries from simulated target profiles to enable tracking of *in vivo* PF kinematics. The study informs future experimental protocols without risk to patients by utilizing a cohort of previously segmented patellar geometries. The study also evaluates the number of views and orientations required to produce quality geometric predictions. The prediction algorithm also highlights the utility of an edge detection technique with nearest neighbor search.

6.3. Methods

An SSM of the healthy normal patellar bone was developed from a training set of 50 subjects. The subjects included 25 males and 25 females whose average age was 64 years (range: 44 to 87), average weight was 73 kg (range: 43 to 127), and average body mass index (BMI) was 25.2 (range: 19.0 to 41.3). Data used in the preparation of this article were obtained from the Osteoarthritis Initiative (OAI) database, which is available for public access at <http://www.oai.ucsf.edu/>. Specific datasets used are 0.E.1, which consists of baseline (initial healthy) scans. Subjects were included if they were deemed healthy and normal with no signs of osteoarthritis. The patellae were reconstructed from MR scans using ScanIP (Simpleware, Exeter, UK) and registered to a template mesh according to [Rao 2013; Smoger 2015]. Registration was performed through an iterative closest point algorithm and provided nodal correspondence between all subjects in a

common local coordinate system. The template mesh consisted of 472 nodes and average element edge lengths were approximately 3 mm. The local coordinate system was developed using the proximal, distal, and lateral points around the articular periphery of the template mesh with the origin located at the geometric centroid [Rao 2013].

The SSM was established by applying PCA to the training set of 50 subjects. Each subject's shape was represented by a 1416 x 1 vector of its registered 3D nodal coordinates (x, y, z). PCA was applied to the covariance matrix of the training set data. PCA is a widely-used statistical technique to decompose a large data set into its primary modes of variation or principal components (PCs). The analysis resulted in a series of 49 non-zero eigenvalues characterizing the amount of variability explained and an associated eigenvector matrix. The modes of variation described the anatomic variation present in the dataset and enabled both training set subjects and new instances of the SSM to be represented by a series of PC scores.

An SSM of the healthy normal patellar bone was developed from a training set of 50 subjects. The subjects included 25 males and 25 females with an average age of 64 years (range: 44 to 87), average weight of 73 kg (range: 43 to 127), and average body mass index (BMI) of 25.2 (range: 19.0 to 41.3). Data used in the preparation of this article were obtained from the Osteoarthritis Initiative (OAI) database, which is available for public access at <http://www.oai.ucsf.edu/>. Specific datasets used are 0.E.1, which consists of baseline (initial healthy) scans. Subjects were included if they were deemed healthy and normal with no signs of osteoarthritis. The patellae were reconstructed from MR scans using ScanIP (Simpleware, Exeter, UK) and registered to a template mesh

according to (Rao et al., 2013; Smoger et al., 2015). Registration was performed through an iterative closest point algorithm and provided nodal correspondence between all subjects in a common local coordinate system. The template mesh consisted of 472 nodes and average element edge lengths were approximately 3 mm. The local coordinate system was developed using the proximal, distal, and lateral points around the articular periphery of the template mesh with the origin located at the geometric centroid (Rao et al., 2013).

The SSM was established by applying PCA to the training set of 50 subjects. Each subject's shape was represented by a 1416 x 1 vector of its registered 3D nodal coordinates (x, y, z). PCA was applied to the covariance matrix of the training set data. PCA is a widely-used statistical technique to decompose a large data set into its primary modes of variation or principal components (PCs). The analysis resulted in a series of 49 non-zero eigenvalues characterizing the amount of variability explained and an associated eigenvector matrix. The modes of variation described the anatomic variation present in the dataset and enabled both training set subjects and new instances of the SSM to be represented by a series of PC scores.

A virtual model of the stereo-radiography system was developed to simulate an experimental data collection on a population of subjects. The model was based on an experimental configuration and subject pose consistent with prior data collections in the knee (Kefala et al., 2015). Experimental images and projection parameters were collected for a single subject as a part of a larger IRB-approved study. The subject was imaged in the sagittal and transverse directions with respect to cameras A and B,

respectively (Figure 6.1). To avoid occlusion from the metallic implants and surrounding tissue, the knee was imaged at 45° flexion. Radio-opaque markers were placed on the patella to locate the patella in the imaging volume of the system. A direct linear transform (DLT), which maps 3D objects onto the camera's 2D image plane, was calculated in a calibration process (Brainerd et al., 2010). Briefly, a DLT is estimated by identifying, in each camera image, points on a cube at known relative positions in the 3D object space. The markers were digitized on the radiographs and the DLT transformed the digitized points into the 3D object space to locate the virtual imaging volume. Marker digitization and camera calibration was conducted in XRayProject (XROMM, Brown University).

For each patella in the training set, an appropriately-sized patellar implant was selected and located, the bone was virtually resected (Ali et al., 2015), and simulated 2D images representative of the stereo-radiography system were generated. Virtual implantation of the training set patellae was achieved by optimizing size and placement of a commercially available patellar implant component to retain the natural thickness and maximize coverage of the implant with less than 2 mm of overhang (Figure 6.2). A transformation was calculated between the training set and marker reference frames to locate the 50 patellae in the imaging volume and to the approximate imaged position of the joint. A horizontal rotation was then applied to each patellae and its associated resection plane in the object space to simulate five imaged positions with respect to the experimentally imaged position (Figure 6.3). Using the DLT, nodes for each patella and resection plane pair were mapped to the virtual 2D image planes for all 5 positions

resulting in 10 unique views of the patella. Positioning actual knee joints for a cohort in the imaging volume would likely introduce some random alignment variability between the patella and the image planes. To account for this, each patella was randomly perturbed in the imaging volume (prior to applying the DLT) by up to ± 5 mm and $\pm 5^\circ$. An alpha-shapes algorithm outlined 2D profiles of the projected vertices of the intact patella. Briefly, alpha-shapes are a generalization of the convex hull and is useful for outlining point clouds with varying levels of complexity (Edelsbrunner et al., 1983). The intact profile was then separated into an anterior and posterior region by locating the two intersecting points of the intact and resection profiles. The anterior region, representing the remaining natural surface projections, was used to simulate each TKR-implanted patella's resected target profile.

A leave-one-out type of analysis was performed on three different sets of imaged positions including the 1st position alone (2 images), the 1st, 3rd, and 5th positions (6 images), and all five positions (10 images). Each of the 50 subjects were separately left out of the training set and new, 49-subject SSMs were built. An optimization algorithm was designed to change shape and alignment of the new instance of the SSM to match the 2D anterior target profiles of the left-out patella (Figure 6.4). The objective function minimized the difference between the 2D anterior target profiles and the project profile of the 3D SSM. 2D image plane error, E , was calculated as the average of the root-mean-square (RMS) errors, e_i , across the images:

$$E = F(X) = \frac{1}{n} \sum_{i=1}^n e_i \quad (6.1)$$

$$e_i = \sqrt{\frac{1}{m} \sum_{j=1}^m d_{ij}^2} \quad (6.2)$$

RMS error was calculated using the 2D Euclidean distances, d_{ij} , measured between pairs of matched points in each image:

$$d_{ij} = \sqrt{\{(x_{ij} - \hat{x}_{ij})^2 + (y_{ij} - \hat{y}_{ij})^2 + (z_{ij} - \hat{z}_{ij})^2\}} \quad (6.3)$$

where n equals the number of images (or twice the number of positions) and m equals the number of matched points in an image. Design variables included 6 pose (3 rotation, 3 translation) parameters and 18 shape parameters, which accounted for 95% of the variability in the training set. Side constraints were placed on the design variables in an effort to limit the model to realistic geometries. The shape parameters were bounded by ± 3 standard deviations to ensure realistic instances; rotation and translation design variables were bounded by $\pm 20^\circ$ and ± 50 mm, respectively.

Given a manually aligned starting pose of the mean SSM instance, its nodes were projected onto the image planes and the alpha-shapes profiles were matched to the simulated anterior target profiles using a perpendicular nearest neighbor search algorithm. Since imaged positions were linked by the known transformation between them, only one set of pose parameters was optimized to simultaneously align projections in multiple imaged positions. To ultimately assess accuracy, 3D error on only the anterior region (as defined by the cut plane) was calculated as the Euclidean distance in mm between matched nodes for the SSM prediction and original patellar geometry.

6.4. Results

The statistical shape model was developed to characterize anatomic variation in a small number of shape parameters. The first three modes of variation were visualized by individually perturbing the mean geometry by ± 1.5 standard deviations of each PC. This

level was chosen to qualify the geometric differences and maintain realistic instances given the size of the training set. The first PC mode accounting for 65.0% of the total variation, was strongly correlated to uniform scaling ($r = -0.95$) (Figure 6.5). The second PC mode, accounting for 6.5% of the total variation, primarily described shape changes including the ML/AP aspect ratio and significant concavity of the articular surface at -1.5 standard deviations compared to a flat articular surface at -1.5 standard deviations. The third principal component, accounting for 4.6% of the total variation, resulted in changes in shape of the medial articular facet and mediolateral shift of the apex were the most significant shape variations in this mode of variation. 18 PCs, which were used in the optimization, accounted for 95% of the total variation.

The number of images required to accurately predict the 3D patellar geometry was evaluated by comparing three scenarios involving 1, 3, and 5 positions for each left-out subject (Figure 6.6). Errors from these scenarios were averaged across all subject predictions. Using only the 1st (experimentally imaged) position, composed of a sagittal and axial or merchant view, the average 2D image plane error on the anterior region was 0.48 ± 0.15 pixels (mean \pm std. dev.) (Figure 6.7). The associated average 3D geometric error was 0.58 ± 0.12 mm with noticeable differences where the patellar profile was not visible in the image. Image sets using positions 1, 3 and 5 together achieved average 2D image plane errors of 1.05 ± 0.61 pixels and 0.48 ± 0.10 mm for 3D geometric error. Using all 5 positions resulted in the largest average 2D image plane error (1.33 ± 0.50 pixels), but the lowest 3D geometric error (0.45 ± 0.07 mm) and better representation of the actual geometry across the anterior surface (Figure 6.8).

On average, a single subject optimization completed in 58, 60, and 29 iterations spanning 10, 22, and 19 minutes for 1, 3 and 5 positions, respectively. In all cases, the average PC scores for the predicted patellar geometries was zero, which indicates that the algorithm generated a predicted set of patellae with an equally balanced amount of variation.

6.5. Discussion

An approach was developed to predict a 3D SSM-based geometric representation of the anterior patellar bone geometry from sets of paired stereo-radiographic images, with the benefit of enabling tracking of *in vivo* PF kinematics for TKR subjects without requiring specialized beaded implants or additional imaging. The computational approach here utilized a leave-one-out type of analysis to robustly and safely evaluate the predictive capability of the approach by using 50 subject-specific geometries to generate simulated target profiles similar to those achieved via edge detection methods. The current approach eliminated the need for imaging and thus may significantly reduce radiation exposure in some protocols. Radiation dose level for a knee CT was reported to be 0.16 mSv (Biswas et al., 2009) whereas the dose in the current protocol was less than 0.006 mSv (PCXMC STUK, Radiation and Nuclear Safety Authority, Helsinki, Finland), or about 4% of the radiation a person would receive from CT. Furthermore, 0.006mSv is about one day of natural background radiation in the US. The stereo-radiography simulation platform was well suited to assess accuracy for the various pose scenarios without impact on patients; the best performing scenario will be implemented in future *in vivo* data collections.

The SSM developed in this study described the main modes of variation in a population of 50 subjects. As in other studies (Bryan et al., 2010, Rao et al., 2013, Smoger et al., 2015), scaling is the primary mode of variation. In structures like the patella whose geometry is relatively convex compared to the neighboring femur and tibia, it is understandable that scaling would account for 65%, a significant amount of the overall variability. Mode 2 shape variation, which described the concavity of the articular surface, was also observed in a previous study that developed an SSM of the cartilage in the PF joint (Fitzpatrick et al., 2011). This comparison illustrates a broader capability of SSMs to consistently characterize shape variation in related structures (i.e. patellar bone and cartilage).

The robustness of the algorithm to predict 3D geometries from 2D fluoroscopic images was evaluated with a leave-one-out type of analysis. Each of the 50 patellae were separately left out of the SSM training set and used to simulate 2D target profiles for the SSM to match. Differences between the actual and predicted patellae occurred primarily where the geometry was not well captured by the profile edges. When more positions were incorporated into the optimization, differences in the average 3D shape (mean and std. dev.) decreased; average 2D errors increased in these scenarios as the optimization required balancing the 3D shape over multiple profiles. 3D geometric error exists in regions hidden from the 2D target profiles (particularly when using only 1 position), which suggests that shape variability at the poles is not strongly correlated to adjacent regions. Evaluation of each subject excluded from the SSM training set illustrates the ability to describe new patellar geometries with the SSM parameters.

The alpha-shapes algorithm used to outline the dense 3D point projections provided similar results to edge-detection techniques (Canny et al., 1986) and is presented here along with a perpendicular nearest neighbor search as an alternative method to the application of digitally reconstructed radiographs for 3D-2D registration. The rounded shape of the patella is an ideal geometry for the alpha-shapes algorithm and a perpendicular nearest neighbor search because interior and hidden edges are uncommon and the radial nature of the projected image reduces the number of possible nearest neighbors, thus improving optimization speed. This method similar to the 2D distance maps developed by Kurazume et al. but is simpler to implement (Kurazume et al., 2009).

Compared to shape prediction techniques from natural bone images (Baka et al., 2011; Li et al., 2008), the proposed methodology was applied to an implanted geometry and thus requires experimental protocol and computational processing that adds some complexity. Specific positions of the patella must be imaged in order to capture enough of the subtle shape variability. Existing natural studies have used fluoroscopic images taken directly from the activities they seek to track because the bones have so far been intact and more complex in their shape. The implanted patella presents a challenge in that a portion of the bone is removed and surrounding metallic implants may occlude some or all of the remaining patellar bone in dynamic 6-DOF activities. Furthermore, the geometries of the natural femur and tibia provide more information in a single set of biplane images. The additional snapshot images proposed in this methodology represent a small increment and thus should not be considered as added risk especially if it eliminates CT scanning.

The ability to track *in vivo* PF kinematics with a 3D-2D registration method depends on the geometric accuracy of the 3D model, the registration algorithm, and the accuracy of the 2D image edge detection protocol. By optimizing pose of a deformable SSM to simulated target profiles, our method focused on recreating accurate 3D geometric models. Baka et al. reported a 0.78 mm point-to-surface difference between their SSM-based femur bone prediction and ground truth models (Baka et al., 2012). Baka et al. applied their shape prediction method to simultaneously track the femur in a biplane fluoroscopic setup and achieved average tracking errors less than 0.07 mm translation and less than 0.2° rotation except for longitudinal rotation, which was reported at 0.32° (Baka et al., 2014). Similarly, Zhu et al. reported an absolute average geometric error of 0.9 mm for the femur bone prediction. Furthermore, geometric errors reported here are less than the slice thickness of most MR and CT image sets, which is typically 0.7 mm (Zhu et al., 2011). Comparable geometric errors to previous studies indicate that the predictions generated here are sufficient for tracking in single and dual-plane studies.

In summary, this study evaluated the ability of an SSM to predict the 3D natural geometry of the implanted patellar bone from 2D stereo-radiographic images of the knee joint. The method eliminates the need for prior CT imaging and segmentation, which is especially challenging in the TKR implanted knee. The level of accuracy achieved in the current study exceeds existing 3D geometric predictions of adjacent bones and is comparable to traditional segmentation considering inter-rater variability, making it sufficient to perform kinematic tracking of TKR subjects. These results are promising, however further work is needed to evaluate this technique experimentally.

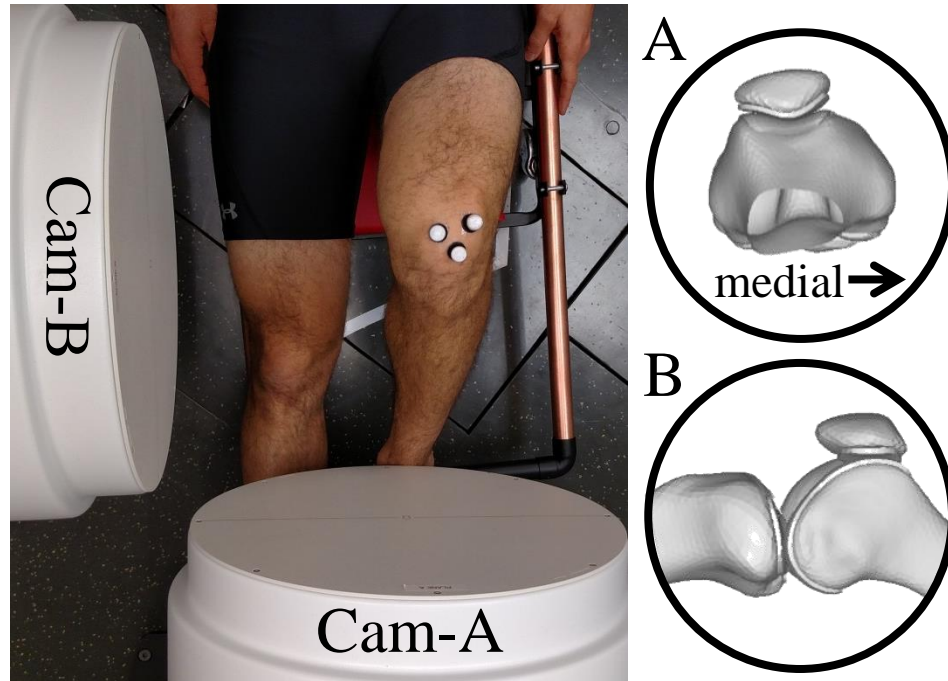


Figure 6.1 Imaged position of the flexed left knee in the high speed stereo radiography (HSSR) system, top view (left). Representation of the imaged knee as seen on camera planes A and B (right). Note: Subject is supine.

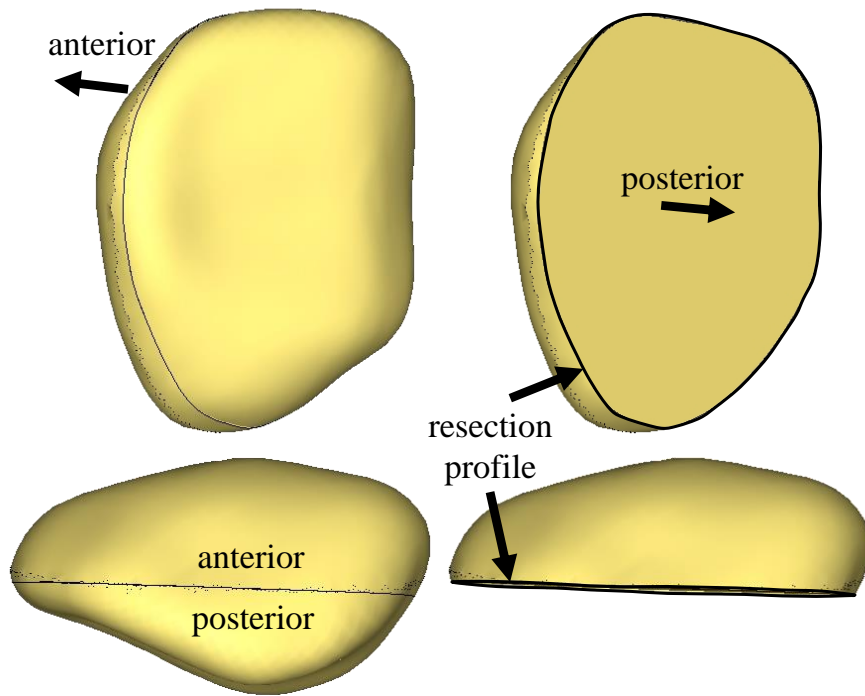


Figure 6.2 A representative intact patella (left) and, after automated implantation, its resected version (right).

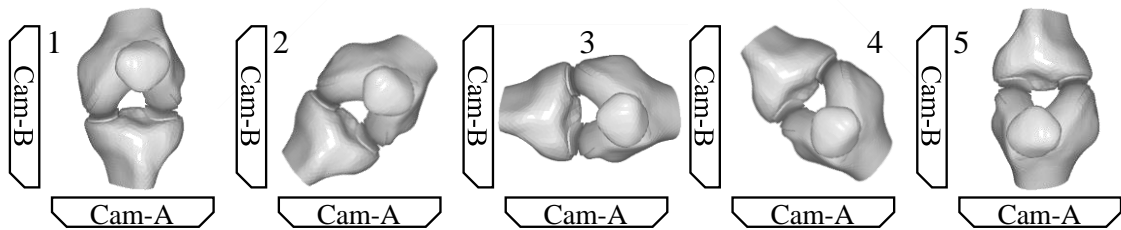


Figure 6.3 Proposed imaging positions with varying orientation in the horizontal plane of the stereo-radiography system.

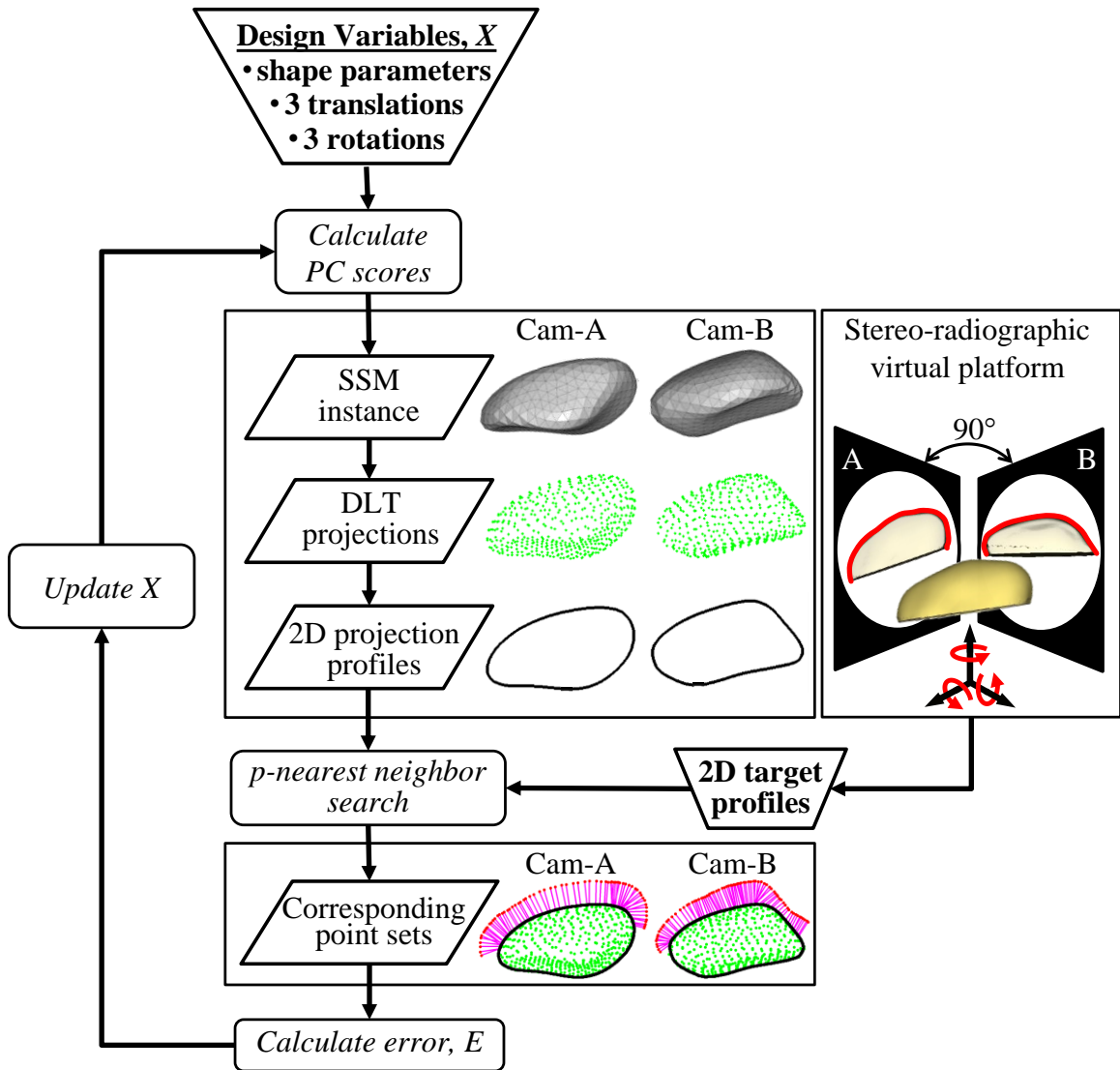


Figure 6.4 Schematic of the optimization algorithm to reconstruct the full 3D patellar geometry from simulated sparse data. PC scores of the patellar bone SSM are optimized until the profile (black) of the projected point cloud (green) matches the simulated target profiles (red). The magenta lines represent corresponding points on the target and predicted profiles. RMS error calculated between these corresponding point sets is minimized by the optimization algorithm.

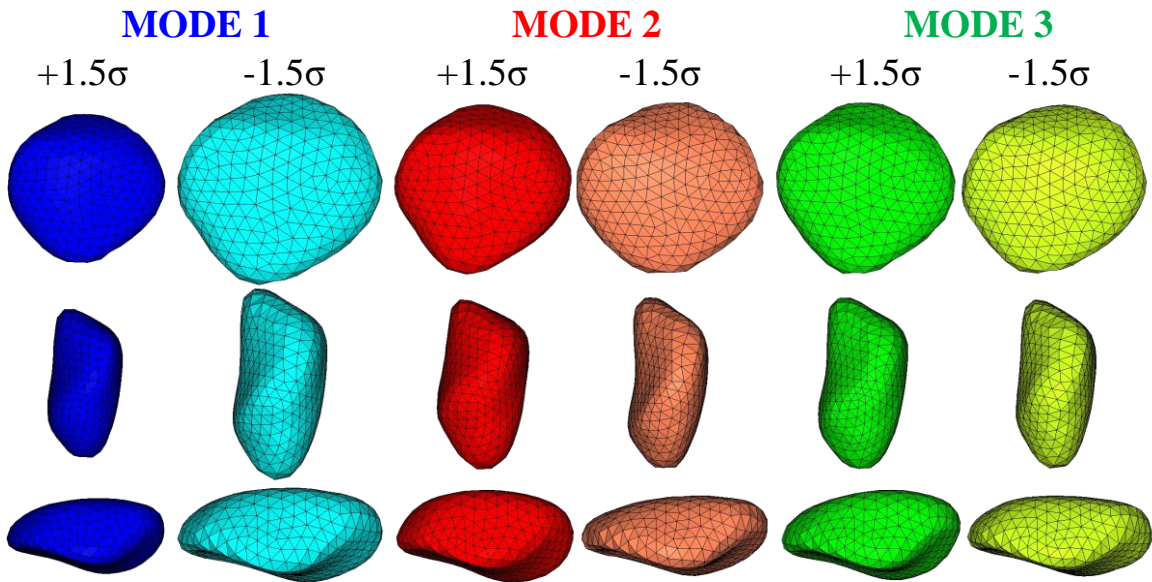


Figure 6.5 Representations of patellar bone for the first three principal component modes. Patellae are shown at +/- 1.5 standard deviations. Views include coronal (top), sagittal (middle), and transverse (bottom).

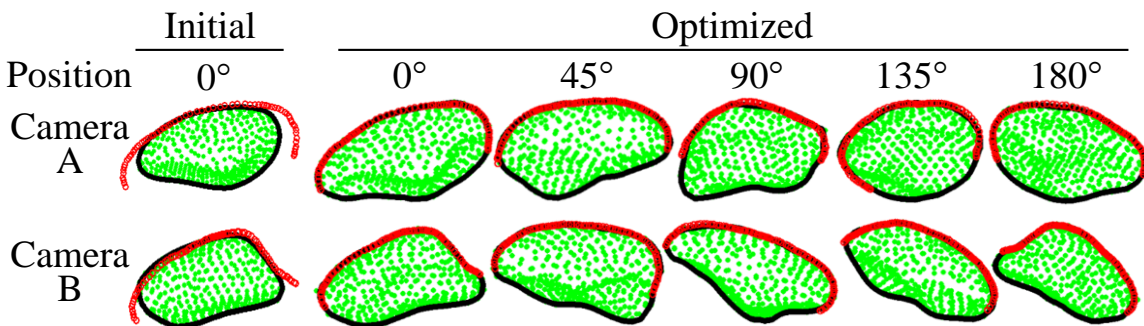


Figure 6.6 Nodes of an instance of the patellar bone SSM (green) projected by the DLT onto the camera image planes and its profile (black). The anterior region of the target profiles for a representative left-out subject (red). One position is shown for rigid body alignment of the mean instance and then all five positions over ~180° for the optimized instance.

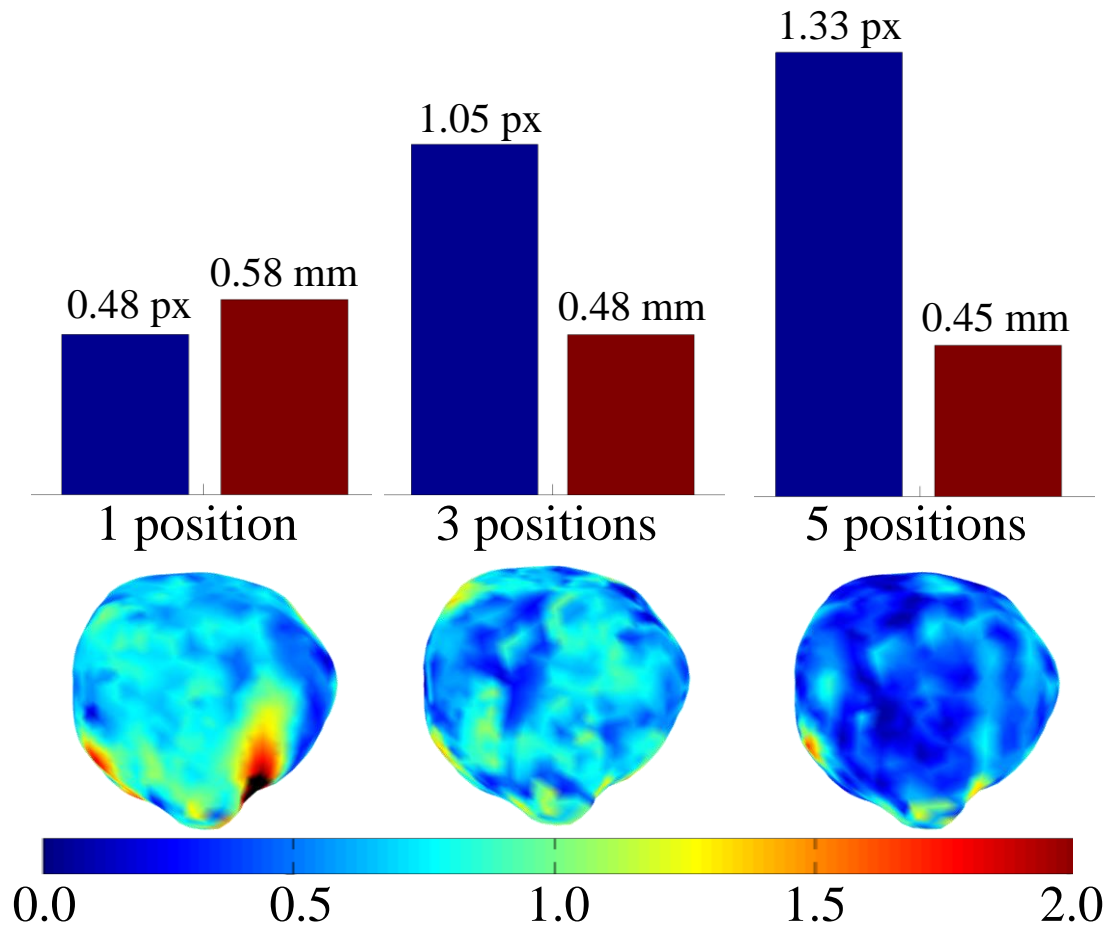


Figure 6.7 Comparison of the three imaging scenarios for a representative subject; the 1st position (left), the 1st, 3rd, and 5th positions (center), and all five positions (right). Bar charts show the 2D image plane error (blue) in pixels and anterior surface 3D geometric error (red) in millimeters for each scenario. Contours represent absolute difference between the actual and predicted shape for the resected case. Contour units are in millimeters.

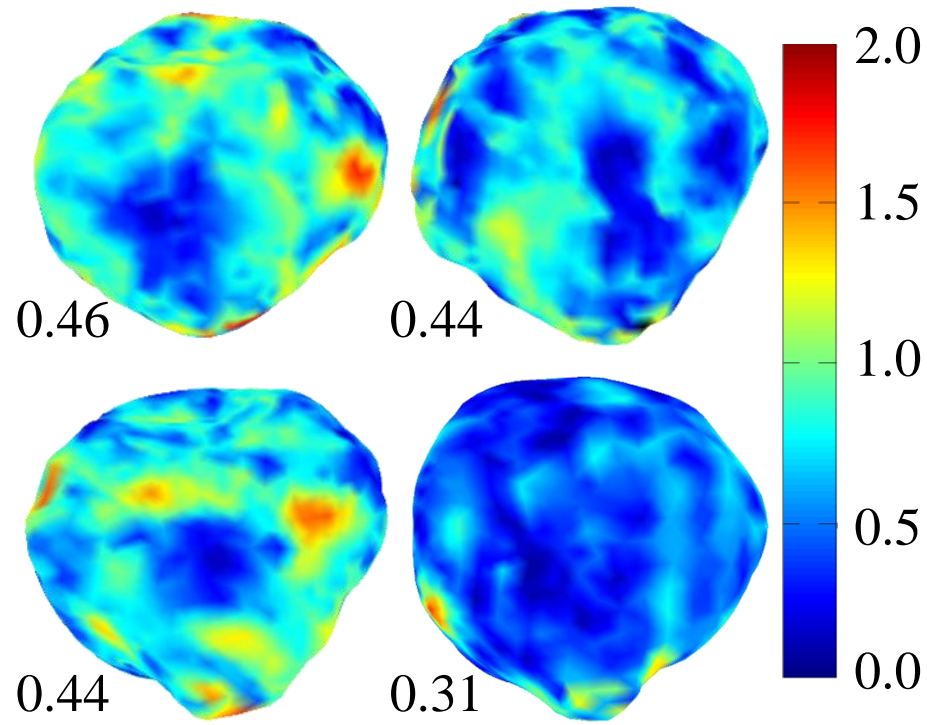


Figure 6.8 Contours of absolute difference between the actual and predicted shape for the resected case using all 5 positions. Four representative subjects are shown. Individual RMS errors are reported next to each subject. Units are in millimeters.

CHAPTER 7. PREDICTION OF KNEE ARTICULAR CARTILAGE FROM 3D BONE GEOMETRY USING A STATISTICAL SHAPE MODEL

7.1. Abstract

Finite element (FE) models of the natural knee are used to evaluate mechanics of the articular cartilage that are otherwise challenging to measure. These investigations require accurate three-dimensional (3D) representations of the cartilage, which is typically segmented from magnetic resonance (MR) images. Substituting segmented geometries with an accurate statistical shape model (SSM) representation could reduce costly and time-consuming imaging and establish norms for cartilage thickness maps. While segmentation processes have been improved with the assistance of SSMs, 3D models sufficient for complex computational analyses have not yet been developed without the assistance of MR imaging. The objective of this study was to develop an SSM of the bone and articular cartilage in the whole knee joint and to predict subject-specific, FE-ready cartilage volumes given only the registered bone geometry. An SSM of bone and cartilage geometry was developed from 50 MR scans of healthy normal subjects. The cartilage geometry was linked directly to a hexahedral mesh by an efficient mesh-morphing algorithm. Principal component analysis (PCA) described common modes of variation across the training set. A predictive PCA approach quantified the degree to which bone and cartilage modes were correlated. A leave-one-out type of

evaluation predicted subject-specific cartilage from new bone geometry for a training set of 50 subjects. Coverage predictions were within 2 mm and average thickness accuracy was within 0.55 mm across all cartilages. These results illustrate the potential to develop computationally sufficient cartilage representations without the need for imaging, segmentation, and mesh processing.

7.2. Introduction

Articular cartilage of the knee allows the joint to function normally by permitting smooth articulation, efficient load transfer and, due to its aneural and avascular properties, pain-free movement. Cartilage damage may occur as a result of the significant loading and kinematic requirements in everyday activities. Cartilage degradation typically leads to joint pain and often requires intensive surgical intervention, such as total knee replacement (TKR). Hence, many studies have sought to understand the morphology and properties of knee articular cartilage through a variety of computational research methods including clinical assessments, finite element (FE) models, or for osteoarthritis (OA) disease progression (Andriacchi et al., 2006; Harris et al., 2012; Omoumi et al., 2015). Furthermore, small differences have been reported to significantly impact contact mechanics. Li et al. developed an FE model of the knee to evaluate the effect of cartilage thickness on contact mechanics and reported that 9% increase in peak surface pressure occurred with 10% thinning of cartilage (Li et al., 2001).

Studies have investigated relationships between bone and cartilage morphology to evaluate causes OA, establish norms for cartilage distribution and thickness, and inform

automated segmentation algorithms. Neogi et al. performed linear discriminant analysis on a three-dimensional (3D) active appearance model of knee bones to show that bone shape can predict the onset of radiographic knee OA (Neogi et al., 2013). Faber et al. reported statistically significant differences in cartilage volume between men and women and attributed it to the larger male joint surface (Faber et al., 2001). Increased cartilage thickness has also been correlated with regions of contact in normal knees (Li et al., 2005), suggesting that shape and alignment of a joint may provide insight into the state of the cartilage structures. Connolly et al. evaluated cartilage thickness across different flexion regions of the femoral condyles and tibial plateaus; cartilage was thicker in the posterior regions of the femoral condyles (Connolly et al., 2008).

Describing the 3D representation of knee joint geometry is typically achieved from segmentation of computed tomography (CT) or magnetic resonance (MR) imaging. CT is preferred for characterizing bony anatomy in preparation for TKR surgery (White et al., 2008); however, it does not provide details regarding soft tissue structures. While MR imaging captures cartilage and other soft tissues, segmenting these structures is typically a manual process and may take several hours to complete (Koo et al., 2005). Additionally, manual segmentation requires a working knowledge of anatomy and experience with the imaging modalities to reduce operator error.

Algorithms to speed up the segmentation process have employed statistical shape models (SSMs) to automatically detect bone and cartilage boundaries in MR images and create gross 3D models of the cartilage (Folkesson et al., 2007, Fripp et al., 2010, Solloway et al., 1997, Yang et al., 2015). Development of an SSM involves establishing

correspondence in a training set of subject geometries and then performing principal component analysis (PCA) to determine the common modes of variation in the data. Solloway et al. built a 2D SSM of the enclosed regions on MRIs in order to efficiently locate bone and cartilage interfaces. More recently, 3D SSMs have been developed to improve accuracy and efficiency by including bone-cartilage interface probability maps (Fripp et al., 1997) and differentiating between healthy and osteoarthritic populations (Folkesson et al., 2007).

SSMs have also gained popularity as useful tools for describing anatomic variation and evaluating sparse data to make predictions about bone shape or joint function. The approach has been successfully applied to describing morphology in the knee bone (Bryan et al., 2010) and cartilage (Baldwin et al., 2010), in the human brain (Reuckert et al., 2003) and in joints with multiple structures (Rao et al., 2013; Yang et al., 2008). Baka et al. exploited the deformable nature of SSMs to predict pose and 3D geometry of the femur and tibia from stereo-radiographic images (Baka et al., 2011). Recent work has assessed relationships between shape and function by performing PCA with geometric, contact mechanics, and kinematic data (Fitzpatrick et al., 2011; Smoger et al., 2015). These studies were able to predict kinematics and contact mechanics from the shape of the joint.

Accordingly, the objective of the current study was to combine an SSM of bone and cartilage in the whole knee joint with a predictive modeling approach to estimate cartilage geometry from local bony anatomy. Specifically, an SSM of the femoral, tibial, and patellar bone and cartilage surface geometries was developed from MR images to

quantify relationships between morphology of bone and cartilage. The model described the associated variability in bone and cartilage with a set of shape parameters. An established predictive algorithm evaluated the strength of the relationships between bone and cartilage within each shape parameter (Fitzpatrick et al., 2011). In the current study, the algorithm predicted cartilage shape for a new bony geometry by characterizing the bone shape with model shape parameters and leveraging these bone-cartilage shape parameter relationships to generate associated cartilage geometry. The utility of this approach is illustrated in the nearly instantaneous generation of FE-ready 3D geometric shape representations of the cartilage from bone without the need for MR imaging. The approach serves to make CT imaging and dynamic stereo-radiographic more attractive options considering the improved bone appearance in CTs and advances in predicting bone shape from stereo-radiographic images with SSMs identical to the one used here.

7.3. Methods

An SSM of the knee bone and articular cartilage was developed from MR images of 50 subjects. The subjects included 25 males and 25 females, whose average age was 64 years (range: 44 to 87), average weight was 73 kg (range: 43 to 127), and average body mass index (BMI) was 25.2 (range: 19.0 to 41.3). Subject geometries were from experimental cadaveric testing and from data courtesy of the Osteoarthritis Initiative (OAI), which is available for public access at <http://www.oai.ucsf.edu/>. The OAI datasets are from O.E.1, which consists of baseline (initial healthy) scans. Subjects were included if they were deemed healthy and normal with no signs of osteoarthritis. Bone and cartilage for the femur, tibia, and patella were manually segmented for each subject

using ScanIP (Simpleware, Exeter, UK). The bones were registered to template meshes using an iterative closest point (ICP) algorithm with rigid-body, scaling, and freeform transformations (Rao et al., 2013). The bone template meshes contained 2384, 1101 and 472 nodes for the femur, tibia and patella, respectively (Figure 7.1). Triangular elements with approximate edge lengths of 3 mm described the surface of the bones. Each template bone was also defined in an anatomically derived local coordinate system (CS) (Rao et al., 2013). This technique dually ensured correspondence between bony features across all 50 subjects and aligned each subject to a consistent anatomical CS for efficient evaluation of shape and joint alignment variability. The cartilage template meshes contained 3968, 2736, and 780 nodes for the femur, tibia and patella, respectively (Baldwin et al., 2010). To enable accurate contact evaluations in finite element (FE) modeling, each structure was represented with hexahedral elements. A subset of the surface nodes were also designated as handles on the template mesh to facilitate the mesh-morphing process in Hyperworks (Altair, Troy, MI).

A custom Matlab (Mathworks, Natick, MA) algorithm based on similar work by Fitzpatrick et al. (2011) was developed to uniformly distribute 2030, 504 and 390 handles on the surface of each subject's segmented femoral, tibial, and patellar cartilages, respectively. A graphical user interface (GUI) provided coronal and transverse views of the 3D stereolithography (STL) segmented geometry in for landmark point selection. Seven landmark points on the femoral cartilage were selected on the cartilage edges above the posterior condyles, corner points on the anterior aspect of the medial and lateral condyles, the intercondylar notch, and distal points on each condyle (Figure 7.2).

Two mediolateral landmark points on each of the tibial cartilages and patellar cartilage defined the primary axis along which the algorithm mathematically distributed vertical sets of handles on the attachment and articular surfaces of the cartilage volumes. The algorithm divided the STL meshes into subsections based on these landmark points and distributed handles evenly across the dividing lines. Uniform handle placement is an important component of both correspondence between subjects and the generation of well-formed hexahedral elements for use in FE analyses. Morphing of the template cartilage mesh to a subject-specific shape was achieved by repositioning the template mesh handles to the subject's corresponding handle coordinates. Surrounding internal and surface nodes were linearly interpolated between adjacent handles to morph and smooth the hex mesh into the subject-specific geometry (Baldwin et al., 2010). Cartilage structures were described in the coordinate system of the associated bone. Inter-rater variability in cartilage registration using the GUI was evaluated between three raters. Each rater was familiar with the anatomy of knee articular cartilage and given basic GUI instructions. Error was quantified by the average 3D geometric distance between corresponding surface handles.

The SSM was developed by applying PCA to the 3D coordinates of 3,957 bone nodes and 2,924 cartilage handles, which represent the nodes on both the bone cartilage interface and articular surface. PCA is a data dimensionality reduction technique that describes the raw data by a linear set of orthogonal bases (eigenvectors) and principal component (PC) scores that are organized in descending order of variability, or eigenvalues. In PCA, the largest eigenvalue indicates the greatest variance along the

associated eigenvector and thus, the first PC contains the most significant structure within the dataset. Nodal and handle correspondence across all 50 aligned subjects allows the PCA technique to describe the variability in shape of the structures. The cartilage surface handles were used to develop the SSM because they efficiently described the shape of the cartilage.

Reconstruction and leave-one-out evaluations were first performed separately on the bones and cartilage to assess the ability of the SSM to accurately characterize new subjects in the lower dimensional principal component space. A reconstruction test evaluates the ability of an SSM to assign PC scores to each of the subjects in the training set. This method is useful to evaluate the amount of variability described by each principal component; when all principal components are used, the resulting PC scores should exactly describe the subjects and thus 3D geometric error should be zero. In a leave-one-out evaluation, each subject is left out one at a time while the others are used in the training set for the new SSM; the left-out subject is then considered a “new” or unknown subject and described by the new SSM as a set of PC scores. Some amount of variability in a “new” subject is likely to be indescribable given that the model was not trained on its geometry. By performing leave-one-out tests separately on bone and cartilage, the variability in each structure was independently quantified to assess their particular effectiveness in a predictive application.

A predictive leave-one-out evaluation assessed the ability of the combined bone-cartilage SSM to predict the shape of cartilage from a “new” bone geometry outside of the training set. The predictive approach described in Fitzpatrick et al. was employed in

this study (Fitzpatrick et al., 2011); inputs were bone shape variables and outputs were cartilage shape variables. An initial bone-only SSM was constructed to define PC scores, eigenvalues and eigenvectors for the training set. Characterization (PC scoring) of the left-out subject was achieved by subtracting the mean SSM shape vector, $\bar{v}_{\text{bone-SSM}}$, from the new subject vector, $v_{\text{bone-raw}}$, and multiplying the centered data, $v_{\text{bone-new}}$, by the SSM eigenvectors, E_{bone} , to project the subject's bones into Principal Component space.

$$v_{\text{bone-new}} = v_{\text{bone-raw}} - \bar{v}_{\text{bone-SSM}} \quad (7.1)$$

$$P_{\text{bone-new}} = v_{\text{bone-new}}' * E_{\text{bone}} = (1 \times n_{\text{bone}}) * (n_{\text{bone}} \times N-1) = (1 \times N-1) \quad (7.2)$$

A combined bone-cartilage SSM was built to describe the relationships between bone and cartilage shape. PC scores associated with the bone, P_{bone} , were calculated from the new SSM by multiplying the bone shape vectors, v_{bone} , and the bone portion of the combined eigenvectors, $E_{\text{combined-bone}}$. The linear relationship vector, m , quantified the effect of the input PC scores on the combined PC scores, P_{combined} . Multiplying m and $P_{\text{bone-new}}$ converted the left-out bone scores, $P_{\text{bone-new}}$, to scores suitable for describing the new subject's full geometry including cartilage. Together with the full eigenvector matrix, these new PC scores were used to reconstruct the bone and cartilage shape for the new subject in their original coordinate system.

$$\{P_{\text{bone-mod}}\}_i = m_i * \{P_{\text{bone-new}}\}_i \quad i = 1 \text{ to number of PCs} \quad (7.3)$$

$$v_{\text{new}}' = \{v_{\text{bone-new}} \ v_{\text{cartilage-new}}\}' = P_{\text{bone-mod}} * E' = (1 \times N-1) * (N-1 \times n) = (1 \times n) \quad (7.4)$$

Correlations between the SSM's input (bone) and overall (bone-cartilage) PC scores were calculated to quantify the strength of the input-combined relationship and

thus assess the ability of the input measures to describe the shape model. The strength of output-combined relationships was evaluated in the same way. A successful prediction of the left-out subject's output measures from input measures is dependent upon the strength of these relationships within the SSM. 3D geometric error between corresponding points was calculated to assess the accuracy of SSM-based cartilage predictions. Cartilage thickness differences were also assessed in an effort to understand whether or not the error distribution was random.

7.4. Results

Both the bone-only and bone-cartilage SSMs reduced several thousand coordinate variables into nominally 50 principal components, which describe independent modes of variation. Mode 1 in the bone SSM described 56.5% of the geometric variability and was strongly correlated to scaling measures such as surface area in patellar bone ($r = -0.86$) (Figure 7.3). Similarly, mode 1 described 27.2% of the variability in the cartilage SSM and was highly correlated to patellar cartilage surface area ($r = -0.84$). This finding supports the expectation that both structures are primarily described by scale. Mode 2 described sulcus angle variability ($r = 0.59$ in bone, $r = 0.52$ in cartilage). Visually, Mode 3 described cartilage coverage variability on both the femur and patella. Average thickness in the femur, tibia, and patellar cartilages were 2.62 mm, 2.18 mm, and 2.88 mm, respectively; average surface area was 5327.1 mm², 1177.4 mm², and 1904.3 mm², respectively.

Reconstruction tests confirmed that the members of the training set could be perfectly characterized by the model by projecting to and from principal component

space without any loss of information. Separate leave-one-out tests on the bone and cartilage SSMs assessed their ability to accurately characterize new subject bones and cartilages, respectively. Using all 48 PCs, average 3D geometric errors in the bone SSM were 0.50 ± 0.42 mm (mean \pm std. dev.), 0.57 ± 0.50 mm, and 0.49 ± 0.40 mm for the femur, tibia, and patella, respectively. By comparison, average 3D geometric errors in the cartilage SSM were 0.70 ± 0.56 mm, 0.85 ± 0.73 mm, and 0.65 ± 0.49 mm for the femur, tibia, and patella, respectively, and thickness error were 0.48 ± 0.12 mm, 0.43 ± 0.11 mm, and 0.52 ± 0.12 mm, respectively.

The combined bone-cartilage SSM evaluated the relationships between the two structures. Shape variation in bone and cartilage was therefore described by a single set of principal components. Accounting for a combined 61.7% of the overall variability, the first 3 modes described 40.3%, 14.8%, and 6.6% of the variability, respectively. Overall, 9 and 33 modes cumulatively described 75% and 95% of the variability in the training set, respectively. As one would expect the first and second modes of variation were correlated with scaling and sulcus groove measures that were correlated in the structure-specific SSMs described earlier. Notably, the combined SSM now provides a single set of PC scores that describe variability within and between both bone and cartilage.

Using all PCs in the reconstruction test, 3D geometric error between actual and predicted structures was zero, thus the reconstruction test successfully rebuilt the bone and cartilage of each subject in the training set given the subject's bone and cartilage. In the leave-one-out test, only the bone was given to the model and the predictive algorithm described earlier was employed to estimate cartilage shape. Since correlations to the

overall PC scores are calculated separately for the input and output PCs (Figure 7.4), prediction accuracy is dependent upon the combined strength of these correlations for each PC. The first input and output correlations are high; indicating that scaling is strongly related between the two structures. In contrast, the third input correlation is very low, indicating that Mode 3 describes little bone shape variation. 3D geometric error in the bone was 0.57 ± 0.47 mm, 0.64 ± 0.56 mm, and 0.59 ± 0.46 mm in the femur, tibia, and patella, respectively (Figure 7.5). Average cartilage 3D geometric error was 1.17 ± 0.88 mm, 1.85 ± 1.40 mm, and 1.09 ± 0.72 mm, respectively. Average thickness errors were 0.51 ± 0.12 mm, 0.40 ± 0.11 mm, and 0.51 ± 0.13 mm, respectively. By comparison, these errors are similar to those calculated in the separate bone and cartilage evaluations. Bounds on the predictions were determined by perturbing weakly correlated principal component scores and assessing the resulting geometric variability. The 3rd principal component, which is substantially weaker in its relationship to the bone but accounts for almost 7% of the overall variability, was perturbed by ± 1 standard deviation of that mode. The perturbation resulted in a difference of up to ± 2 mm at the cartilage edges. Inter-rater variability in the cartilage registration process was 0.25 mm for average 3D geometric distance between corresponding handles, which resulted in 0.1 mm average thickness variation between corresponding handles of each rater's registered geometries.

7.5. Discussion

The purpose of this study was to assess the relationship between bone and cartilage shape and the predictive capability of bone geometry for the distribution and

thickness of articular cartilage. A statistical shape model of bone and articular cartilage in the knee joint was used in leave-one-out type of evaluation to predict subject-specific cartilage from bony anatomy. A complete representation of bone and cartilage provides several benefits; the PC modes described a holistic relationship between anatomy of the bone and cartilage for the femur, tibia, and patella without requiring a priori identification of specific shape measures; an efficient mesh-morphing process allowed seamless integration with finite element modeling techniques; and enables efficient development of new virtual geometries for use in population-based studies.

Accuracy of left-out bone and cartilage predictions were evaluated by 3D geometric and thickness differences from its actual shape vector. Cartilage and bone scaled well together, which is likely a result of the strong correlation of both structures to the first mode of variation. Other studies have made similar connections between size of the joint and cartilage coverage; statistically significant gender differences were found in cartilage volume due to the larger male joint surface (Faber et al., 2001). All of the geometric error in the bone can be traced back to the bone-only SSM's ability to score new subjects. By comparison, the difference between cartilage predictions by the combined SSM and cartilage-only SSM was less than 1.0 mm. Thickness errors between the cartilage-only and combined SSM leave-one-out tests were virtually the same. Therefore, a large portion of the cartilage error can be ascribed to the consistency of cartilage coverage, particularly at the cartilage boundaries. The remaining error may be explained by the strength of the relationship between the shape of bone and cartilage, which is strongest in the first and second modes of variation (Figure 7.4). Bounds on the

predictions of up to ± 2 mm illustrate the challenges in imaging and segmenting thin cartilage boundaries. The weak relationship between bone shape and the 3rd mode of variation presents a challenge in predicting its appropriate PC score. However, since the majority of contact in activities and mechanics-based evaluations occurs away from these regions, their accuracy is unlikely to impact contact mechanics or implant selection and placement.

Few other studies have evaluated the predictive capability of whole structures to estimate size and shape of adjacent structures. Yang et al. applied a nonlinear iterative partial least squares (NIPALS) regression approach in the shoulder joint to predict adjacent bones from each other (Yang et al., 2008). Given the scapular bone as the predictor, average RMS error between the actual and predicted humeri was 2.63 ± 0.91 mm. When the humerus was the predictor, average scapular RMS error was 5.66 ± 1.48 mm. Given the differences in structures from the current study, it is difficult to make a direct comparison to the current study, however the NIPALS approach was also evaluated in this work and performance was comparable to the predictive PCA approach.

Alternative automated methods for capturing cartilage shape require the use of MR scans to guide a statistical model. Fripp et al. proposed a method for development of a 3D active shape model that includes bone, a probability map of the bone-cartilage interface, and a cartilage thickness map to be used on MR images with a specific imaging sequence (Fripp et al., 2007). The resulting cartilage segmentation matched with manually segmented cartilage structures to within 0.25 mm; however, the structures would require further processing for use in computational contact analyses. Baldwin et

al. linked MR images with a statistical shape model of knee articular cartilage that efficiently morphed a template hexahedral FE model to a subject-specific shape with limited user interaction (Baldwin et al., 2010). Efficiencies with statistical models and FE analyses are important in population-based analyses where model-processing time makes large sample sizes cumbersome. SSMs have already been used to evaluate relative differences in contact mechanics between modes of variation (Rao et al., 2013).

SSM-based evaluations of disease states such as OA have demonstrated their potential to act as a classifier and predictor. Neogi et al. performed an MR-based study that detected the onset of OA (Neogi et al., 2013). Active appearance models of the bones were created for healthy and pathologic knees and linear discriminant analysis identified vectors to discriminate between the two groups. Results indicated that 3D bone shape increased the likelihood of developing OA by 3X. Furthermore, studies have shown statistically significant differences between OA and healthy cartilage (Folkesson et al., 2007). Thus, the current workflow could exploit PCA as a classifier on a larger training set of healthy and pathologic subjects to further investigate the etiology of OA.

Morphology of knee articular cartilage is also affected by other factors that have not been considered in this study. Cartilage thickness increased by 20-50% in regions of contact in normal knees (Li et al., 2005) and while contact area may be estimated by bone shape, joint alignment was not considered in this study. Hudelmaier et al. reported an age-dependent positive correlation between muscle cross sectional area and cartilage volume ($r = 0.66$) and thickness ($r = 0.44$) (Hudelmaier et al., 2003). Loading conditions also been reported to have an effect on cartilage thickness. Eckstein et al. reported as

much as 0.26 mm in thickness variability due to activity (Eckstein et al. 2000), which can take several hours to recover. Inactivity also contributes to cartilage loss; Hinterwimmer et al. reported tibial cartilage thickness atrophy over a 7 week period of $6.6 \pm 4.9\%$, or 0.1-0.2 mm given the average tibial cartilage thickness reported in the current study (Hinterwimmer et al., 2004). As a likely more relevant time-based factor, Waterton et al. reported diurnal variation in femoral cartilage thickness of up to 0.6 mm in the loaded regions of the patellofemoral compartment and both tibiofemoral compartments (Waterton et al., 2000). This finding in particular suggests that a stronger relationship may be formed between bone and cartilage morphology if these factors are controlled for or included in predictive models. Doing so, however, makes the development of a large training set very difficult. Instead factors such as segmentation error, which can be as much as 0.5 mm in thickness (Koo et al., 2005) and registration error, reported here, may be easier to control and result in valuable prediction improvements.

Cartilage prediction may benefit TKR surgery and *in vivo* stereo-radiographic studies where radiographs and CTs are part of the current workflow. To date, this is the first study to reconstruct articular cartilage from the shape of the associated bone and without guidance from MR images. As patient-specific cutting blocks become more common in TKR surgeries, manufacturers and surgeons may benefit from an accurate prediction of cartilage thickness to inform cutting block design and surgical alignment in an effort to restore the natural joint line (Burdulis et al., 2006). *In vivo* studies with stereo-radiography, or fluoroscopy, are also becoming more common; the technique provides real-time information on the motion of bones, implants and other radiopaque

structures. This technique is adequate for the extraction of joints kinematics; however, since the articulating cartilage is not radiopaque, it must be modeled via the traditional MR segmentation technique if contact mechanics are of interest. 3D-2D registration techniques are used to align 3D bone or implant geometries with their corresponding 2D silhouettes on x-ray image sequences to calculate *in vivo* kinematics and contact mechanics in TKR (Li et al., 2008; Yamaguchi et al., 2011) and healthy natural knees (Li et al., 2005; Fernandez et al., 2008). Furthermore, studies have illustrated the ability of SSMs to dually reconstruct and track 3D bone geometry from fluoroscopic sequences (Baka et al., 2011, 2012 and 2014). The SSMs used by Baka et al. to reconstruct the bone are similar to the current study's SSM, thus the workflow presented here could potentially use bone predicted from fluoroscopic sequences to generate the corresponding cartilage structures.

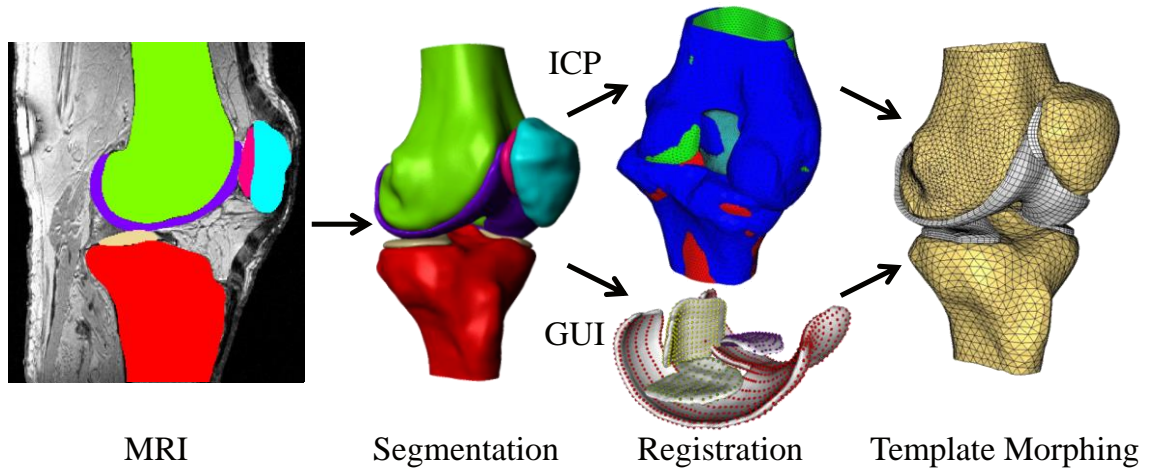


Figure 7.1 Development of a statistical shape model of the knee: Scans of an MRI were segmented to generate a 3D stereolithography (STL) model of the bone and cartilage. Bone was registered to a template using an Iterative Closest Point (ICP) algorithm while cartilage, being a thinner structure, required a custom developed algorithm and GUI to register the STL geometry. A template developed for a median-sized subject was then morphed for each training set member to establish correspondence between like structures.

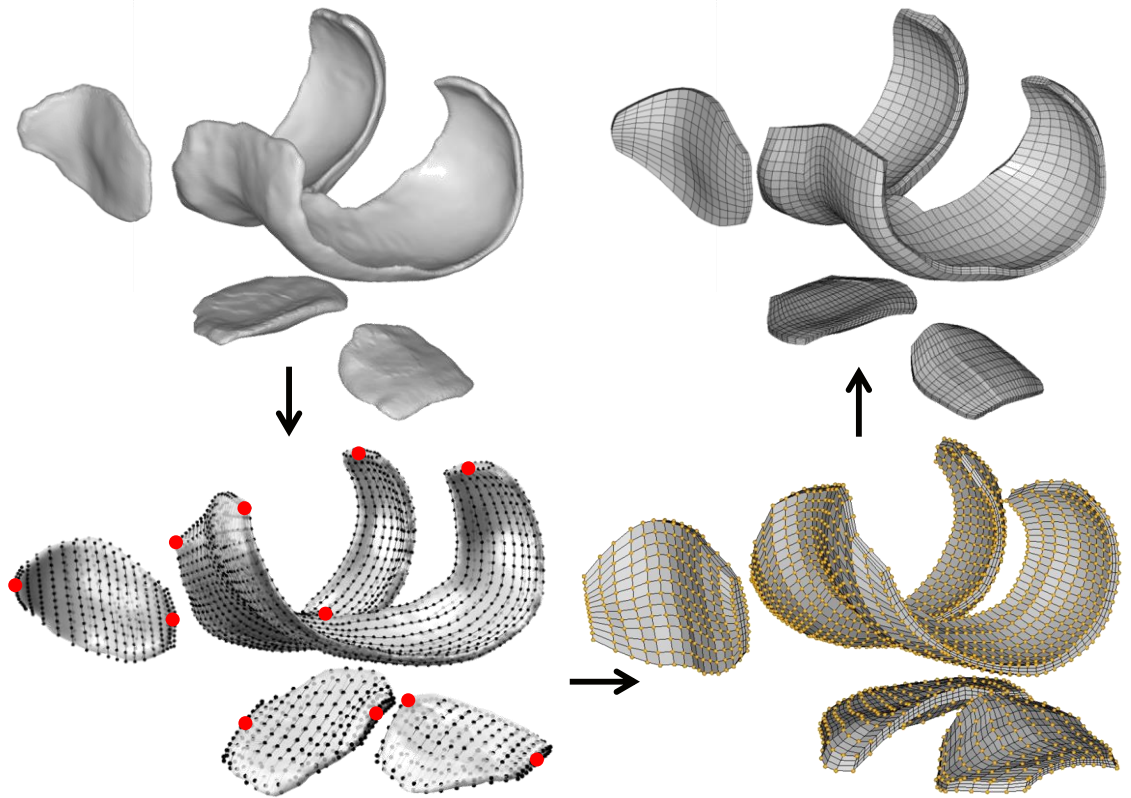


Figure 7.2 The segmented geometry is loaded into the Matlab® graphical user interface (top left), landmark points (red) are manually selected to guide the automatic distribution of handles (black) onto the subject's surface (bottom left). This dually establishes correspondence to the training set and the template hexahedral mesh (bottom right). A mesh-morphing algorithm deforms the template hexahedral mesh to the subject's segmented shape to generate an FE-ready cartilage representation (top right).

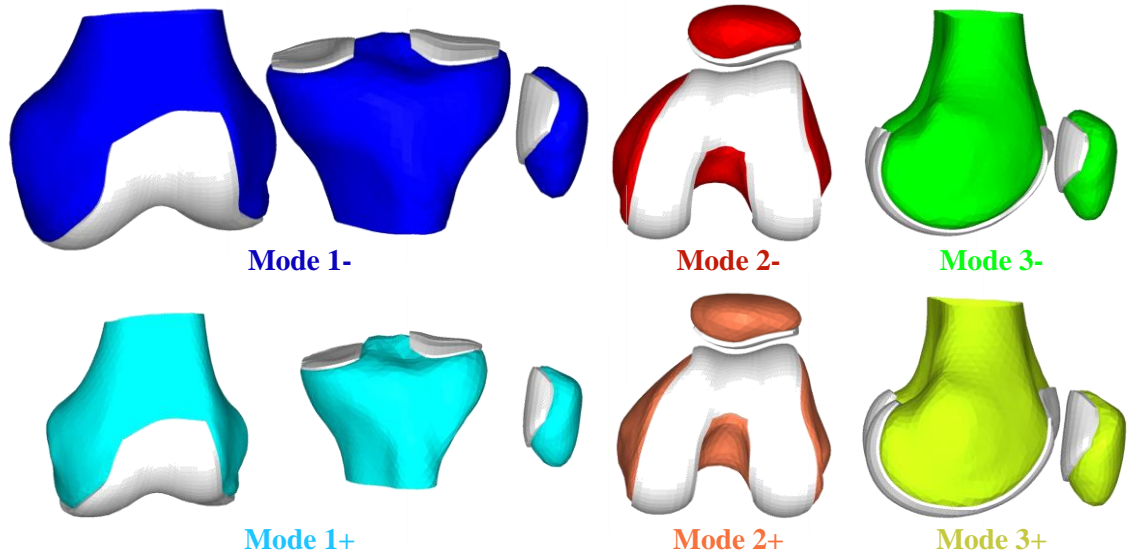


Figure 7.3 Representations of the bones and cartilage for first three principal component modes from the combined bone-cartilage model. Knees are shown at ± 1.5 standard deviations and bones are aligned to their local coordinate systems. Alignments are for relative comparison between mode perturbations.

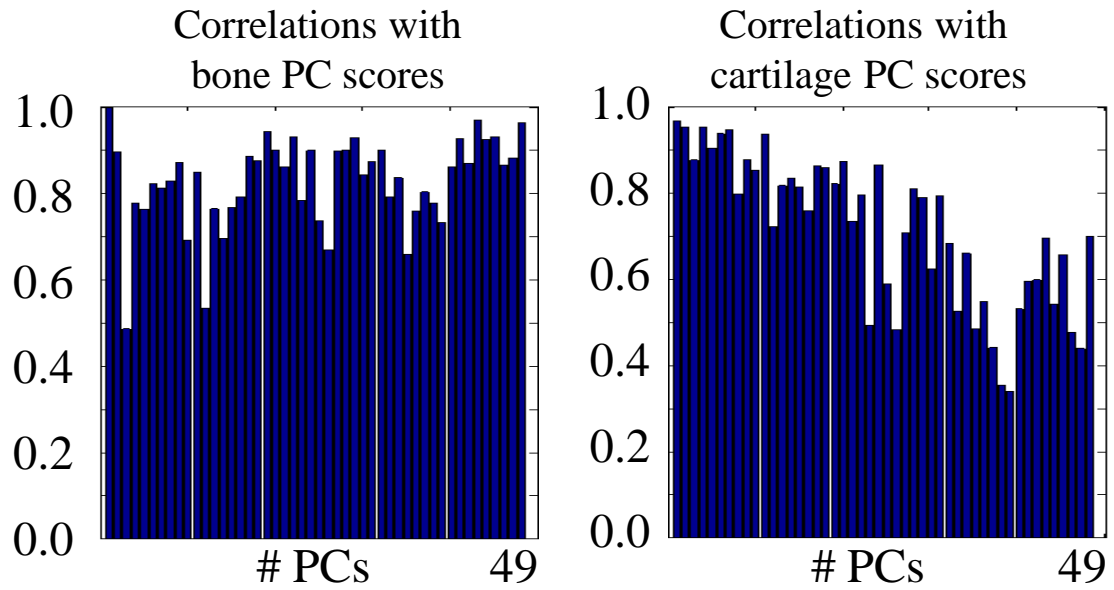


Figure 7.4 Correlations within the combined bone-cartilage SSM. Overall PC scores were correlated to bone-only PC scores (left) and cartilage-only PC scores (right). PCs with high correlations in both figures indicate that the shape described by those modes have strong predictive potential.

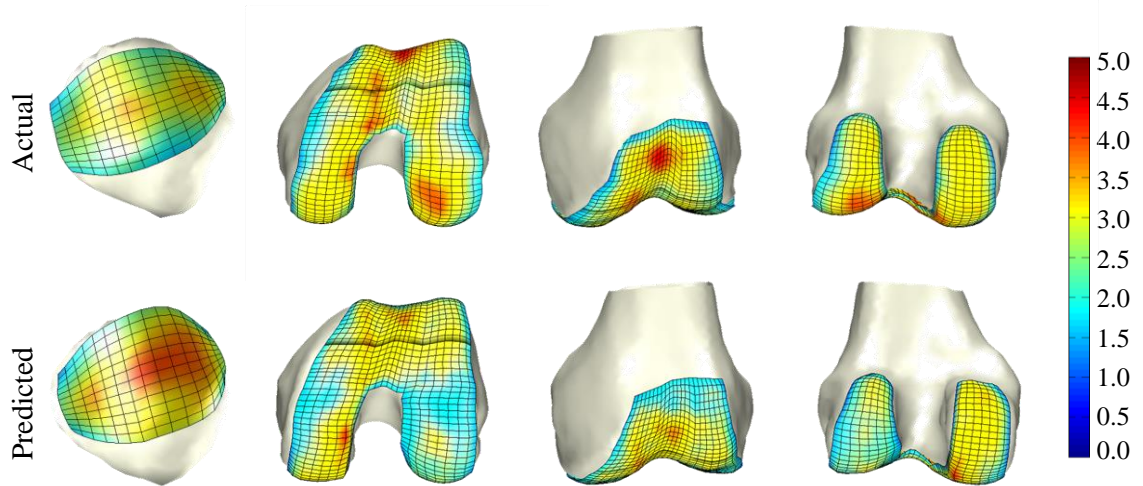


Figure 7.5 Comparison of actual and predicted cartilage distribution and thickness for the femur and patella. The patella has been enlarged for the visualization purposes. Thickness is represented by the color contour on the actual and predicted cartilage surface. Units are in millimeters.

CHAPTER 8. CONCLUSIONS AND RECOMMENDATIONS

The purpose of this dissertation was to develop statistical modeling tools to account for variability in natural knee joint morphology and function. The tools are meant to improve the efficiency of computational biomechanics evaluations. Models were developed using principal component analysis (PCA), which served to efficiently characterize the population by describing the data with a reduced number of variables. The benefit of this was observed by the resulting groups of interrelated characteristics including holistic shape features, linear anatomical measures, and kinematics of the tibiofemoral (TF) and patellofemoral (PF) joints.

Specific contributions of this research were dually in applications and outcomes of the statistical modeling approaches. Statistical shape models (SSMs) had so far described morphological variability for applications such as TKR component sizing and static joint alignment variability. Chapter 4 combined whole joint shape and 6 degree-of-freedom (DOF) kinematics for a more complete evaluation of the knee. The efficiency of this approach was illustrated by its ability to describe clinically relevant shape-function relationships reported across numerous existing studies. Assessment of the whole 3D shape in Chapter 4 provided the necessary insight to inform potentially valuable 2D measures further evaluated in Chapter 5. A measures-function model was built in Chapter 5 to more directly assess relationships between clinically relevant 2D linear

measures and motion of a controlled PF joint model. Correlations were strong enough to make subject-specific kinematic predictions, suggesting that the extracted 2D measures may be useful metrics for establishing norms. The methods in Chapters 4 and 5 could potentially be applied to pathologic groups to inform clinicians and researchers as to the predisposing factors influencing unnatural joint motion.

Efficient development of natural bone geometries from SSMs and radiographs reduce the need for MR and CT scanning and improve the efficiency of *in vivo* analyses. Chapter 6 presented an algorithm to reconstruct the 3D shape of the patellar bone from radiographs, which directly contributes to those same improvements. However, efficient prediction of natural bony geometry has limited utility in finite element (FE) analyses of contact mechanics as cartilage prediction is not part of the workflow. Previous works developed SSM-based tools to improve segmentation efficiency, however this required MR scans and subsequent processing to align and mesh the STL geometries for use in an FE model. Chapter 7 introduced a novel approach to cartilage estimation that did not require MR scans and has the potential to be integrated into other existing tools for a whole joint prediction from radiographs. The same SSM that is used to predict subject-specific bone shapes could potentially be used to inform the associated cartilage shape.

Tools such as the cartilage registration and ligament wrapping algorithms contribute to the efficient development of natural knee models suitable for population-based studies. Efficient soft-tissue generation was first discussed as a direct contribution to the research motivating this dissertation (Baldwin, 2009). Adaptation of these tools to Matlab scripting from similar versions in Hyperworks (Altair, Troy, MI) and The

Visualization Toolkit (VTK) has made them more user-friendly and efficient as statistical modeling techniques become more automated. Further value could be added to these tools by eliminating the remaining manual steps such as selecting several landmark points on the cartilage structures to seed the automatic distribution of surface handles. Furthermore, not all soft-tissues of the knee are currently generated by the morphing algorithm; additional structures such as the popliteofibular ligament (PFL) and the popliteus muscle could be added if their origin and insertion sites were known or predictable.

In summary, the research topics presented in this dissertation contribute to the growing body of knowledge on statistical shape modeling and its application to the natural knee joint. Future studies should make use of the efficient generation of computational models for population-based FE evaluations of cartilage contact and soft-tissue laxity under physiological loading conditions and controlled shape variability.

LIST OF REFERENCES

- ABAQUS, 2013. ABAQUS Analysis User's Manual. Simulia, Providence, RI. (Version 6.13-1).
- Ackland, D.C., Keynejad, F., Pandy, M.G., 2011. Future trends in the use of X-ray fluoroscopy for the measurement and modelling of joint motion. *Proceedings of the Institution of Mechanical Engineers, Part H: Journal of Engineering in Medicine*. 225 (12):1136-1148.
- Ali, A.A., Clary, C.W., Smoger, L.S., Fitzpatrick, C.K., Rullkoetter, P.J., Laz, P.J., 2015. Efficient Computational Framework for Population-Based Evaluation of TKR-Implanted Joint Mechanics. *Journal of Orthopaedic Research: Official Publication of the Orthopaedic Research Society*. Paper #868.
- Amis, A.A., Senavongse, W., Bull, A.M., 2006. Patellofemoral kinematics during knee flexion-extension: An in vitro study. *Journal of Orthopedic Research*. 24 (12):2201-2211.
- Andriacchi, T.P., Briant, P.L., Bevill, S.L., Koo, S., 2006. Rotational changes at the knee after ACL injury cause cartilage thinning. *Clinical Orthopaedics and Related Research*. 442:39-44.
- Andriacchi, T.P., Koo, S., Scanlan, S.F., 2009. Gait Mechanics Influence Healthy Cartilage Morphology and Osteoarthritis of the Knee. *Journal of Bone and Joint Surgery*. 91 (Supplement 1):95-101.
- Andriacchi, T.P., Mundermann, A., 2006. The role of ambulatory mechanics in the initiation and progression of knee osteoarthritis. *Current Opinion in Rheumatology*. 18 (5):514-518.
- Andriacchi, T.P., Mundermann, A., Smith, R.L., Alexander, E.J., Dyrby, C.O., Koo, S., 2004. A framework for the in vivo pathomechanics of osteoarthritis at the knee. *Annals Biomedical Engineering*. 32 (3):447-457.
- Argenson, J.N., Scuderi, G.R., Komistek, R.D., Scott, W.N., Kelly, M.A., Aubaniac, J.M., 2005. In vivo kinematic evaluation and design considerations related to high flexion in total knee arthroplasty. *Journal of Biomechanics*. 38 (2):277-284.
- Baka, N., de Bruijne, M., van Walsum, T., Kaptein, B.L., Giphart, J.E., Schaap, M., Niessen, W.J., Lelieveldt, B.P.F., 2012. Statistical Shape Model-Based Femur Kinematics from Biplane Fluoroscopy. *IEEE Transactions on Medical Imaging*. 31 (8):1573-1583.
- Baka, N., Kaptein, B. L., de Bruijne, M., van Walsum, T., Giphart, J. E., Niessen, W. J., Lelieveldt, B. P. F., 2011. 2D-3D shape reconstruction of the distal femur from stereo X-ray imaging using statistical shape models. *Medical Image Analysis* 15 (6):840-850.

- Baka, N., Kaptein, B.L., Giphart, J.E., Staring, M., de Bruijne, M., Lelieveldt, B.P.F., Valstar, E., 2014. Evaluation of automated statistical shape model based knee kinematics from biplane fluoroscopy. *Journal of Biomechanics*. 47 (1):122-129.
- Baldwin, M.A. "Explicit Finite Element Modeling of Knee Mechanics During Simulated Dynamic Activities." Diss. University of Denver, June 2009. Print.
- Baldwin, M.A., Clary, C., Maletsky, L.P., Rullkoetter, P.J., 2009. Verification of predicted specimen-specific natural and implanted patellofemoral kinematics during simulated deep knee bend. *Journal of Biomechanics*. 42 (14):2341-2348.
- Baldwin, M.A., Clary, C.W., Fitzpatrick, C.K., Deacy, J.S., Maletsky, L.P., 2012. Dynamic finite element simulation for evaluation of knee replacement mechanics. *Journal of Biomechanics*. 45 (3):474-483.
- Baldwin, M.A., Langenderfer, J.E., Rullkoetter, P.J., Laz, P.J., 2010. Development of subject-specific and statistical shape models of the knee using an efficient segmentation and mesh morphing approach. *Computer Methods and Programs in Biomedicine*. 97 (3):232-240.
- Banks, S., Bellemans, J., Nozaki, H., Whiteside, L.A., Harman, M., Hodge, W.A., 2003. Knee motions during maximum flexion in fixed and mobile-bearing arthroplasties. *Clinical Orthopaedics and Related Research*. 410:131-138.
- Barratt, D.C., Chan, C.S., Edwards, P.J., Penney, G.P., Slomczykowski, M., Carter, T.J. and Hawkes, D.J., 2008. Instantiation and registration of statistical shape models of the femur and pelvis using 3D ultrasound imaging. *Medical image analysis*, 12(3), pp.358-374.
- Behiels, G., Maes, F., Vandermeulen, D., Suetens, P., 2002. Evaluation of image features and search strategies for segmentation of bone structures in radiographs using active shape models. *Medical Image Analysis* 6 (1):47-62.
- Bey, M.J., Kline, S.K., Tashman, S., Zael, R., 2008. Accuracy of biplane x-ray imaging combined with model-based tracking for measuring in-vivo patellofemoral joint motion. *Journal of Orthopaedic Surgery and Research*. 3:38.
- Bingham, J.T., Li, G., 2006. An Optimized Image Matching Method for Determining In-vivo TKA Kinematics with a Dual-Orthogonal Fluoroscopic Imaging System. *Journal of Biomechanics Engineering*. 128 (4):588-595.
- Biswas, D., Bible, J.E., Bohan, M., Simpson, A.K., Whang, P.G., Grauer, J.N., 2009. Radiation Exposure from Musculoskeletal Computerized Tomographic Scans. *Journal of Bone and Joint Surgery*. 91 (8):1882-1889.

- Boling, M., Padua, D., Marshall, S., 2010. Gender differences in the incidence and prevalence of patellofemoral pain syndrome. *Scandinavian Journal of Medicine and Science in Sports*. 20 (5):725-30.
- Brage, M.E., Draganich, L.F., Pottenger, L.A. and Curran, J.J., 1994. Knee laxity in symptomatic osteoarthritis. *Clinical orthopaedics and related research*, 304, pp.184-189.
- Brainerd, E.L., Baier, D.B., Gatesy, S.M., Hedrick, T.L., Metzger, K.A., Gilbert, S.L., Crisco, J.J., 2010. X-ray reconstruction of moving morphology (XROMM): precision, accuracy and applications in comparative biomechanics research. *Journal of Experimental Zoology Part A: Ecological Genetics and Physiology*. 313A (5): 262-279.
- Bredbenner, T.L., Eliason, T.D., Potter, R.S., Mason, R.L., Havill, L.M., Nicoletta, D., 2010. Statistical shape modelling describes variation in tibia and femur surface geometry between Control and Incidence groups from the osteoarthritis initiative database. *Journal of Biomechanics*. 43 (9):1780-1786.
- Bryan, R., Mohan, P.S., Hopkins, A., Galloway, F., Taylor, M., Nair, P.B., 2010. Statistical modeling of the whole human femur incorporating geometric and material properties. *Medical Engineering and Physics*. 32 (1):57-65.
- Bryan, R., Nair, P.B., Taylor, M., 2009. Use of a statistical model of the whole femur in a large scale, multi-model study of femoral neck fracture risk. *Journal of Biomechanics*. 42 (13):2171-2176.
- Bryan, R., Nair, P.B. Taylor, M., 2012. Influence of femur size and morphology on load transfer in the resurfaced femoral head: A large scale, multi-subject finite element study. *Journal of biomechanics*, 45(11), pp.1952-1958.
- Burdulis, A.G., Fitz, W., Vargas-Vo-Racek, R., 2006. Surgical tools facilitating increased accuracy, speed and simplicity in performing joint arthroplasty. Patent Number WO 2006/060795.
- Canny, J., 1986. A Computational Approach to Edge Detection. *IEEE Transactions On Pattern Analysis And Machine Intelligence*. 8 (6):679-698.
- Carballido-Gamio, J., Bauer, J.S., Stahl, R., Lee, K., Krause, S., Link, T.M., Majumdar, S., 2008. Inter-subject comparison of MRI knee cartilage thickness. *Medical Image Analysis*. 12 (2):120-135.
- Carpenter, R.D., Brilhault, J., Majumdar, S., Ries, M.D., 2009. Magnetic resonance imaging of *in vivo* patellofemoral kinematics after total knee arthroplasty. *The Knee*. 16 (5):332-336.
- Chintalapani, G., Ellingsen, L.M., Sadowsky, O., Prince, J.L. and Taylor, R.H., 2007. Statistical atlases of bone anatomy: construction, iterative improvement and validation. In

- Medical Image Computing and Computer-Assisted Intervention–MICCAI 2007 (pp. 499-506). Springer Berlin Heidelberg.
- Clary, C.W., Fitzpatrick, C.K., Maletsky, L.P., Rullkoetter, P.J., 2013. The influence of total knee arthroplasty geometry on mid-flexion stability: An experimental and finite element study. *Journal of Biomechanics*. 46 (7):1351-1357.
- Cohen, Z.A., McCarthy, D.M., Kwak, D.S., Legrand, P., Fograsi, F., Ciaccio, E.J., Atheshian, G.A., 1999. Knee cartilage topography, thickness, and contact areas from MRI in-vitro calibration and in-vivo measurements. *Osteoarthritis and Cartilage*. 7 (1):95-109.
- Connolly, A., FitzPatrick, D., Moulton, J., Lee, J., Lerner, A., 2008. Tibiofemoral cartilage thickness distribution and its correlation with anthropometric variables. *Proceedings of the Institution of Mechanical Engineers, Part H: Journal of Engineering in Medicine*. 222 (1):29-39.
- Cootes, T.F., Taylor, C.J., Cooper, D.H., Graham J., 1995. Active shape models - their training and application. *Computer Vision and Image Understanding*. 61(1):38-59.
- D’Lima, D.D., Chen, P.C., Kester, M.A., Colwell Jr., C.W., 2003. Impact of patellofemoral design on patellofemoral forces and polyethylene stresses. *The American Journal of Bone Joint Surgery*. 85-A (Suppl. 4):85-93.
- Dai, Y., Bischoff, J.E., 2013. Comprehensive assessment of tibial plateau morphology in total knee arthroplasty: Influence of shape and size on anthropometric variability. *Journal of Orthopaedic Research*. 31 (10):1643-1652.
- Dalury, D.F. and Dennis, D.A., 2003. Extensor mechanism problems following total knee replacement. *The journal of knee surgery*, 16(2), pp.118-122.
- Deluzio, K.J., Wyss, U.P., Zee, B., Costigan, P.A. and Serbie, C., 1997. Principal component models of knee kinematics and kinetics: normal vs. pathological gait patterns. *Human Movement Science*, 16(2), pp.201-217.
- Dennis, D., Komistek, R., Scuderi, G., et al. 2001. In vivo three-dimensional determination of kinematics for subjects with a normal knee or a unicompartamental or total knee replacement. *Journal of Bone and Joint Surgery*. 83-A (Suppl. 2 Pt. 2):104-115.
- Dennis, D.A., Kim, R.H., Johnson, D.R., Springer, B.D., Fehring, T.K. and Sharma, A., 2011. The John Insall Award: control-matched evaluation of painful patellar Crepitus after total knee arthroplasty. *Clinical Orthopaedics and Related Research®*, 469(1), pp.10-17.

- Dennis, D.A., Mahfouz, M.R., Komistek, R.D. and Hoff, W., 2005. In vivo determination of normal and anterior cruciate ligament-deficient knee kinematics. *Journal of Biomechanics*. 38 (2):241-253.
- Eckhoff, D.G., Dwyer, T.F., Bach, J.M., Spitzer, V.M. and Reinig, K.D., 2001. Three-dimensional morphology of the distal part of the femur viewed in virtual reality. *J Bone Joint Surg Am*, 83(2 suppl 1), pp.S43-50.
- Eckstein, F., Lemberger, B., Stammberger, T., Englemeier, K. H., Reiser, M., 2000. Patellar cartilage deformation in vivo after static versus dynamic loading. *Journal of Biomechanics* 33, 819-825.
- Edelsbrunner, H., Kirkpatrick, D.G. and Seidel, R., 1983. On the shape of a set of points in the plane. *Information Theory, IEEE Transactions on*, 29(4), pp.551-559.
- Faber, S.C., Eckstein, F., Lukasz, S., Mühlbauer, R., Hohe, J., Englmeier, K.H. and Reiser, M., 2001. Gender differences in knee joint cartilage thickness, volume and articular surface areas: assessment with quantitative three-dimensional MR imaging. *Skeletal radiology*, 30(3), pp.144-150.
- Farahmand, F., Sejiavongse, W. and Amis, A.A., 1998. Quantitative study of the quadriceps muscles and trochlear groove geometry related to instability of the patellofemoral joint. *Journal of Orthopaedic Research*, 16(1), pp.136-143.
- Farahmand, F., Tahmasbi, M.N. and Amis, A., 2004. The contribution of the medial retinaculum and quadriceps muscles to patellar lateral stability—an in-vitro study. *The knee*, 11(2), pp.89-94.
- Fellows, R.A., Hill, N.A., Gill, H.S., MacIntyre, N.J., Harrison, M.M., Ellis, R.E. and Wilson, D.R., 2005. Magnetic resonance imaging for in vivo assessment of three-dimensional patellar tracking. *Journal of biomechanics*, 38(8), pp.1643-1652.
- Fernandez, J.W., Akbarshahi, M., Kim, H.J. and Pandy, M.G., 2008. Integrating modelling, motion capture and x-ray fluoroscopy to investigate patellofemoral function during dynamic activity. *Computer methods in biomechanics and biomedical engineering*, 11(1), pp.41-53.
- Fitzpatrick, C., FitzPatrick, D., Lee, J. and Auger, D., 2007. Statistical design of unicompartamental tibial implants and comparison with current devices. *The Knee*, 14(2), pp.138-144.
- Fitzpatrick, C.K., Baldwin, M.A., Laz, P.J., FitzPatrick, D.P., Lerner, A.L. and Rullkoetter, P.J., 2011. Development of a statistical shape model of the patellofemoral joint for investigating relationships between shape and function. *Journal of biomechanics*, 44(13), pp.2446-2452.

- Fitzpatrick, C.K., Kim, R.H., Ali, A.A., Smoger, L.M. and Rullkoetter, P.J., 2013. Effects of resection thickness on mechanics of resurfaced patellae. *Journal of biomechanics*, 46(9), pp.1568-1575.
- Fitzpatrick, C.K., Steensen, R.N., Tumuluri, A., Trinh, T., Bentley, J. and Rullkoetter, P.J., 2015. Computational analysis of factors contributing to patellar dislocation. *Journal of Orthopaedic Research*. (in-press)
- Fleute, M. and Lavallée, S., 1998. Building a complete surface model from sparse data using statistical shape models: Application to computer assisted knee surgery. In *Medical Image Computing and Computer-Assisted Intervention—MICCAI'98* (pp. 879-887). Springer Berlin Heidelberg.
- Folkesson, J., Dam, E.B., Olsen, O.F., Pettersen, P.C. and Christiansen, C., 2007. Segmenting articular cartilage automatically using a voxel classification approach. *Medical Imaging, IEEE Transactions on*, 26(1), pp.106-115.
- Freedman, B.R. and Sheehan, F.T., 2013. Predicting three-dimensional patellofemoral kinematics from static imaging-based alignment measures. *Journal of Orthopaedic Research*, 31(3), pp.441-447.
- Freeman, M.A.R. and Pinskerova, V., 2005. The movement of the normal tibio-femoral joint. *Journal of biomechanics*, 38(2), pp.197-208.
- Fregly, B.J., Rahman, H.A. and Banks, S.A., 2005. Theoretical accuracy of model-based shape matching for measuring natural knee kinematics with single-plane fluoroscopy. *Journal of biomechanical engineering*, 127(4), pp.692-699.
- Fripp, J., Crozier, S., Warfield, S.K., Ourselin, S., 2010. Automatic segmentation and quantitative analysis of the articular cartilages from magnetic resonance images of the knee. *IEEE Transactions on Medical Imaging* 29(1), 55-64.
- Fripp, J., Warfield, S.K., Crozier, S. and Ourselin, S., 2006. Automatic segmentation of the knee bones using 3D active shape models. In *Pattern Recognition, 2006. ICPR 2006. 18th International Conference on* (Vol. 1, pp. 167-170). IEEE.
- Fritscher, K., Grünerbl, A., Hänni, M., Suhm, N., Hengg, C. and Schubert, R., 2009. Trabecular bone analysis in CT and X-ray images of the proximal femur for the assessment of local bone quality. *Medical Imaging, IEEE Transactions on*, 28(10), pp.1560-1575.
- Galloway, F., Kahnt, M., Ramm, H., Worsley, P., Zachow, S., Nair, P. and Taylor, M., 2013. A large scale finite element study of a cementless osseointegrated tibial tray. *Journal of biomechanics*, 46(11), pp.1900-1906.

- Galloway, F., Worsley, P., Stokes, M., Nair, P. and Taylor, M., 2012. Development of a statistical model of knee kinetics for applications in pre-clinical testing. *Journal of biomechanics*, 45(1), pp.191-195.
- Gollmer, S.T., Lachner, R. and Buzug, T.M., 2007, August. Registration algorithm for statistical bone shape reconstruction from radiographs-an accuracy study. In *Engineering in Medicine and Biology Society, 2007. EMBS 2007. 29th Annual International Conference of the IEEE* (pp. 6375-6378). IEEE.
- Grood, E.S. and Suntay, W.J., 1983. A joint coordinate system for the clinical description of three-dimensional motions: application to the knee. *Journal of biomechanical engineering*, 105(2), pp.136-144.
- Guo, C., Cheng, Y., Guo, H., Wang, J., Wang, Y. and Tamura, S., 2015. Surface-based rigid registration using a global optimization algorithm for assessment of MRI knee cartilage thickness changes. *Biomedical Signal Processing and Control*, 18, pp.303-316.
- Halloran, J.P., Petrella, A.J. and Rullkoetter, P.J., 2005. Explicit finite element modeling of total knee replacement mechanics. *Journal of biomechanics*, 38(2), pp.323-331.
- Hamai, S., Moro-oka, T.A., Miura, H., Shimoto, T., Higaki, H., Fregly, B.J., Iwamoto, Y. and Banks, S.A., 2009. Knee kinematics in medial osteoarthritis during in vivo weight-bearing activities. *Journal of Orthopaedic Research*, 27(12), pp.1555-1561.
- Hanson, G.R., Suggs, J.F., Freiberg, A.A., Durbhakula, S. and Li, G., 2006. Investigation of in vivo 6DOF total knee arthroplasty kinematics using a dual orthogonal fluoroscopic system. *Journal of orthopaedic research*, 24(5), pp.974-981.
- Harbaugh, C.M., Wilson, N.A. and Sheehan, F.T., 2010. Correlating femoral shape with patellar kinematics in patients with patellofemoral pain. *Journal of Orthopaedic Research*, 28(7), pp.865-872.
- Harris, M.D., Anderson, A.E., Henak, C.R., Ellis, B.J., Peters, C.L. and Weiss, J.A., 2012. Finite element prediction of cartilage contact stresses in normal human hips. *Journal of Orthopaedic Research*, 30(7), pp.1133-1139.
- Hill, P.F., Vedi, V., Williams, A., Iwaki, H., Pinskerova, V. and Freeman, M.A.R., 2000. Tibiofemoral movement 2: the loaded and unloaded living knee studied by MRI. *Journal of Bone & Joint Surgery, British Volume*, 82(8), pp.1196-1198.
- Hinterwimmer, S., Krammer, M., Krötz, M., Glaser, C., Baumgart, R., Reiser, M. and Eckstein, F., 2004. Cartilage atrophy in the knees of patients after seven weeks of partial load bearing. *Arthritis & Rheumatism*, 50(8), pp.2516-2520.
- Horn, J.L., 1965. A rationale and test for the number of factors in factor analysis. *Psychometrika*, 30(2), pp.179-185.

- Hoshino, Y., Wang, J.H., Lorenz, S., Fu, F.H. and Tashman, S., 2012. The effect of distal femur bony morphology on in vivo knee translational and rotational kinematics. *Knee Surgery, Sports Traumatology, Arthroscopy*, 20(7), pp.1331-1338.
- Hudelmaier, M., Glaser, C., Englmeier, K.H., Reiser, M., Putz, R. and Eckstein, F., 2003. Correlation of knee-joint cartilage morphology with muscle cross-sectional areas vs. anthropometric variables. *The Anatomical Record Part A: Discoveries in Molecular, Cellular, and Evolutionary Biology*, 270(2), pp.175-184.
- Insall, J. and Salvati, E., 1971. Patella Position in the Normal Knee Joint 1. *Radiology*, 101(1), pp.101-104.
- Ivester, J.C., Cyr, A.J., Harris, M.D., Kulis, M.J., Rullkoetter, P.J. and Shelburne, K.B., 2015. A Reconfigurable High-Speed Stereo-Radiography System for Sub-Millimeter Measurement of In Vivo Joint Kinematics. *Journal of Medical Devices*, 9(4), p.041009.
- Iwaki, H., Pinskerova, V. and Freeman, M.A.R., 2000. Tibiofemoral movement 1: the shapes and relative movements of the femur and tibia in the unloaded cadaver knee. *Journal of Bone & Joint Surgery, British Volume*, 82(8), pp.1189-1195.
- Jafari, A., Farahmand, F. and Meghdari, A., 2008. The effects of trochlear groove geometry on patellofemoral joint stability-a computer model study. *Proceedings of the Institution of Mechanical Engineers, Part H: Journal of Engineering in Medicine*, 222(1), pp.75-88.
- Johal, P., Williams, A., Wragg, P., Hunt, D. and Gedroyc, W., 2005. Tibio-femoral movement in the living knee. A study of weight bearing and non-weight bearing knee kinematics using 'interventional' MRI. *Journal of biomechanics*, 38(2), pp.269-276.
- Jolliffe, I., 2002. *Principal component analysis*. John Wiley & Sons, Ltd.
- Kalichman, L., Zhu, Y., Zhang, Y., Niu, J., Gale, D., Felson, D.T. and Hunter, D., 2007. The association between patella alignment and knee pain and function: an MRI study in persons with symptomatic knee osteoarthritis. *Osteoarthritis and Cartilage*, 15(11), pp.1235-1240.
- Kawano, T., Miura, H., Nagamine, R., Urabe, K., Matsuda, S., Mawatari, T., Moro-Oka, T. and Iwamoto, Y., 2002. Factors affecting patellar tracking after total knee arthroplasty. *The Journal of arthroplasty*, 17(7), pp.942-947.
- Kefala, V., 2015. *Assessment of Normal Knee Kinematics using High-Speed Stereo-Radiography System (Masters thesis, UNIVERSITY OF DENVER)*.
- Kiapour, A.M. and Murray, M.M., 2014. Basic science of anterior cruciate ligament injury and repair. *Bone and Joint Research*, 3(2), pp.20-31.
- Komistek, R.D., Dennis, D.A., Mabe, J.A. and Walker, S.A., 2000. An in vivo determination of patellofemoral contact positions. *Clinical Biomechanics*, 15(1), pp.29-36.

- Koo, S., Gold, G.E. and Andriacchi, T.P., 2005. Considerations in measuring cartilage thickness using MRI: factors influencing reproducibility and accuracy. *Osteoarthritis and Cartilage*, 13(9), pp.782-789.
- Kurazume, R., Nakamura, K., Okada, T., Sato, Y., Sugano, N., Koyama, T., Iwashita, Y. and Hasegawa, T., 2009. 3D reconstruction of a femoral shape using a parametric model and two 2D fluoroscopic images. *Computer Vision and Image Understanding*, 113(2), pp.202-211.
- Laporte, S., Skalli, W., De Guise, J.A., Lavaste, F. and Mitton, D., 2003. A biplanar reconstruction method based on 2D and 3D contours: application to the distal femur. *Computer Methods in Biomechanics & Biomedical Engineering*, 6(1), pp.1-6.
- Laprade, J. and Lee, R., 2005. Real-time measurement of patellofemoral kinematics in asymptomatic subjects. *The Knee*, 12(1), pp.63-72.
- Laz, P.J. and Browne, M., 2010. A review of probabilistic analysis in orthopaedic biomechanics. *Proceedings of the Institution of Mechanical Engineers, Part H: Journal of Engineering in Medicine*, 224(8), pp.927-943.
- Ledesma, R.D. and Valero-Mora, P., 2007. Determining the number of factors to retain in EFA: An easy-to-use computer program for carrying out parallel analysis. *Practical assessment, research & evaluation*, 12(2), pp.1-11.
- Leszko, F., Hovinga, K.R., Lerner, A.L., Komistek, R.D. and Mahfouz, M.R., 2011. In vivo normal knee kinematics: is ethnicity or gender an influencing factor?. *Clinical Orthopaedics and Related Research*, 469(1), pp.95-106.
- Leszko, F., Sharma, A., Komistek, R.D., Mahfouz, M.R., Cates, H.E. and Scuderi, G.R., 2010. Comparison of in vivo patellofemoral kinematics for subjects having high-flexion total knee arthroplasty implant with patients having normal knees. *The Journal of arthroplasty*, 25(3), pp.398-404.
- Li, G., Lopez, O. and Rubash, H., 2001. Variability of a three-dimensional finite element model constructed using magnetic resonance images of a knee for joint contact stress analysis. *Journal of biomechanical engineering*, 123(4), pp.341-346.
- Li, G., Park, S.E., DeFrate, L.E., Schutzer, M.E., Ji, L., Gill, T.J. and Rubash, H.E., 2005. The cartilage thickness distribution in the tibiofemoral joint and its correlation with cartilage-to-cartilage contact. *Clinical biomechanics*, 20(7), pp.736-744.
- Li, G., Van de Velde, S.K. and Bingham, J.T., 2008. Validation of a non-invasive fluoroscopic imaging technique for the measurement of dynamic knee joint motion. *Journal of biomechanics*, 41(7), pp.1616-1622.

- Li, G., Wuerz, T.H. and DeFrate, L.E., 2004. Feasibility of using orthogonal fluoroscopic images to measure in vivo joint kinematics. *Journal of biomechanical engineering*, 126(2), pp.313-318.
- Lorenz, C. and Krahnstöver, N., 2000. Generation of point-based 3D statistical shape models for anatomical objects. *Computer vision and image understanding*, 77(2), pp.175-191.
- Mahfouz, M., Fatah, E.E.A., Bowers, L.S. and Scuderi, G., 2012. Three-dimensional morphology of the knee reveals ethnic differences. *Clinical Orthopaedics and Related Research*, 470(1), pp.172-185.
- Mahfouz, M.R., Hoff, W.A., Komistek, R.D. and Dennis, D.A., 2003. A robust method for registration of three-dimensional knee implant models to two-dimensional fluoroscopy images. *Medical Imaging, IEEE Transactions on*, 22(12), pp.1561-1574.
- Maletsky, L.P. and Hillberry, B.M., 2005. Simulating dynamic activities using a five-axis knee simulator. *Journal of biomechanical engineering*, 127(1), pp.123-133.
- Markelj, P., Tomaževič, D., Likar, B. and Pernuš, F., 2012. A review of 3D/2D registration methods for image-guided interventions. *Medical image analysis*, 16(3), pp.642-661.
- Martelli, S. and Pinskerova, V., 2002. The shapes of the tibial and femoral articular surfaces in relation to tibiofemoral movement. *Journal Of Bone And Joint Surgery-British Volume*, 84(4), pp.607-613.
- Masouros, S.D., Bull, A.M.J. and Amis, A.A., 2010. (i) Biomechanics of the knee joint. *Orthopaedics and Trauma*, 24(2), pp.84-91.
- McGibbon, C.A., 2003. Inter-rater and intra-rater reliability of subchondral bone and cartilage thickness measurement from MRI☆. *Magnetic resonance imaging*, 21(7), pp.707-714.
- Mei, L., Figl, M., Rueckert, D., Darzi, A. and Edwards, P., 2008, June. Statistical shape modelling: how many modes should be retained?. In *Computer Vision and Pattern Recognition Workshops, 2008. CVPRW'08. IEEE Computer Society Conference on* (pp. 1-8). IEEE.
- Meller, S. and Kalender, W.A., 2004, June. Building a statistical shape model of the pelvis. In *International Congress Series (Vol. 1268, pp. 561-566)*. Elsevier.
- Mizuno, Y., Kumagai, M., Mattessich, S.M., Elias, J.J., Ramrattan, N., Cosgarea, A.J. and Chao, E., 2001. Q-angle influences tibiofemoral and patellofemoral kinematics. *Journal of Orthopaedic Research*, 19(5), pp.834-840.

- Morton, N.A., Maletsky, L.P., Pal, S. and Laz, P.J., 2007. Effect of variability in anatomical landmark location on knee kinematic description. *Journal of Orthopaedic Research*, 25(9), pp.1221-1230.
- Neogi, T., Bowes, M.A., Niu, J., Souza, K.M., Vincent, G.R., Goggins, J., Zhang, Y. and Felson, D.T., 2013. Magnetic resonance imaging-based three-dimensional bone shape of the knee predicts onset of knee osteoarthritis: data from the Osteoarthritis Initiative. *Arthritis & Rheumatism*, 65(8), pp.2048-2058.
- Nha, K.W., Papannagari, R., Gill, T.J., Van de Velde, S.K., Freiberg, A.A., Rubash, H.E. and Li, G., 2008. In vivo patellar tracking: clinical motions and patellofemoral indices. *Journal of Orthopaedic Research*, 26(8), pp.1067-1074.
- Omoumi, P., Michoux, N., Roemer, F.W., Thienpont, E. and Berg, B.V., 2015. Cartilage thickness at the posterior medial femoral condyle is increased in femorotibial knee osteoarthritis: a cross-sectional CT arthrography study (Part 2). *Osteoarthritis and Cartilage*, 23(2), pp.224-231.
- Pal, S., Besier, T.F., Beaupre, G.S., Fredericson, M., Delp, S.L. and Gold, G.E., 2013. Patellar maltracking is prevalent among patellofemoral pain subjects with patella alta: an upright, weightbearing MRI study. *Journal of Orthopaedic Research*, 31(3), pp.448-457.
- Pal, S., Draper, C.E., Fredericson, M., Gold, G.E., Delp, S.L., Beaupre, G.S. and Besier, T.F., 2011. Patellar maltracking correlates with vastus medialis activation delay in patellofemoral pain patients. *The American journal of sports medicine*, 39(3), pp.590-598.
- Pandy, M.G., Sasaki, K. and Kim, S., 1997. A three-dimensional musculoskeletal model of the human knee joint. Part 1: theoretical construction. *Computer Methods In Biomechanics And Bio Medical Engineering*, 1(2), pp.87-108.
- Papaioannou, G., Nianios, G., Mitrogiannis, C., Fyhrie, D., Tashman, S. and Yang, K.H., 2008. Patient-specific knee joint finite element model validation with high-accuracy kinematics from biplane dynamic Roentgen stereogrammetric analysis. *Journal of Biomechanics*, 41(12), pp.2633-2638.
- Petersilge, W.J., Oishi, C.S., Kaufman, K.R., Irby, S.E. and Colwell Jr, C.W., 1994. The effect of trochlear design on patellofemoral shear and compressive forces in total knee arthroplasty. *Clinical orthopaedics and related research*, 309, pp.124-130.
- Piazza, S.J. and Cavanagh, P.R., 2000. Measurement of the screw-home motion of the knee is sensitive to errors in axis alignment. *Journal of biomechanics*, 33(8), pp.1029-1034.
- Powers, C.M., 2000. Patellar kinematics, part II: the influence of the depth of the trochlear groove in subjects with and without patellofemoral pain. *Physical therapy*, 80(10), pp.965-973.

- Powers, C.M., Shellock, F.G. and Pfaff, M., 1998. Quantification of patellar tracking using kinematic MRI. *Journal of Magnetic Resonance Imaging*, 8(3), pp.724-732.
- Powers, C.M., Ward, S.R., Fredericson, M., Guillet, M. and Shellock, F.G., 2003. Patellofemoral kinematics during weight-bearing and non-weight-bearing knee extension in persons with lateral subluxation of the patella: a preliminary study. *Journal of Orthopaedic & Sports Physical Therapy*, 33(11), pp.677-685.
- Querol, L.B., Büchler, P., Rueckert, D., Nolte, L.P. and Ballester, M.Á.G., 2006. Statistical finite element model for bone shape and biomechanical properties. In *Medical Image Computing and Computer-Assisted Intervention—MICCAI 2006* (pp. 405-411). Springer Berlin Heidelberg.
- Rao, C., Fitzpatrick, C.K., Rullkoetter, P.J., Maletsky, L.P., Kim, R.H. and Laz, P.J., 2013. A statistical finite element model of the knee accounting for shape and alignment variability. *Medical engineering & physics*, 35(10), pp.1450-1456.
- Ravi, B., Croxford, R., Reichmann, W.M., Losina, E., Katz, J.N. and Hawker, G.A., 2012. The changing demographics of total joint arthroplasty recipients in the United States and Ontario from 2001 to 2007. *Best practice & research Clinical rheumatology*, 26(5), pp.637-647.
- Rhee, S.J. and Haddad, F.S., 2008. Patello-femoral joint in total knee replacement. *Current Orthopaedics*, 22(2), pp.132-138.
- Rueckert, D., Frangi, A.F. and Schnabel, J.A., 2003. Automatic construction of 3-D statistical deformation models of the brain using nonrigid registration. *Medical Imaging, IEEE Transactions on*, 22(8), pp.1014-1025.
- Sarkalkan, N., Weinans, H. and Zadpoor, A.A., 2014. Statistical shape and appearance models of bones. *Bone*, 60, pp.129-140.
- Schumann, S., Tannast, M., Nolte, L.P. and Zheng, G., 2010. Validation of statistical shape model based reconstruction of the proximal femur—a morphology study. *Medical engineering & physics*, 32(6), pp.638-644.
- Shalhoub, S. and Maletsky, L.P., 2014. Variation in patellofemoral kinematics due to changes in quadriceps loading configuration during in vitro testing. *Journal of biomechanics*, 47(1), pp.130-136.
- Sharma, G.B., Saevarsson, S.K., Amiri, S., Montgomery, S., Ramm, H., Lichti, D.D., Lieck, R., Zachow, S. and Anglin, C., 2012. Radiological method for measuring patellofemoral tracking and tibiofemoral kinematics before and after total knee replacement. *Bone and Joint Research*, 1(10), pp.263-271.

- Sheehan, F.T., Derasari, A., Brindle, T.J. and Alter, K.E., 2009. Understanding patellofemoral pain with maltracking in the presence of joint laxity: complete 3D in vivo patellofemoral and tibiofemoral kinematics. *Journal of Orthopaedic Research*, 27(5), pp.561-570.
- Shim, V.B., Pitto, R.P., Streicher, R.M., Hunter, P.J. and Anderson, I.A., 2008. Development and validation of patient-specific finite element models of the hemipelvis generated from a sparse CT data set. *Journal of biomechanical engineering*, 130(5), p.051010.
- Shlens, J., 2014. A tutorial on principal component analysis. arXiv preprint arXiv:1404.1100.
- Singerman, R., Pagan, H.D., Peyser, A.B. and Goldberg, V.M., 1997. Effect of femoral component rotation and patellar design on patellar forces. *Clinical orthopaedics and related research*, 334, pp.345-353.
- Smoger, L.M., Fitzpatrick, C.K., Clary, C.W., Cyr, A.J., Maletsky, L.P., Rullkoetter, P.J. and Laz, P.J., 2015. Statistical modeling to characterize relationships between knee anatomy and kinematics. *Journal of Orthopaedic Research*, 33(11), pp.1620-1630.
- Solloway, S., Hutchinson, C.E., Waterton, J.C. and Taylor, C.J., 1997. The use of active shape models for making thickness measurements of articular cartilage from MR images. *Magnetic Resonance in Medicine*, 37(6), pp.943-952.
- Song, Y., Greve, J.M., Carter, D.R., Koo, S. and Giori, N.J., 2006. Articular cartilage MR imaging and thickness mapping of a loaded knee joint before and after meniscectomy. *Osteoarthritis and cartilage*, 14(8), pp.728-737.
- Stäubli, H.U., Schatzmann, L., Brunner, P., Rincón, L. and Nolte, L.P., 1999. Mechanical tensile properties of the quadriceps tendon and patellar ligament in young adults. *The American journal of sports medicine*, 27(1), pp.27-34.
- Stefanik, J.J., Zumwalt, A.C., Segal, N.A., Lynch, J.A. and Powers, C.M., 2013. Association between measures of patella height, morphologic features of the trochlea, and patellofemoral joint alignment: the MOST study. *Clinical Orthopaedics and Related Research*, 471(8), pp.2641-2648.
- Stiehl, J.B., Komistek, R.D., Dennis, D.A. and Keblish, P.A., 2001. Kinematics of the patellofemoral joint in total knee arthroplasty. *The Journal of arthroplasty*, 16(6), pp.706-714.
- Turk, M. and Pentland, A., 1991. Eigenfaces for recognition. *Journal of cognitive neuroscience*, 3(1), pp.71-86.

- Varadarajan, K.M., Freiberg, A.A., Gill, T.J., Rubash, H.E. and Li, G., 2010. Relationship between three-dimensional geometry of the trochlear groove and in vivo patellar tracking during weight-bearing knee flexion. *Journal of biomechanical engineering*, 132(6), p.061008.
- von Eisenhart-Rothe, R., Siebert, M., Bringmann, C., Vogl, T., Englmeier, K.H. and Graichen, H., 2004. A new in vivo technique for determination of 3D kinematics and contact areas of the patello-femoral and tibio-femoral joint. *Journal of biomechanics*, 37(6), pp.927-934.
- von Eisenhart-Rothe, R., Vogl, T., Englmeier, K.H. and Graichen, H., 2007. A new in vivo technique for determination of femoro-tibial and femoro-patellar 3D kinematics in total knee arthroplasty. *Journal of biomechanics*, 40(14), pp.3079-3088.
- Waterton, J.C., Solloway, S., Foster, J.E., Keen, M.C., Gandy, S., Middleton, B.J., Maciewicz, R.A., Watt, I., Dieppe, P.A. and Taylor, C.J., 2000. Diurnal variation in the femoral articular cartilage of the knee in young adult humans. *Magnetic resonance in medicine*, 43(1), pp.126-132.
- White, D., Chelule, K.L. and Seedhom, B.B., 2008. Accuracy of MRI vs CT imaging with particular reference to patient specific templates for total knee replacement surgery. *The International Journal of Medical Robotics and Computer Assisted Surgery*, 4(3), pp.224-231.
- Yamaguchi, S., Tanaka, Y., Kosugi, S., Takakura, Y., Sasho, T. and Banks, S.A., 2011. In vivo kinematics of two-component total ankle arthroplasty during non-weightbearing and weightbearing dorsiflexion/plantarflexion. *Journal of biomechanics*, 44(6), pp.995-1000.
- Yang, Y.M., Rueckert, D. and Bull, A.M., 2008. Predicting the shapes of bones at a joint: application to the shoulder. *Computer Methods in Biomechanics and Biomedical Engineering*, 11(1), pp.19-30.
- Yang, Z., Fripp, J., Chandra, S.S., Neubert, A., Xia, Y., Strudwick, M., Paproki, A., Engstrom, C. and Crozier, S., 2015. Automatic bone segmentation and bone-cartilage interface extraction for the shoulder joint from magnetic resonance images. *Physics in medicine and biology*, 60(4), p.1441.
- You, B.M., Siy, P., Anderst, W. and Tashman, S., 2001. In vivo measurement of 3-D skeletal kinematics from sequences of biplane radiographs: application to knee kinematics. *Medical Imaging, IEEE Transactions on*, 20(6), pp.514-525.
- Yue, B., Varadarajan, K.M., Ai, S., Tang, T., Rubash, H.E. and Li, G., 2011. Differences of knee anthropometry between Chinese and white men and women. *The Journal of arthroplasty*, 26(1), pp.124-130.

- Zheng, G. and Nolte, L.P., 2006. Surface reconstruction of bone from X-ray images and point distribution model incorporating a novel method for 2D-3D correspondence. In *Computer Vision and Pattern Recognition, 2006 IEEE Computer Society Conference on* (Vol. 2, pp. 2237-2244). IEEE.
- Zheng, G., Gollmer, S., Schumann, S., Dong, X., Feilkas, T. and Ballester, M.A.G., 2009. A 2D/3D correspondence building method for reconstruction of a patient-specific 3D bone surface model using point distribution models and calibrated X-ray images. *Medical Image Analysis*, 13(6), pp.883-899.
- Zhu, Z. and Li, G., 2011. Construction of 3D human distal femoral surface models using a 3D statistical deformable model. *Journal of biomechanics*, 44(13), pp.2362-2368.
- Zhu, Z. and Li, G., 2012. An automatic 2D–3D image matching method for reproducing spatial knee joint positions using single or dual fluoroscopic images. *Computer methods in biomechanics and biomedical engineering*, 15(11), pp.1245-1256.

APPENDIX A. RELATED PUBLICATIONS

- Smoger, L.M., Fitzpatrick, C.K., Clary, C.W., Cyr, A.J., Maletsky, L.P., Rullkoetter, P.J. and Laz, P.J., 2015. Statistical modeling to characterize relationships between knee anatomy and kinematics. *Journal of Orthopaedic Research*, 33(11), pp.1620-1630.
- Smoger, L.M., Cyr, A.J., Vierczhalek, A., Fitzpatrick, C.K., Clary, C.W., Maletsky, L.P., Rullkoetter, P.J., Laz, P.J. Statistical modeling to characterize relationships between knee anatomy and kinematics. 60th Annual Meeting of the Orthopaedic Research Society, March 2014.
- Laz, P.J., Smoger, L.M., Fitzpatrick, C.K., Maletsky, L.P., Shelburne, K.B., Rullkoetter, P.J. Characterizing intersubject variability for population-based evaluations of joint mechanics. Multiscale Modeling Consortium Meeting, October 2013.

APPENDIX B. STATISTICAL MODELING TO CHARACTERIZE RELATIONSHIPS
BETWEEN KNEE ANATOMY AND KINEMATICS

Appendix B.1. List of Anatomical Measures

- Epicondylar Width (mm) – Distance between the medial and lateral epicondyles of the femur.
- Femur AP Width (mm) – Distance between the most anterior and posterior points of the femur.
- Tibia ML Width (mm) – Distance between the most medial and lateral points on the tibia in the plane of the tibial plateau.
- Patella AP Width (mm) – Distance between the most anterior and posterior points of the patella.
- Patella Angle (deg.) – Angle, in the transverse plane, between two lines drawn along the surfaces of the medial and lateral facets of the patella.
- Insall-Salvati Index – Ratio of the length of the patellar tendon to the height of the patella.
- Trochlear Angle (deg.) - Angle, in the transverse plane, between the posterior condylar line and a line passing along the most anterior margins of the medial and lateral trochlear facets.
- Anterior Sulcus Angle (deg.) – Angle, in the transverse plane, between two lines drawn along the surfaces of the medial and lateral trochlear facets.
- Medial Trochlear Inclination (deg.) – Angle, in the transverse plane, between the posterior condylar line and a line drawn along the surface of the medial trochlear facet.
- Lateral Trochlear Inclination (deg.) – Angle, in the transverse plane, between the posterior condylar line and a line drawn along the surface of the lateral trochlear facet.
- Antero-inferior Sulcus Angle (deg.) – Angle, in the 45° merchant view, between two lines drawn along the surfaces of the medial and lateral trochlear facets.

Distal Sulcus Angle (deg.) – Angle, in the coronal plane, between two lines drawn along the surfaces of the medial and lateral trochlear facets.

Distal Condylar Angle (deg.) – Angle, in the coronal plane, between a line connecting the most distal points of the condyles and the mediolateral axis of the femur.

Bisect Offset (%) – The percentage of the patellar lateral to the midline of the femur.

Appendix B.2. Description of Further Modes

Descriptions of the first three modes were provided in Chapter 4. This section describes the relevant shape-kinematic relationships for modes 4 through 6. As the amount of variability decreases with later modes (Table B.1), these modes characterized more subtle changes.

In comparison to Mode 4-, Mode 4+ exhibited a more medial patellar ridge and thicker medial facet, which, when paired with a more prominent lateral trochlear facet on the femur, contributed to a more lateral initial patellar alignment (Figure B.4). PC score for Mode 4 was moderately correlated to initial ML patellar alignment ($r = 0.64$, Table B.2), which is consistent with findings from Harbaugh et al. relating patellar ML translation and the prominence of the lateral trochlear facet (Harbaugh et al., 2010). Mode 4+ also featured a near constant distal and posterior femoral radius, leading to less tibial SI translation through the cycle; however, deeper tibial dwell points placed Mode 4+ in a more superior initial position (not shown). Tibial SI translation through the cycle was only 2 mm compared to the 7 mm of translation in 4-. Mode 4- described a non-uniform AP/SI aspect ratio with a decreasing radius from distal to posterior on the medial femoral condyle that contributed to a more superior motion through the cycle ($r = -0.55$).

Mode 5 primarily described changes to the femoral intercondylar notch and

medial-lateral kinematics (TF and PF, Figure B.5). PC score for Mode 5 was highly correlated to tibial ML translation through the cycle ($r = 0.77$, Table B.2). Mode 5+ was characterized by a larger intercondylar notch width (27 mm) compared to Mode 5- (21 mm, Figure B.5), resulting in greater medial tibial translation. Mode 5- also showed the largest amount of lateral patellar translation, which is likely attributed to the tibial motion and a steeper medial trochlear facet in the distal region.

Both Modes 5 and 6 captured differences in the femur's distal sulcus geometry and variation in tibial IE rotation through the cycle (Figure B.5 and Figure B.6). Mode 5 described the angle of the medial femoral facet and intercondylar notch. Noting the correlation between TF IE and PF ML (0.61, below), Mode 5 exhibited the largest variation in ROM for these measures, suggesting the geometric changes led to interactions between patellar medial translation and internal tibial rotation. For Mode 6+ and 6-, respectively, the distal sulcus angle was 130° and 120° , and tibial IE ROM was 14.1° degrees and 6.2° of internal rotation through the cycle. Accordingly, the PC score for Mode 6 was correlated to TF IE ROM (0.51, Table B.2).

Expanding on distal sulcus angle and TF IE rotation, Mode 6 also characterized variation in the J-curve, which was more subtle than in Mode 1, and tibial AP translation. PC score for Mode 6 was correlated to the TF AP ROM ($r = -0.55$, Table B.2). Mode 6- described changes in the shape of the posterior-inferior aspect of the femoral condylar geometry, effectively changing the shape of the J-curve (Figure B.6). The resulting flatter distal aspect of the femur was associated with a more anteriorly aligned tibia than in Mode 6+.

Table B.1 Cumulative variability explained with the specified number of modes of variation.

Mode	Cumulative variability (%)
1	23.0
2	36.3
3	49.0
4	57.7
5	64.3
6	69.4
10	84.7
15	95.3
19	100.0

Table B.2 Pearson's correlation coefficients between net kinematics defined here as the difference between start and end positions in the flexion cycle. Correlations are presented as absolute values. White cells indicate no correlation.

TF FE	TF VV	TF IE	TF ML	TF AP	TF SI	PF FE	PF VV	PF IE	PF ML	PF AP	PF SI	
						0.79				0.54		TF FE
			0.46				0.67					TF VV
								0.50	0.61	0.47		TF IE
							0.49		0.56			TF ML
												TF AP
						0.49				0.43		TF SI
										0.72	0.42	PF FE
												PF VV
									0.53			PF IE
												PF ML
												PF AP
												PF SI

	0.4 to 0.6
	0.6 to 0.8
	0.8 to 1.0

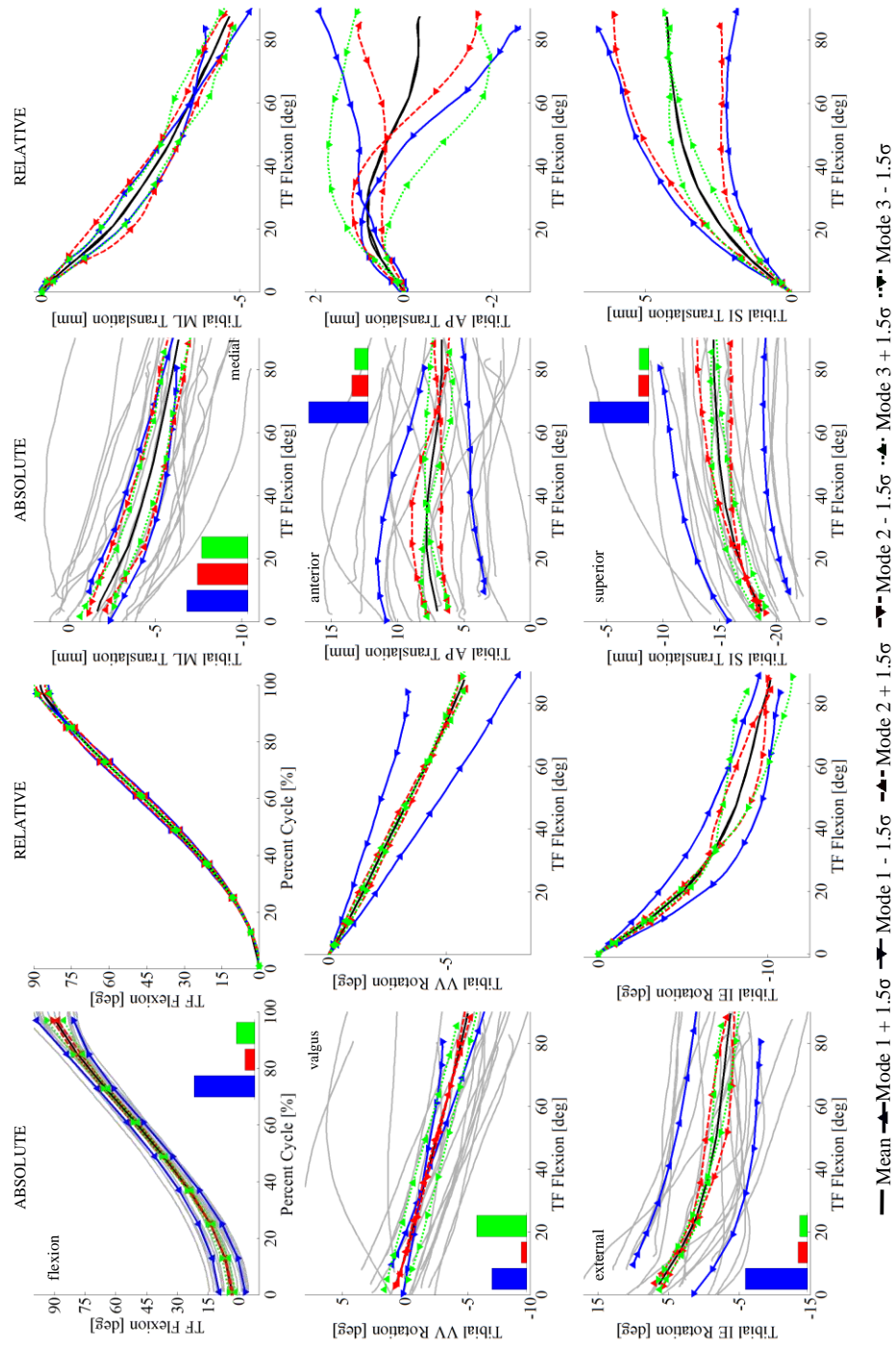


Figure B.1 Absolute and relative tibiofemoral kinematics for the first 3 principal component modes and all specimens (gray lines). Bar charts show relative contribution of each mode.

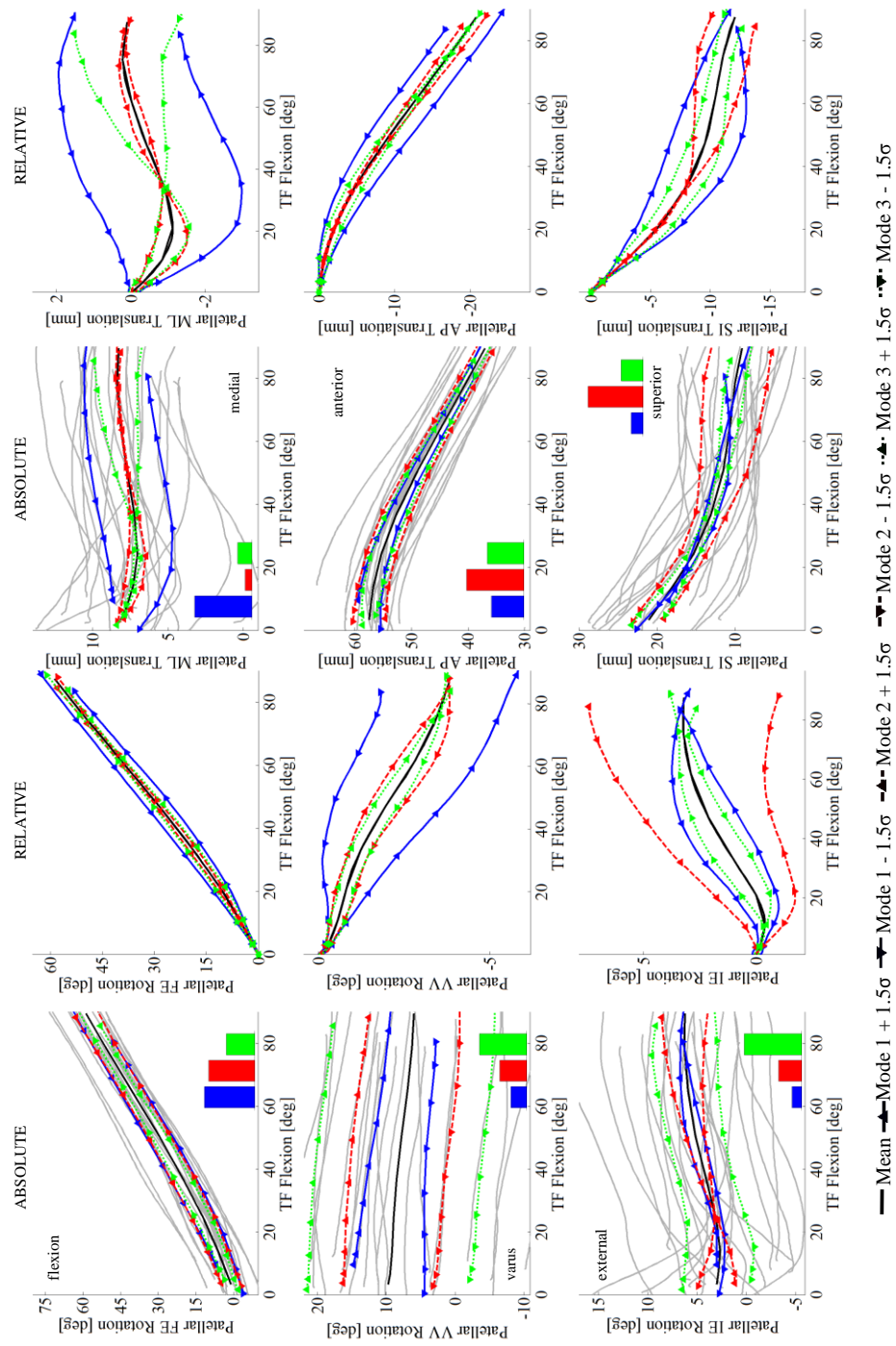


Figure B.2 Absolute and relative patellofemoral kinematics for the first 3 principal component modes and all specimens (gray lines). Bar charts show relative contribution of each mode.

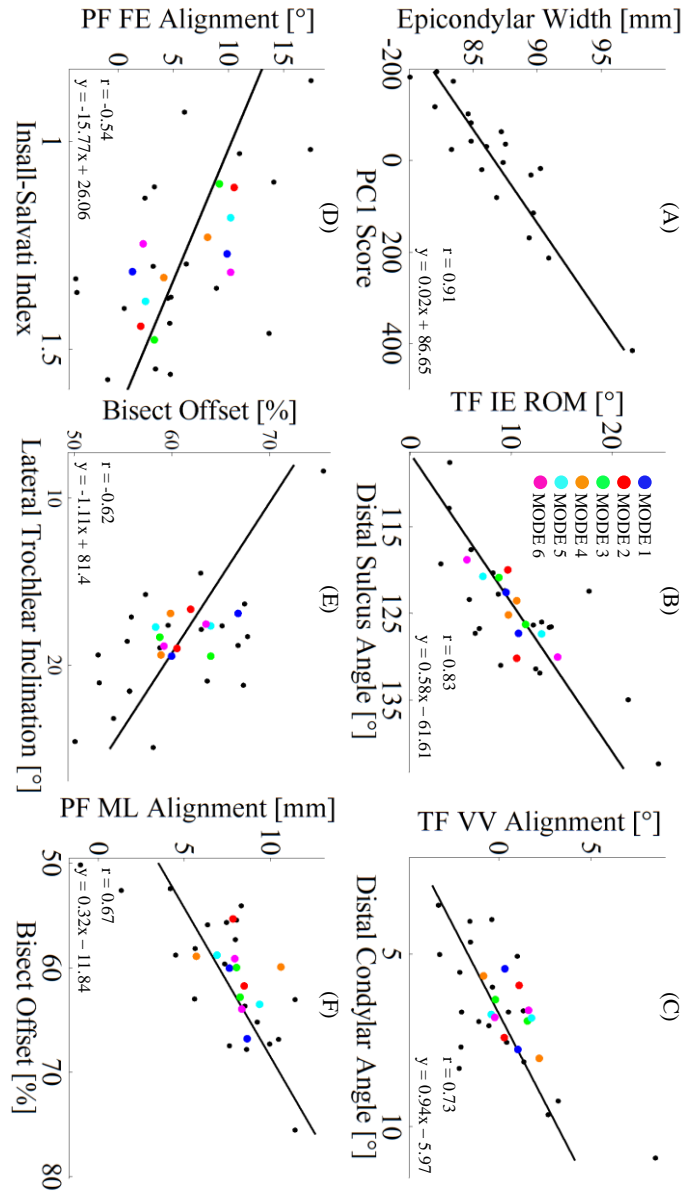


Figure B.3 Scatter plots of mode, shape and kinematic relationships with strong correlations. PC score for Mode 1 versus epicondylar width (A), anatomic measures versus tibiofemoral (TF) kinematics (B-C), and patellofemoral (PF) shape and kinematics (D-F). Colored data points represent the first six PC modes at $\pm 1.5\sigma$. Pearson's correlation coefficient (r) and linear equation are reported for each plot.

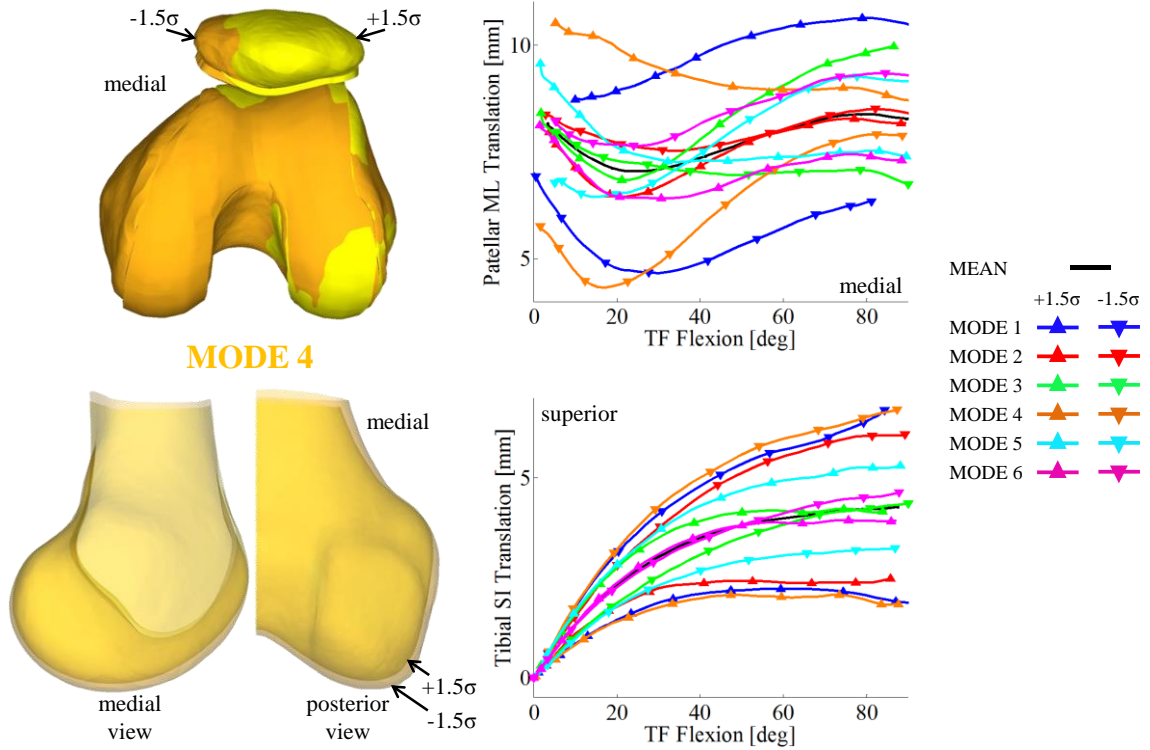


Figure B.4 Distal view of Mode 4+ and 4- showing variation in patellar ML alignment and lateral trochlear inclination (top left). The absolute patellar ML translation curve further illustrates the high ROM in Mode 4- (top right). Geometric differences in the medial femoral condyle contribute to the variation in relative tibial SI translation (bottom left and right).

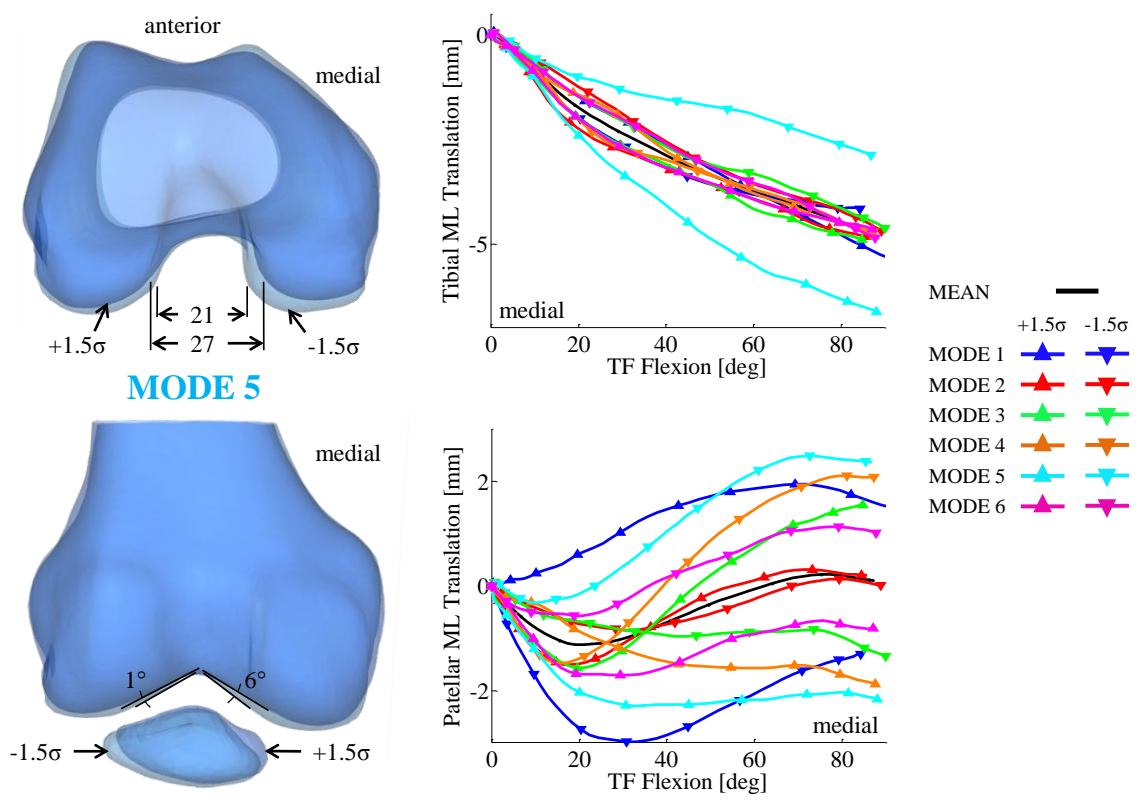


Figure B.5 Proximal view of Mode 5+ and 5- showing variation in intercondylar notch width (top left). Relative tibial ML translation through the cycle (top right). Variation in the distal region of the medial femoral facet influences the relative patellar ML translation through the cycle (bottom left and right). Dimensions are shown in millimeters unless otherwise noted.

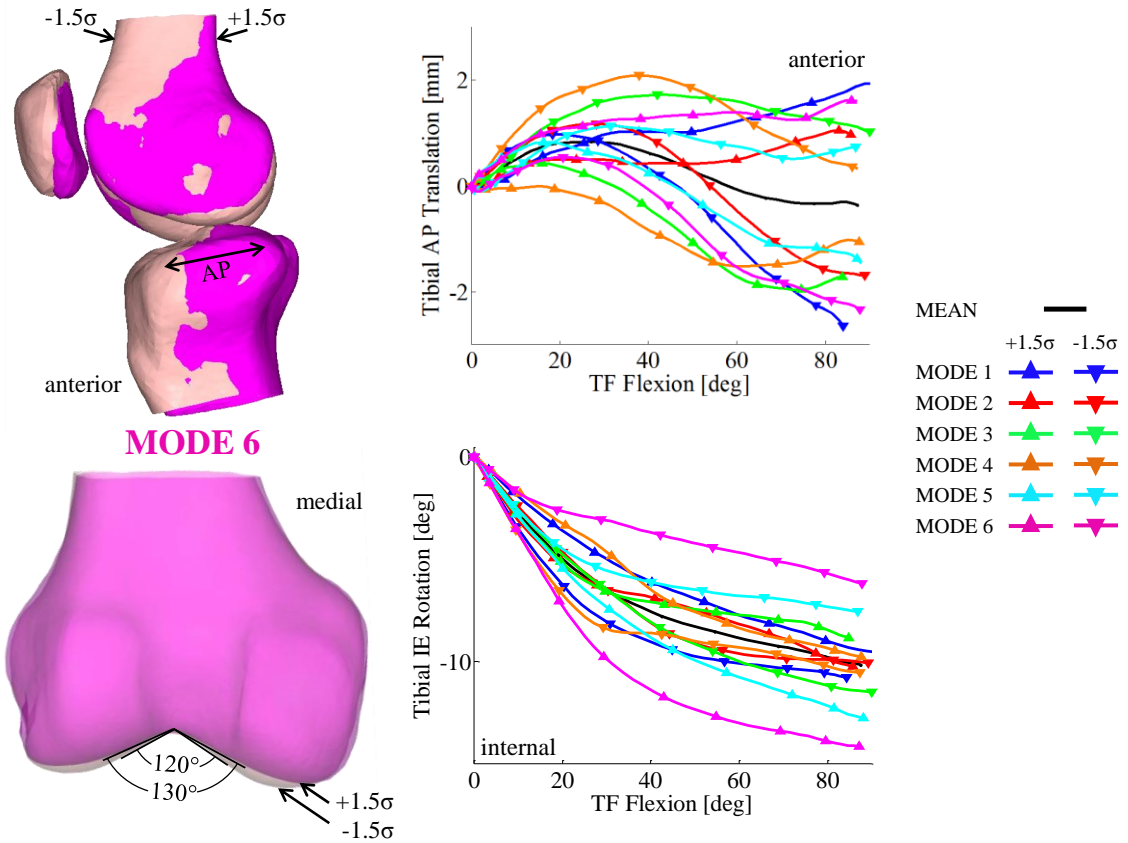


Figure B.6 Initial anterior tibial alignment in Mode 6- is associated with more prominent postero-inferior femoral condyles (top left). Second to Mode 1, Mode 6 exhibited a large amount of through-cycle variation in tibial AP translation (top right). Variation in distal sulcus angle (bottom left) and relative tibial IE rotation (bottom right) are highly correlated ($r = 0.83$).

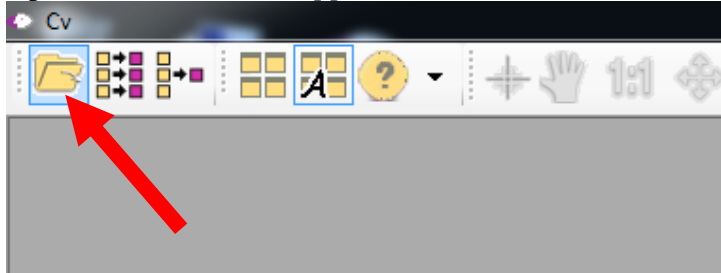
APPENDIX C. PATELLA DIGITIZATION INSTRUCTIONS IN XMALAB

Organize file/folders in the new subject's directory

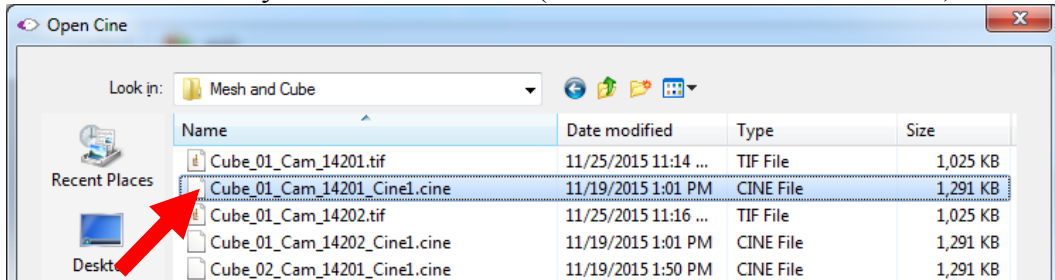
1. Create or located a 'Calibration' and 'XMA Lab' folder.
2. Copy/paste the **framespec5.csv** and **CalibrationPoints1.ref** files to the Calibration folder (take from an already processed subject folder).

Convert files from .cine to .tif

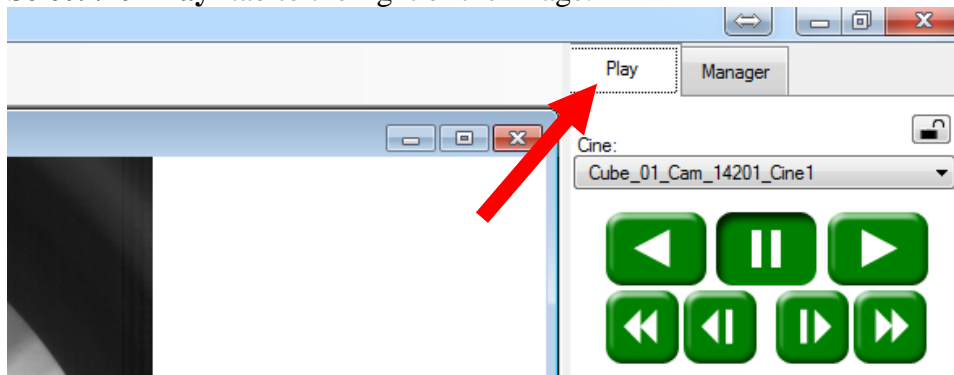
1. Open the *Cine Viewer Application, CV.exe*, and select the **Open File** icon.



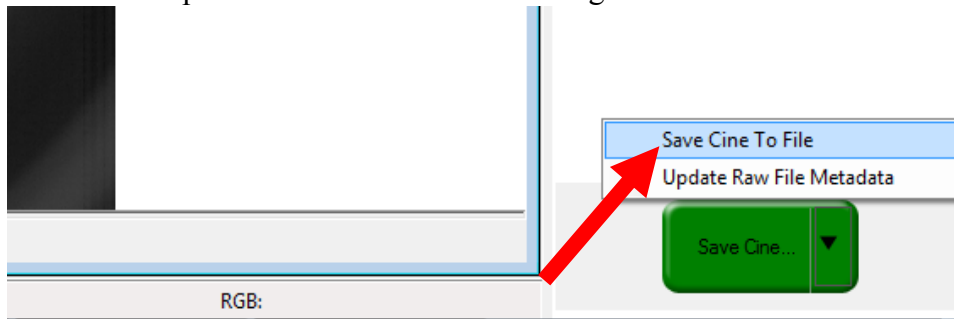
2. Select the **.cine file** you'd like to convert (i.e. *Cube_01_Cam_14201.cine*).



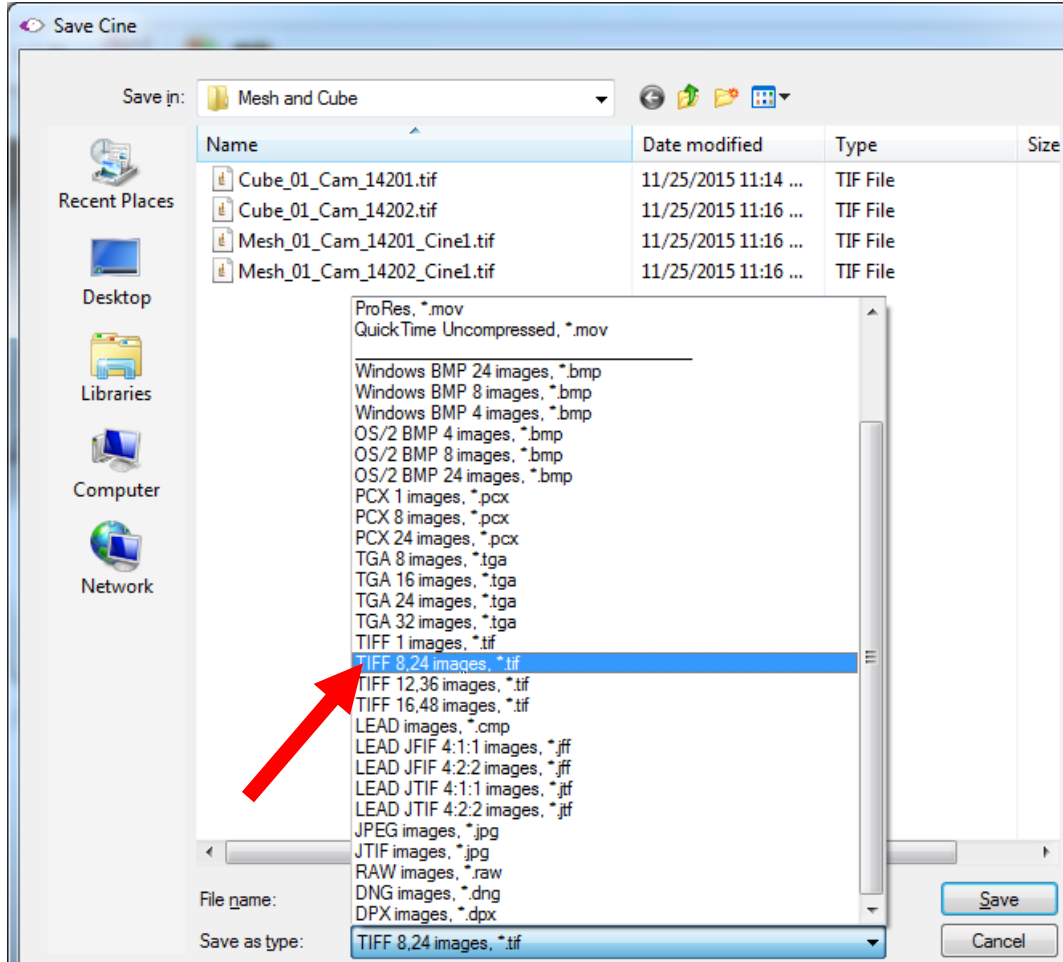
3. Select the **'Play'** tab to the right of the image.



4. Select the dropdown menu arrow at bottom right and click **'Save Cine to File'**.



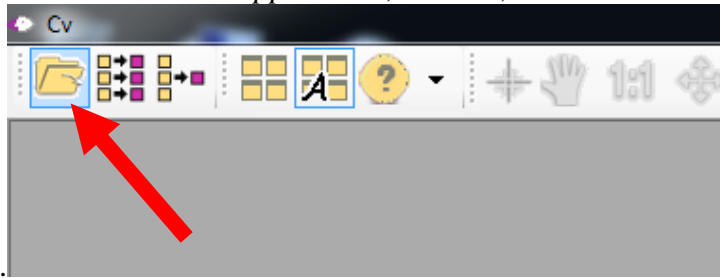
5. Choose **‘TIFF 8.24 images, *.tif’** in the **‘Save as type’** dropdown menu & **use the same filename.**



6. Return to the **‘Manager’** tab and select the red X icon to remove the file from the application.
7. **Repeat steps 2-6** for the two cube and two mesh files needed for calibration and undistortion.

Convert multiple .cine files to .tif using the 'Batch convert files' tool

1. Open the *Cine Viewer Application*, **CV.exe**, and select the **Batch convert files**

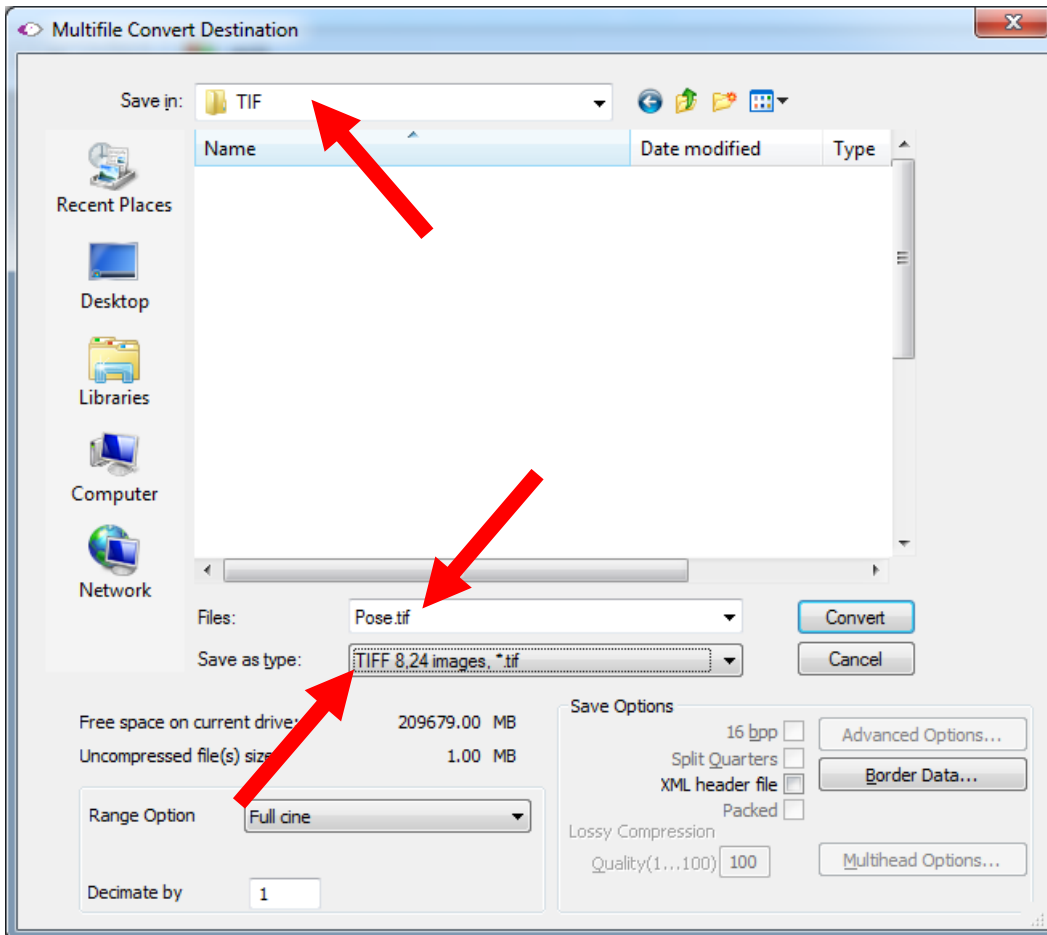


icon.

2. Create a **new folder** 'TIF' in the same directory as the .cine files and select all files to convert.



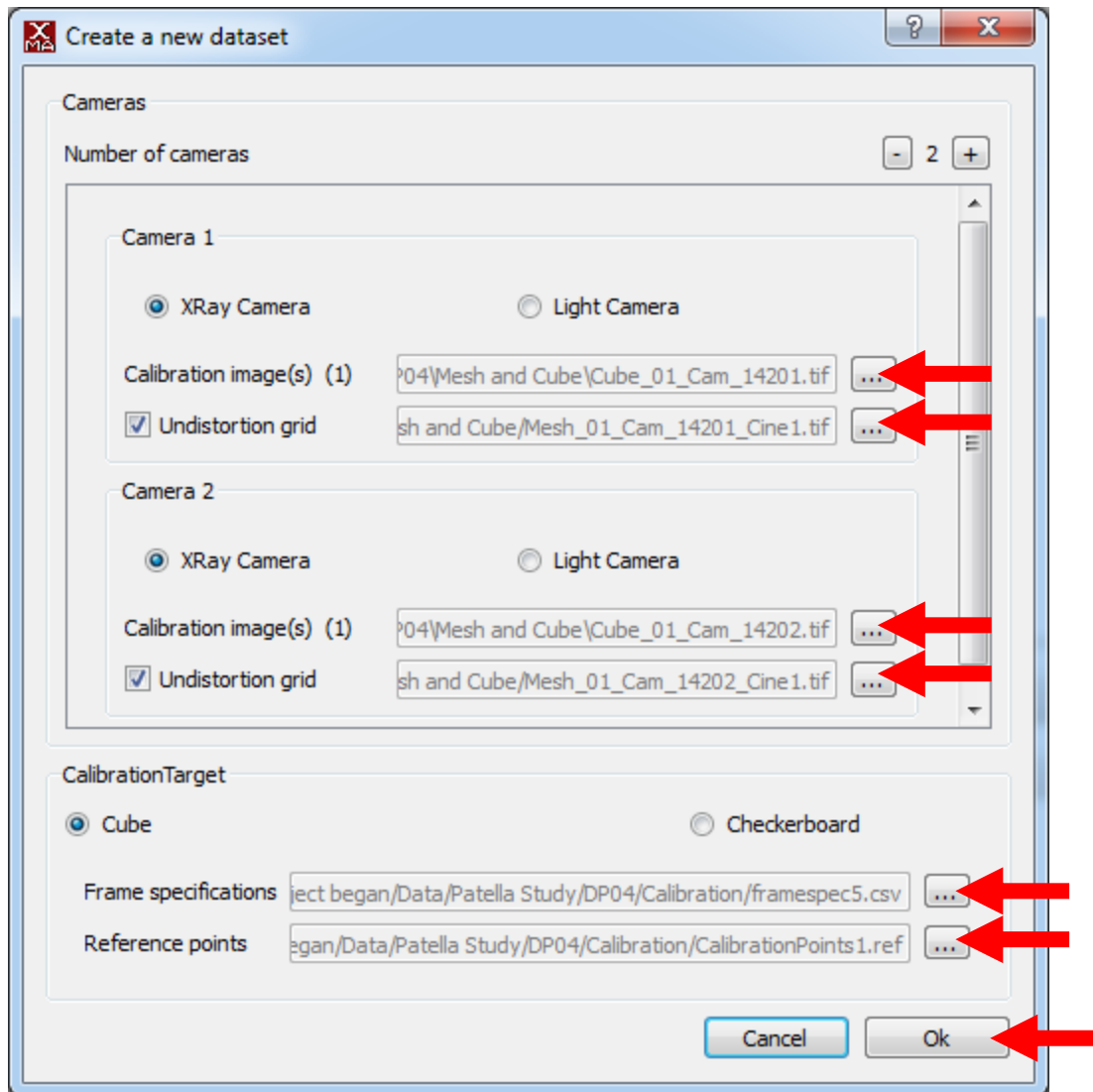
3. Upon selecting ‘**Open**’ in the window shown above, a new window will replace it. Browse to the **TIF** folder and enter a generic filename (i.e. ‘Pose’) and then choose ‘**TIFF 8.24 images, *.tif**’ in the ‘**Save as type**’ dropdown menu. Select **Convert**. A folder for each file will be created.



4. You are now done with CV.exe, you may close the application.

Create a .xma file to begin the calibration, undistortion and digitization process

1. Open the *XMALab* application and select the **New Dataset** icon.
2. Browse to and select the **cube.tif**, **mesh.tif**, **framespec.csv**, and **CalibrationPoints1.ref** files



3. The **Undistortion** workspace will load. Select the ‘**compute undistortion**’ button on the left hand side. This takes about 1 minute and results in green dots on the mesh once completed.
4. Select ‘**Calibration**’ from the Workspace dropdown menu above the images.
5. Select the first **reference point** in Camera 1 as indicated on the left hand side (i.e. 40 Triangle).
Zoom = scroll wheel & **Drag** = Rt. Click & Hold
6. Select remaining points as indicated on left hand side. All other points will appear automatically.
7. **Repeat** steps 5 & 6 for Camera 2.
8. **Calibration is complete** if no errors appear and green dots appear on all cube points.
9. Save the .xma file to the /XMA Lab/ folder (**File > Save**) with the subject name (i.e. DP04.xma).

10. **Export the DLT coefficients.**

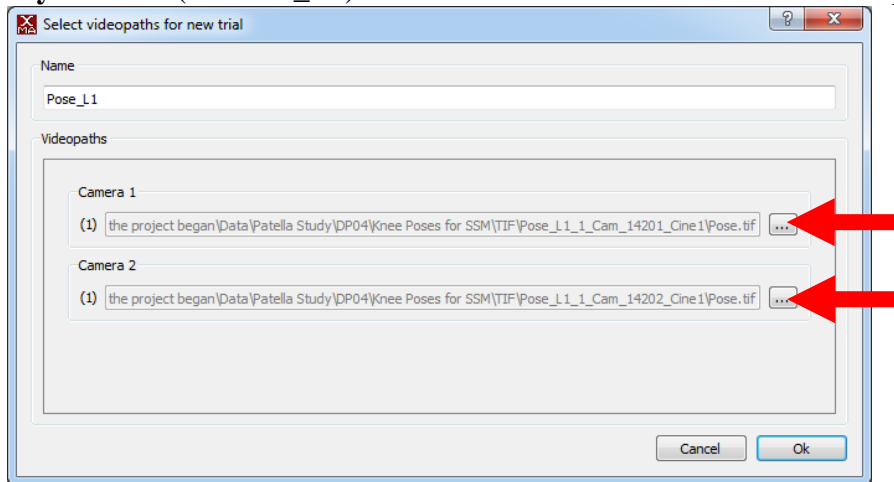
File > Export > XRayProject Matlab Format

Note a bug crashes XMA Lab 1.2.18 after files are created.

11. Do not close XMA Lab if you now wish to digitize. Move on to next set of instructions.

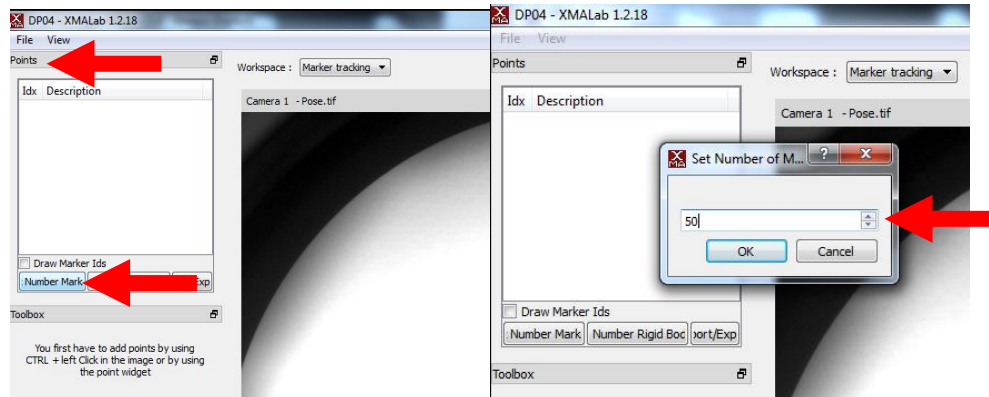
Digitizing in XMA Lab

1. If you are opening a new XMA Lab application, select '**Load .xma file**' select the .xma file.
Undistortion will reprocess.
2. Select '**Marker tracking**' from the Workspace dropdown menu above the images.
3. Select the '**Add trial**' button to open a file setup window.
4. **Name your trial** (i.e. Pose_L1). Browse to and select the .tif files for the pose. Select



Ok.

5. Select '**Set Number Markers**' in the **Points** window/tab on left side and type 50 and select **Ok**.



Note you may need additional or fewer markers depending on the patella. A list of points will appear on the left hand side.

6. **Select all points** (Ctrl+A) and **Right-click** anywhere in the **Points** list to show the **Points** menu.

7. Select ‘**Change Detectionmethod of selected Points**’ and choose ‘**no detection**’. Select **Ok**.
8. Select the **first point in the list** and then select the **first bead in Camera A**.
If no distorted epipolar line appears in Camera B, simply scroll or drag on the window to update.
9. Select the **first bead in Camera B** (should be the only bead intersecting the epipolar line).
10. To advance to the next point, **Click-hold Ctrl** while you select the **second bead in Camera A**.
11. **Release Ctrl**, select **2nd marker in Camera B** (should be only point intersecting the epipolar line).
12. **Repeat** steps 10 & 11 to digitize the 3rd and final marker.
If your crosshair moves in the image, the Detectionmethod may need to be reset. See steps 6 & 7.
Try to stay consistent with the order in which you digitize the 3 markers across all poses.
13. **Repeat** steps 10 & 11 to digitize the patellar profile in each view. **Read notes 1 & 2.**

Note 1: *If epipolar line crosses patella profile in two spots, both profile points are valid.*

You don't care how 3D points project onto both views simultaneously.


You only care how the 3D points project onto each view separately.

Note 2: *If a profile point in one camera results in an epipolar line that does **NOT** intersect the natural patellar profile in the other camera, place a dummy point **AWAY** from the profile and make a note (i.e. “Point 34 in camera A is irrelevant even though it’s useful in camera B”).*

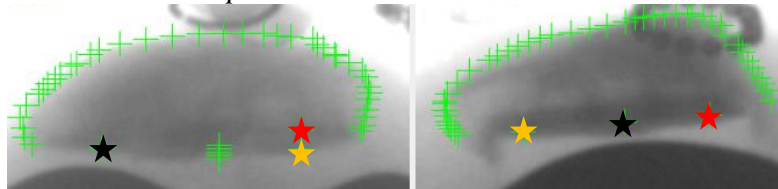
ALL “DUMMY” POINTS MUST GO AT THE END IN ONE CAMERA VIEW (i.e. points 41-46 below)



14. **Delete** any points from the **points list** that haven't been used.
15. **Export** the **3D points** to a .csv file (i.e. Pose_L1.csv) **with headers**. *File > Export > 3D Points*

16. **Save** the .xma file frequently!
17. Select the  button above the images to add a new trial/pose and repeat steps 4 through 17.
18. **Resection Plane Digitization Step** (only required in a *single view* for each patella):
 - a. Choose a pose (ideally Pose_*1) that provides a view that is as perpendicular to the cut plane as possible (i.e. the right image below is a sagittal view of a left patella).
 - b. In the perpendicular image (shown here on right) select 3 points (shown here as stars) along a straight line that best **represents the resection plane**.
 - c. Place corresponding markers in the left image in the same way shown below.

This will create a triangle (kind of like peg locations) that represents the resection plane



19. **Export** a new file of the **3D points** to a .csv file (i.e. Pose_**_cutplane.csv) **with headers**.
*Replace ** with the current pose (i.e. L1, R3, etc.)*

Make sure you have exported the following files before you run the prediction wrapper script, PAT_PREDICT_OPT_WRAPPER.m

- 1 - MergedDlts_Frame0.csv
- 4 - Pose_**.csv files (one for each pose)
- 1 - Pose_**_cutplane.csv digitized pose points with additional cutplane points
- 1 - **unwanted_points.dat** file containing the unwanted points information

Example (Leg, Pose, Camera, Start):

L	1	A	43
R	3	B	40

APPENDIX D. TRAINING SET IDENTIFIERS

Table D.3 Training set identifiers and demographics from the University of Kansas, DePuy-Synthes, and Osteoarthritis Initiative databases.

Mean		62.6	1.7	71.1	24.6
Std. Dev.		10.1	0.1	12.7	3.7
Min		37.0	1.5	42.6	19.0
Max		80.0	1.9	100.0	33.9
Subjects	Gender	Age (years)	Height (m)	Weight (kg)	BMI
BB02	M	80	1.83	93.0	27.8
BB03	M	55	1.68	81.64	29.1
BB04	M	59	1.78	63.5	20.1
BB06	M	59	1.78	63.5	20.1
BB07	M	80	1.83	92.98	27.8
BB08	M	61	1.83	90.72	27.1
BB09	M	80	1.83	93.0	27.8
BB11	M	55	1.68	81.6	29.1
BB12	M	59	1.78	63.5	20.1
BB14	M	68	1.83	100.0	29.9
BB16	M	72	1.66	68.2	24.9
BB17	M	63	1.85	77.1	22.4
BB24	M	74	1.75	81.7	26.7
BB25	M	60	1.75	60.8	19.8
BB26	M	52	1.73	72.6	24.3
BB27	M	79	1.73	74.4	24.9
BB29	M	77	1.73	86.2	28.9
BB30	M	52	1.73	72.6	24.3
BB32	M	64	1.75	61.2	19.9
BB34	M	71	1.78	70.3	22.2
DU02	M	44	1.83	70.3	21.0

DU03	M	72	1.83	77.1	23.1
KS03	M	62	1.74	75	24.7
SQ03	M	42	1.65	54.4	20.0
SQ07	M	61	1.88	69.9	19.8
DU05	F	37	1.68	54.4	19.3
9001695	F	52	1.65	77.7	28.6
9039972	F	70	1.65	61.4	22.4
9043005	F	72	1.58	56.9	22.7
9098882	F	78	1.63	76.3	28.9
9169499	F	67	1.59	76.1	30.1
9207016	F	62	1.64	68.1	25.4
9240045	F	60	1.63	53.0	20.0
9280181	F	53	1.81	81.2	24.8
9363662	F	53	1.71	88.3	30.2
9393127	F	59	1.63	65.7	24.7
9405034	F	57	1.53	62.4	26.7
9431345	F	52	1.57	53.8	21.8
9435250	F	55	1.50	42.6	19.0
9439881	F	56	1.61	54.9	21.2
9465321	F	52	1.67	74.3	26.6
9674667	F	67	1.54	60.1	25.3
9736028	F	60	1.64	91.0	33.9
9771440	F	63	1.58	58.2	23.3
9842543	F	74	1.59	67.7	26.9
9861824	F	60	1.70	64.3	22.4
9905276	F	66	1.64	75.5	28.0
9932750	F	71	1.59	58.7	23.2
9980800	F	69	1.63	76.5	28.8
9998089	F	66	1.66	60.1	21.9